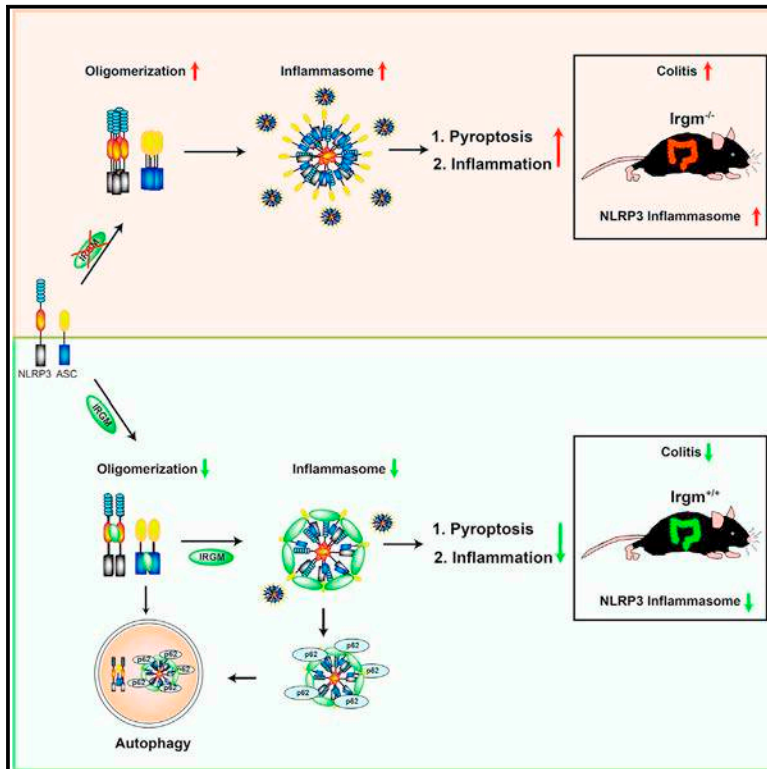# The Crohn's Disease Risk Factor IRGM Limits NLRP3 Inflammasome Activation by Impeding Its Assembly and by Mediating Its Selective Autophagy

Graphical Abstract

Authors

Subhash Mehto, Kautilya Kumar Jena, Parej Nath, ..., Ashish Jain, Gregory A. Taylor, Santosh Chauhan

Correspondence

schauhan@ils.res.in

In Brief

The IRGM is an established genetic risk factor for Crohn's diseases and several other inflammatory disorders. Mehto et al. show that IRGM inhibits NLRP3 inflammasome activation to keep the inflammation under check. This study provides a basis for the protective function of IRGM in inflammatory diseases.

Highlights

- IRGM negatively regulates NLRP3/ASC inflammasome activation

- IRGM obstructs NLRP3/ASC inflammasome assembly

- IRGM mediates selective autophagic degradation of NLRP3/ASC inflammasome

- Irgm1 by suppressing Nlrp3 inflammasome prevents gut inflammation in an IBD mouse model

CellPress

The Crohn's Disease Risk Factor IRGM Limits NLRP3 Inflammasome Activation by Impeding Its Assembly and by Mediating Its Selective Autophagy

Subhash Mehto,[1,7] Kautilya Kumar Jena,[1,2,7] Parej Nath,[1,2] Swati Chauhan,[1] Srinivasa Prasad Kolapalli,[1]
Saroj Kumar Das,[1,8] Pradyumna Kumar Sahoo,[1] Ashish Jain,[3,4] Gregory A. Taylor,[5,6] and Santosh Chauhan[1,9,*]
[1]Cell Biology and Infectious Diseases Unit, Institute of Life Sciences, Bhubaneswar 751023, India
[2]School of Biotechnology, KIIT University, Bhubaneswar 751024, India
[3]Department of Molecular Cell Biology, Institute for Cancer Research, Oslo University Hospital, Oslo, Norway
[4]Centre for Cancer Cell Reprogramming, Institute of Clinical Medicine, Faculty of Medicine, University of Oslo, Oslo, Norway
[5]Geriatric Research, Education, and Clinical Center, VA Medical Center, Durham, NC 27705, USA
[6]Departments of Medicine, Molecular Genetics and Microbiology, and Immunology, Division of Geriatrics and Center for the Study of Aging
and Human Development, Duke University Medical Center, Durham, NC 27710, USA
[7]These authors contributed equally
[8]Present address: Centre for Biotechnology, Siksha 'O' Anusandhan (Deemed to be University), Bhubaneswar, Odisha, India
[9]Lead Contact
*Correspondence: schauhan@ils.res.in
https://doi.org/10.1016/j.molcel.2018.11.018

SUMMARY

Several large-scale genome-wide association studies genetically linked IRGM to Crohn's disease and other inflammatory disorders in which the IRGM appears to have a protective function. However, the mechanism by which IRGM accomplishes this anti-inflammatory role remains unclear. Here, we reveal that IRGM/Irgm1 is a negative regulator of the NLRP3 inflammasome activation. We show that IRGM expression, which is increased by PAMPs, DAMPs, and microbes, can suppress the pro-inflammatory responses provoked by the same stimuli. IRGM/Irgm1 negatively regulates IL-1β maturation by suppressing the activation of the NLRP3 inflammasome. Mechanistically, we show that IRGM interacts with NLRP3 and ASC and hinders inflammasome assembly by blocking their oligomerization. Further, IRGM mediates selective autophagic degradation of NLRP3 and ASC. By suppressing inflammasome activation, IRGM/Irgm1 protects from pyroptosis and gut inflammation in a Crohn's disease experimental mouse model. This study for the first time identifies the mechanism by which IRGM is protective against inflammatory disorders.

INTRODUCTION

Acute inflammation is an essential innate immune response to self-protect from harmful stimuli, including irritants and pathogens. However, a chronic inflammatory response is deleterious and leads to several inflammatory diseases (Okin and Medzhitov, 2012). Autophagy is a fundamental cell-survival process

that plays a broad homeostatic role in cleaning cells by removing toxic wastes including determinants of surplus inflammation (Deretic et al., 2013; Ma et al., 2013). Recently, several studies have demonstrated the importance of autophagy in protecting against chronic inflammatory diseases (Deretic and Klionsky, 2018).

One of the most critical components of the inflammatory response are inflammasomes, which are molecular complexes that are activated by diverse danger signals of pathogenic and non-pathogenic origin, resulting in the production of the pro-inflammatory cytokines such as interleukin-1β (IL-1β) and IL-18 (Jo et al., 2016; Schroder et al., 2018). A well-studied inflammasome is composed of the NLRP3 (NACHT, LRR, and PYD domains containing protein 3) protein that complexes with ASC (PYCARD) (apoptosis-associated speck-like protein containing a CARD) to form a caspase-1-activating complex that then cleaves and activates IL-1β (Guo et al., 2015). Dysregulation of NLRP3 inflammasome has been linked with several chronic inflammatory, infectious, and autoimmune diseases (Lamkanfi and Dixit, 2012; Strowig et al., 2012). Autophagy has emerged as one of the essential processes in controlling excess inflammasome activation. By mediating the degradation of obsolete mitochondria and by degrading inflammasome components including NLRP3, autophagy keeps unnecessary and aberrant activation of inflammasomes under check (Shi et al., 2012; Yan et al., 2015; Zhong et al., 2016).

Immunity-related GTPase M (IRGM) belongs to a family of interferon-inducible GTPases (IRGs), one of the strongest cell-autonomous resistance systems to intracellular pathogens (Hunn et al., 2011). After a landmark study showing the importance of human IRGM in anti-mycobacterial autophagy (Singh et al., 2006), several genome-wide association studies identified SNPs in the *IRGM* gene and a deletion polymorphism in *IRGM* promoter region as being strongly associated with Crohn's disease (CD) and tuberculosis (Brest et al., 2011; Che et al., 2010; McCarroll et al., 2008; Parkes et al., 2007; Wellcome Trust Case Control, 2007; Craddock et al., 2010). Later, IRGM was genetically and functionally linked with several other chronic
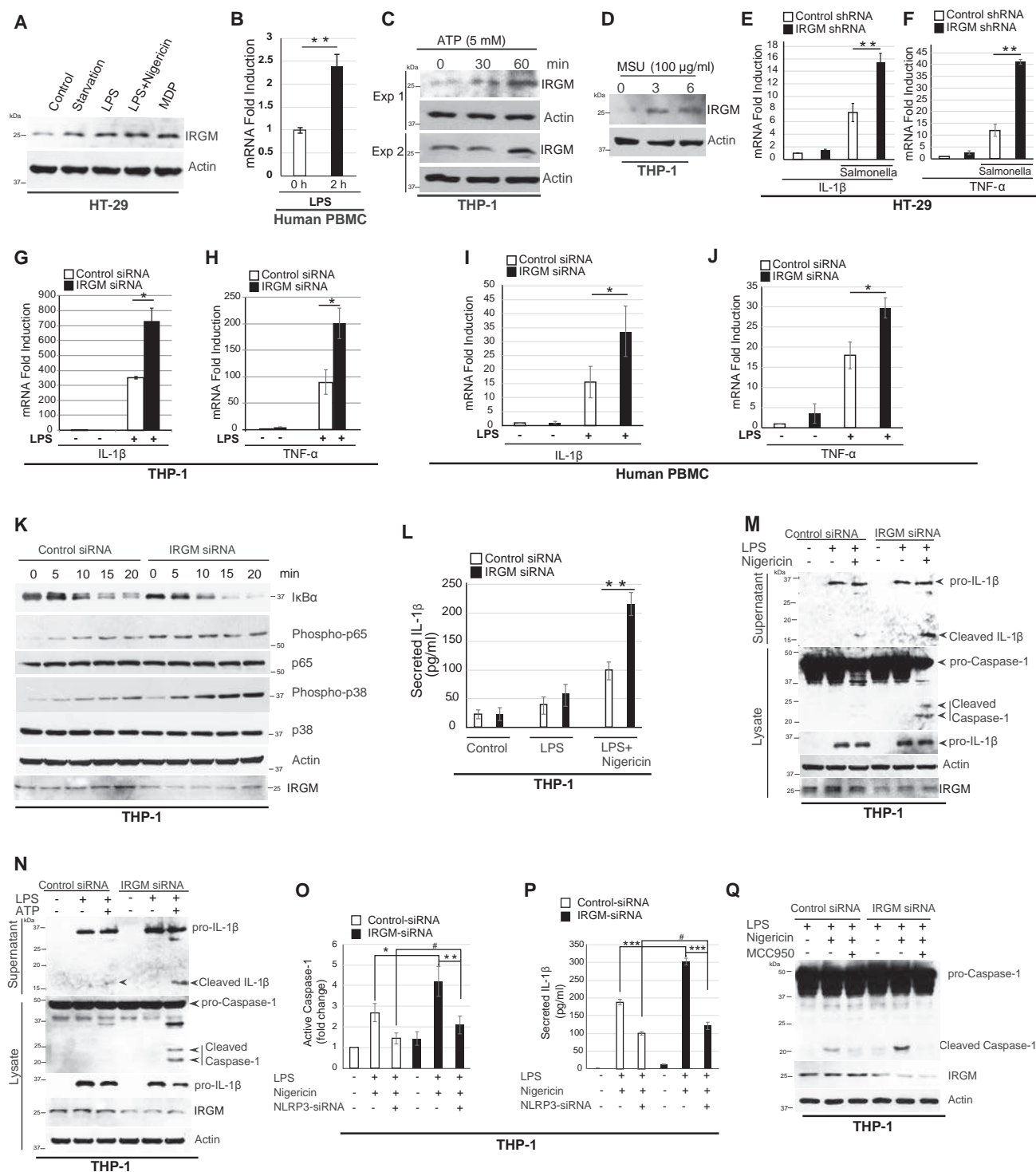
Figure 1. IRGM Suppresses Pro-inflammatory Response and NLRP3-Inflammasome Activation

(A) Human colon epithelial HT-29 cells were starved (2 hr) or stimulated with LPS (100 ng/mL, 2 hr) alone or in combination with nigericin (10 μM, 1 hr) or with MDP (10 μg/mL, 6 hr), and immunoblotting was performed with lysates.

(B) Human PBMCs from healthy volunteers were exposed to LPS (100 ng/mL), and total RNA was subjected to qRT-PCR using IRGM TaqMan probe.

(C and D) THP-1 cells were stimulated with inflammasome inducers (C) ATP or (D) MSU crystals for the indicated time periods, and extracts were subjected to western blotting with IRGM antibody.

inflammatory and autoimmune diseases (Baskaran et al., 2014; Burada et al., 2012; Glas et al., 2013; Yang et al., 2014). Given the linkage of IRGM with so many inflammatory and autoimmune disorders, it is surprising that IRGM's mechanism of action in regulating inflammation remains unclear.

In this study, our work reveals that human IRGM and its mice ortholog Irgm1 control inflammation by suppressing the activation of NLRP3 inflammasomes. Mechanistically, we found that IRGM physically complexes with NLRP3 inflammasome components and obstructs inflammasome assembly. IRGM interacts with SQSTM1/p62 (henceforth, p62) and mediates p62-dependent selective autophagy of NLRP3 and ASC. Thus, by restricting inflammasome activity, IRGM protects from pyroptosis. Further, we found that mouse Irgm1 suppresses the colon inflammation by inhibiting NLRP3 inflammasome in a DSS-induced colitis mouse model. Taken together, this work identifies a direct role of IRGM in suppressing the inflammation and provides a basis for its protective role in inflammatory diseases including Crohn's.

RESULTS

Human IRGM Suppresses Pro-inflammatory Cytokine Response

Human *IRGM* is mainly expressed in cells of myeloid and epithelial origin, and this expression is increased following exposure of interferon (IFN)-γ (Chauhan et al., 2015). IRGM expression in the colon epithelial cell line HT-29 is increased under starvation conditions and by treatment of cells with the pathogen-associated-molecular-patterns (PAMPs) such as lipopolysaccharide (LPS) and muramyl dipeptide (MDP) (Figures 1A and S1A). In human peripheral blood mononuclear cells (PBMCs), IRGM expression was increased on treatment with LPS (Figure 1B). Further, the treatment of THP-1 cells with danger-associated molecular patterns (DAMPs) such as ATP, MSU (Monosodium urate), and cholesterol crystals increased protein expression of IRGM (Figures 1C, 1D, and S1B). The expression of IRGM was increased on infection of THP-1 cells with *Salmonella typhimurium* (SL1433) (Figure S1C). Thus, *IRGM* expression is induced by DAMPs, PAMPs, and microbes in innate immune cells.

Next, we investigated the role of IRGM in modulating the pro-inflammatory responses induced by LPS treatment and by Salmonella infection. The control and IRGM stable knockdown HT-29 human colon epithelial cells were infected with *Salmonella*

typhimurium, and the expression of sentinel pro-inflammatory genes *Il1b*, *Tnfa*, *Il18*, and *Rantes* were monitored by qRT-PCR. As compared to the control cells, IRGM-depleted cells mounted a stronger pro-inflammatory response (Figures 1E, 1F, S1D, and S1E). Similarly, in THP-1 cells, the LPS induced *Il1b* and *Tnfa*, expression was further increased in IRGM small interfering RNA (siRNA) knockdown cells (Figures 1G and 1H). In these cells, *Il18* expression was increased but not significantly, and *Rantes* expression was not affected (Figures S1F and S1G). Further, human PBMCs from healthy donors showed enhanced production of pro-inflammatory cytokine *Il1b* and *Tnfa* when IRGM was knockdown (Figures 1I and 1J). Furthermore, the secretion of IL-6 and tumor necrosis factor alpha (TNF-α) was significantly higher in IRGM-depleted THP-1 cells as compared to the control cells (Figures S1H and S1I). Taken together, the data suggest that IRGM suppresses the pro-inflammatory cytokine response.

To determine the pro-inflammatory signaling pathway controlled by IRGM, we performed a time-course experiment of LPS treatment in control and IRGM-depleted THP-1 cells. As compared to the control cells, the IRGM-depleted cells have lesser IκBα that was degraded faster with LPS treatment (Figure 1K). In the agreement, phospho-NF-κB-p65 levels were higher in IRGM-depleted cells at all the time points (Figure 1K). A previous study in mice indicated the role of p38 MAPK signaling pathway in Irgm1-mediated LPS (TLR4) induced a pro-inflammatory cytokine response (Bafica et al., 2007). Here, in human cells, we found a similar increase in phospho-p38 in IRGM knockdown cells compared to control cells (Figure 1K) suggesting that human IRGM inhibit both NF-κB and p38 MAPK pro-inflammatory signaling pathways to control pro-inflammatory cytokine response.

We note that our several attempts to generate an IRGM knockout human monocytic cell line or a colon epithelial cell lines by different CRISPR-CAS9 methods were unsuccessful. Consequently, in this study, we used siRNA (THP-1 and PBMCs) or small hairpin RNA (shRNA) (HT-29 cells) to transiently or stably knock down the human IRGM; typical knockdown efficiency in any given cell or cell line (PBMC, THP-1, HT-29) was found to be 40%–60% (Figures S1J–S1L).

IRGM Limits NLRP3 Inflammasome Activation

IL-1β is translated as pro-IL-1β that stays in inactivated form until a second signal activates inflammasomes leading to pro-IL-1β

(E and F) HT-29 control and IRGM knockdown cells were infected with *S. typhimurium* (1:10 MOI, 8 hr), and the total RNA was subjected to qRT-PCR with (E) IL-1β and (F) TNF-α.

(G–J) The total RNA isolated from the LPS-stimulated (100 ng/mL, 2 hr) control and IRGM siRNA-transfected (G and H) THP-1 cells or (I and J) PBMCs from five healthy donors were subjected to qRT-PCR for the indicated genes. For (G) and (H), n = 3, mean ± SE, *p < 0.05, Student's unpaired t test. For (I) and (J), n = 5, mean ± SE, *p < 0.05, Student's paired t test.

(K) The LPS (500 ng/mL)-stimulated control and IRGM siRNA-transfected THP-1 cell lysates were subjected to immunoblotting with indicated antibodies.

(L) The supernatants from control and IRGM siRNA-transfected THP-1 cells, which were stimulated with LPS (100 ng/mL, 4 hr) alone or in combination with nigericin (5 μM, 30 min), were subjected to ELISA with IL-1β antibody.

(M and N) The western blotting was performed with control and IRGM siRNA-transfected THP-1 cells, which were stimulated with LPS (1 μg/mL for 3 hr) alone or in combination (M) with nigericin (5 μM, 30 min) or (N) with ATP (2.5 mM, 4 hr).

(O and P) Quantification of (O) active caspase-1 (FLICA assay) and (P) secreted IL-1β (ELISA) in THP-1 cells transfected with control, IRGM, and NLRP3 siRNA and treated with LPS (1 μg/mL, 3 hr) and nigericin (5 μM, 15 min).

(Q) The control and IRGM siRNA-transfected THP-1 cells were treated with LPS (1 μg/mL, 3 hr), nigericin (5 μM, 15 min), or MCC950 (1 μM) as indicated, and western blotting was performed.

Unless otherwise stated above, n = 3, mean ± SD, *p < 0.05, **p < 0.005, ***p < 0.0005, #insignificant, Student's unpaired t test. See also Figure S1.
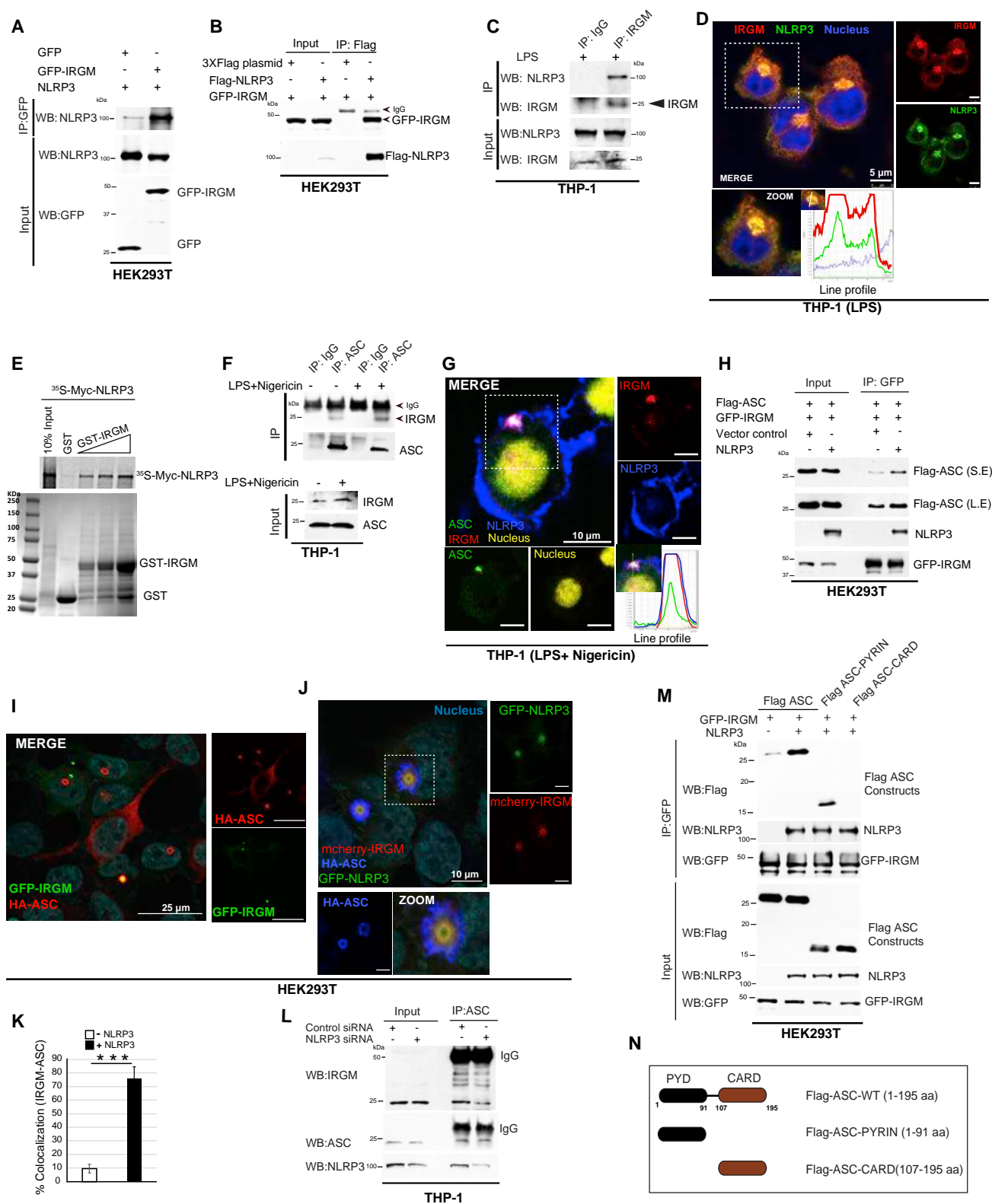
Figure 2. IRGM Interacts and Co-localizes with NLRP3 Inflammasome Components

(A and B) Co-immunoprecipitation (coIP) analysis of interaction between (A) GFP-IRGM and NLRP3 or (B) Flag-NLRP3 and GFP-IRGM in HEK293T cells lysates.

(C) IP analysis of interaction between endogenous IRGM and NLRP3 in LPS-stimulated THP-1 cells.

(legend continued on next page)

cleavage by caspase-1 to a mature form that is secreted (Choi and Ryter, 2014). We next investigated whether IRGM controls the levels of secreted IL-1β. In ELISA assays, the secreted IL-1β levels were significantly increased on silencing IRGM (Figure 1L) indicating that IRGM suppresses IL-1β cleavage and secretion. The treatment of THP-1 cells with LPS and the inflammasome inducers nigericin (Figure 1M) or ATP (Figure 1N) resulted in increased cleavage of caspase-1 and IL-1β in IRGM-depleted cells compared to the control cells. The results indicate that IRGM suppresses the cleavage of caspase-1 and IL-1β presumably by suppressing NLRP3 inflammasome. We validated this notion by depleting (by siRNA) and inhibiting (by MCC950) the NLRP3 in IRGM knockdown cells. The enhanced inflammasome activation in IRGM-depleted THP-1 cells was blunted when NLRP3 was depleted or inhibited (Figures 1O–1Q and S1M) suggesting that IRGM inhibits NLRP3 activity to suppress activation of caspase-1 and IL-1β.

IRGM Interacts and Co-localizes with NLRP3 and ASC over the Inflammasomes

Several diverse signals can activate NLRP3 leading to the oligomerization of NLRP3, the adaptor protein ASC, and the caspase-1 enzyme for the assembly of an activated inflammasome (Choi and Ryter, 2014). Since we found that IRGM suppresses cleavage of caspase-1 and IL-1β, next, we examined the mechanism by which IRGM suppresses the activity of NLRP3 inflammasome. First, we investigated whether IRGM physically associates with inflammasome components. In immunoprecipitation assays, IRGM strongly interacted with both exogenous and endogenous NLRP3 (Figures 2A–2C and S1N). The endogenous IRGM and NLRP3 interacted in THP-1 monocytes (Figure 2C), and the interaction was increased in the presence of *Salmonella typhimurium* (Figure S1N). Endogenous as well as exogenously expressed IRGM was found to be completely co-localized with the NLRP3 in the perinuclear regions of the cells (Figures 2D, S1O, and S1P). In GST pull-down assays, purified IRGM directly interacted with NLRP3 in a concentration-dependent manner (Figure 2E). Taken together, the data suggest that IRGM directly interacts and co-localizes with NLRP3.

On inflammasome activation, ASC oligomerizes with itself and with NLRP3 and caspase-1 to form an active inflammasome complex. In immunoprecipitation assays, performed in THP-1 cells, IRGM interacted with ASC, both under basal and inflammasome-inducing conditions (Figure 2F). ASC formed distinct specks in the cells that are hallmarks of inflammasome activation. Under inflammasome-inducing conditions, IRGM co-local-

ized with ASC and NLRP3 in the core region of specks (Figures 2G, S1Q, and S1R). In co-immunoprecipitation (coIP) experiments, IRGM interacted with ASC, and this interaction was increased when NLRP3 was co-expressed (Figure 2H). In agreement with this, the co-localization of overexpressed ASC structures and IRGM was dramatically increased when NLRP3 was co-expressed (Figures 2I–2K). Also, the depletion of NLRP3 reduced the ASC-IRGM interaction (Figure 2L). The data show that NLRP3 is important for bridging IRGM and ASC. Next, in a domain-mapping experiment, we found that IRGM interacts with PYRIN domain but not with the CARD domain of ASC (Figures 2M and 2N). The PYRIN is the oligomerization domain of ASC. Taken together, the data suggest that IRGM is part of NLRP3 inflammasome where it complexes with both NLRP3 and ASC.

IRGM Interferes with NLRP3 Inflammasome Assembly

To further understand the details of the NLRP3-IRGM interaction, we mapped the binding of IRGM to functional domains in NLRP3 (Figure 3A). NLRP3 is composed of PYRIN, NACHT (nucleotide binding domain or NBD), and LRR domains (Figure 3A). We found that IRGM predominantly interacted with the NACHT domain (Figure 3A). A weak interaction with LRR and almost negligible interaction with PYRIN domain were observed (Figure 3A). The NACHT domain of NLRP3 is an ATP binding domain with an ATPase activity (Duncan et al., 2007). An intact NACHT domain of NLRP3 is required for its oligomerization and activation (Duncan et al., 2007). Hence, we examined whether IRGM perturbs the oligomerization of NLRP3. Indeed, in crosslinking experiments, IRGM depletion was sufficient to increase oligomerization of NLRP3 (Figure 3B). In contrast, the oligomeric forms of overexpressed NLRP3 were reduced when IRGM was overexpressed (Figure 3C). Further, in coIP assays, IRGM was able to reduce homotypic interaction between FLAG-NLRP3 and GFP-NLRP3 (Figure 3D). Furthermore, overexpression of IRGM reduced the interaction between full-length NLRP3 and NACHT domain (Figure 3E) and also between FLAG-NACHT and mCherry-NACHT suggesting that IRGM disrupts the homo-oligomerization of the NLRP3 (Figure 3F). In immunofluorescence assays, the size of NLRP3 aggregates was reduced in the presence of IRGM (Figures S2A–S2C). Altogether, the data show that IRGM restricts the oligomerization of NLRP3.

ASC possess prion-like properties of self-association and forms branched fiber-like structure important for inflammasome activation (Cai et al., 2014). A high-resolution microscopy of ASC specks in THP-1 cells revealed a significantly larger and branched ASC specks in IRGM knockdown cells compared to

(D) Representative confocal images of THP-1 macrophages, treated with LPS and processed for immunofluorescence (IF) analysis.

(E) GST pull-down assay of in-vitro-translated and radiolabeled myc-tagged NLRP3 with GST or GST-tagged IRGM.

(F) IP analysis of interaction between endogenous IRGM and ASC in LPS+nigericin-treated THP-1 cells.

(G) Representative confocal images of THP-1 cells, treated with LPS (1 μg/mL, 3 hr) and nigericin (5 μM, 30 min) and processed for IF analysis.

(H) CoIP analysis of interaction between IRGM and ASC in HEK293T cell lysates in absence and in presence of NLRP3. S.E., short exposure; L.E., long exposure.

(I and J) Representative confocal images of HEK293T cells transiently expressing (I) GFP-IRGM and HA-ASC and (J) GFP-NLRP3, mcherry-IRGM, and HA-ASC.
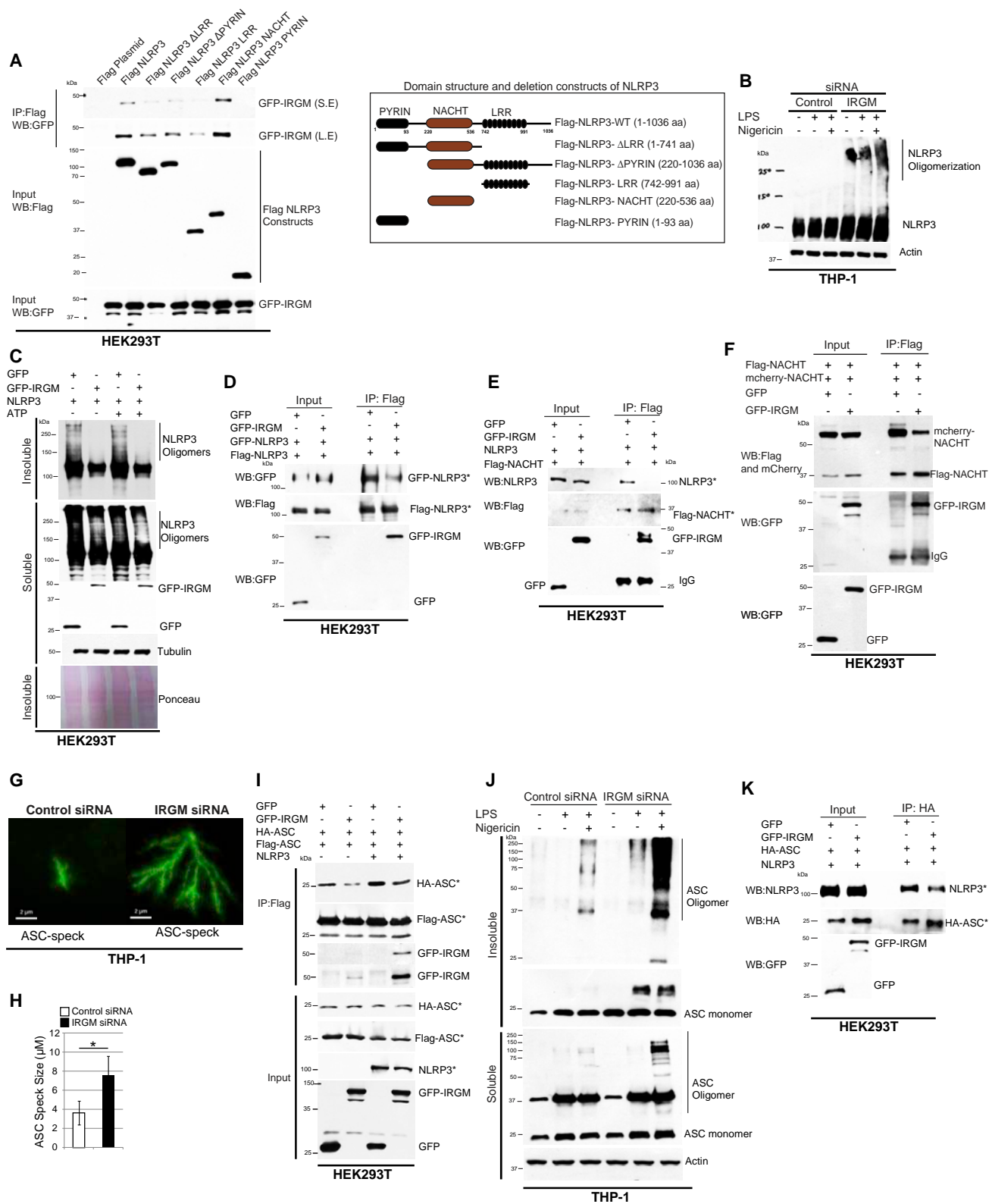
(K) The graph depicts percentage co-localization of ASC specks with IRGM in the absence and presence of NLRP3 (n = 3, mean ± SD, ***p < 0.0005).

(L) IP analysis of the interaction between endogenous IRGM and ASC in THP1 cells transfected with control siRNA or NLRP3 siRNA.

(M) CoIP analysis to map the interaction of ASC domains with IRGM in HEK293T cell lysates.

(N) The domain organization map of ASC and deletion constructs cloned as FLAG-tagged proteins. Scale bars are indicated in the respective figures.

See also Figure S1.

A

IP:Flag
WB:GFP
GFP-IRGM (S.E)
GFP-IRGM (L.E)

Input
WB:Flag
Flag NLRP3
Constructs

Input
WB:GFP
GFP-IRGM

HEK293T

Domain structure and deletion constructs of NLRP3

PYRIN NACHT LRR Flag-NLRP3-WT (1-1036 aa)
Flag-NLRP3- ΔLRR (1-741 aa)
Flag-NLRP3- ΔPYRIN (220-1036 aa)
Flag-NLRP3- LRR (742-991 aa)
Flag-NLRP3- NACHT (220-536 aa)
Flag-NLRP3- PYRIN (1-93 aa)

B

siRNA
Control   IRGM
NLRP3
Oligomerization
NLRP3
Actin
THP-1

C

Insoluble — NLRP3 Oligomers
Soluble — NLRP3 Oligomers
GFP-IRGM
GFP
Tubulin
Insoluble — Ponceau
HEK293T

D

Input   IP: Flag
WB:GFP — GFP-NLRP3*
WB:Flag — Flag-NLRP3*
GFP-IRGM
WB:GFP — GFP
HEK293T

E

Input   IP: Flag
WB:NLRP3 — NLRP3*
WB:Flag — Flag-NACHT*
WB:GFP — GFP-IRGM
GFP — IgG
HEK293T

F

Input   IP:Flag
WB:Flag and mCherry — mcherry-NACHT / Flag-NACHT
WB:GFP — GFP-IRGM / IgG
WB:GFP — GFP-IRGM / GFP
HEK293T

G

Control siRNA   IRGM siRNA
ASC-speck   ASC-speck
THP-1

H

☐ Control siRNA
■ IRGM siRNA
*
ASC Speck Size (μM)

I

IP:Flag — HA-ASC* / Flag-ASC* / GFP-IRGM / GFP-IRGM
Input — HA-ASC* / Flag-ASC* / NLRP3* / GFP-IRGM / GFP
HEK293T

J

Control siRNA   IRGM siRNA
Insoluble — ASC Oligomer / ASC monomer
Soluble — ASC Oligomer / ASC monomer / Actin
THP-1

K

Input   IP: HA
WB:NLRP3 — NLRP3*
WB:HA — HA-ASC*
WB:GFP — GFP-IRGM / GFP
HEK293T

(legend on next page)

the control cells (Figures 3G and 3H). In contrast, when IRGM was overexpressed, ASC specks were found to be significantly smaller in overexpressing cells compared to the control cells (Figures S2D–2F). The data indicate that IRGM suppresses the polymerization of ASC. To corroborate these findings, we performed biochemical assays. In coIP experiments, the overexpression of IRGM reduced interaction between HA-ASC and FLAG-ASC (Figure 3I). In western blotting experiments performed with cross-linked insoluble cellular fraction, ASC oligomerization was inhibited by overexpression of IRGM (Figure S2G). In contrast, the amount of oligomerized ASC in the insoluble fraction of the THP-1 cells was markedly increased in IRGM knockdown cells compared to the control cells (Figure 3J). Taken together, these results suggest that IRGM obstructs the oligomerization of ASC also. The interaction between NLRP3 and ASC was also reduced in the presence of IRGM (Figure 3K, see also Figure 5E), but the interaction between ASC and caspase-1 was unaffected by IRGM (Figure S2H). Overall, we found that IRGM restricts assembly of the inflammasome by impeding the homo- and hetero-oligomerization of NLRP3 and ASC.

IRGM Mediates Autophagic Degradation of NLRP3 Inflammasome Components

We found that the overexpression of IRGM reduced NLRP3 levels (Figure 4A, S2I, and S2J), while silencing IRGM by siRNA increased the total amount of endogenous NLRP3 (Figures 4B and S2K). The data indicate that IRGM mediates degradation of the NLRP3 protein.

NLRP3 is known to be degraded by both the proteasome and autophagy (Kimura et al., 2015; Song et al., 2016). The Bafilomycin A1 (BafA1, an autophagy inhibitor), but not MG132 (a proteasome inhibitor), was able to restore the IRGM-mediated degradation of NLRP3 indicating a role for autophagy in the degradation process (Figures 4C and S2L). In the absence of the essential autophagy proteins, ATG5 or ATG7, IRGM was not able to degrade NLRP3 (Figures 4D–4G and S2M) suggesting that IRGM degrades NLRP3 via autophagy process.

ASC as a part of an inflammasome was previously shown to be degraded by autophagy (Shi et al., 2012). Here, we found that overexpression of IRGM reduced ASC protein levels (Figures 4H and S2N), while IRGM depletion resulted in increased ASC amounts (Figures 4I and S2O). This finding was further supported by immunofluorescence experiments showing that the LPS and nigericin-induced ASC specks (inflammasomes) were significantly increased in number on knocking down IRGM (Figures S2P and S2Q). In contrast, overexpression of IRGM significantly reduced the total number of ASC specks (Figures S2R and S2S). These data suggest that IRGM mediates degradation of ASC. This degradation was completely restored in the presence of BafA1, but only partly in the presence of MG132 (Figures 4J and S2T). In the absence of ATG5 or ATG7, IRGM was not able to degrade ASC (Figures 4F and 4G) suggesting that IRGM degrades ASC via autophagy process.

IRGM Mediates p62-Dependent Selective Autophagy of NLRP3 Inflammasomes

p62 is a selective autophagy adaptor protein that plays a vital role in autophagic degradation of several inflammatory signaling pathway proteins including inflammasomes and their components (Chen et al., 2016; Samie et al., 2018; Shi et al., 2012). Here, we explored whether IRGM acts as a scaffold protein to mediate p62-dependent selective autophagy of NLRP3. We found that IRGM interacted and co-localized with p62 (Figures 4K and 4L). IRGM was also required for expression of p62 under basal and inflammasome-inducing conditions in THP-1 cells (Figure S3A). NLRP3 itself can interact and co-localize with p62 (Figures S3B–3D). In THP-1 cells, p62 was co-localized with NLRP3 (Figure S3D) on perinuclear structures that appeared similar to those on which IRGM and NLRP3 co-localized (Figure 2D) suggesting that all the three proteins are part of the same complex. In HEK293T cells, overexpressed IRGM, p62, and NLRP3 co-localized with each other suggesting that they are indeed in a single complex (Figure 4M). IRGM increased the interaction of p62 with both NLRP3 (Figures 4N and 4O) and ASC (Figure 4P) suggesting that IRGM is vital for bridging p62 with NLRP3- and ASC-containing inflammasomes.

Next, we asked whether p62 as a part of the IRGM-p62-NLRP3 complex is required for IRGM-mediated autophagic degradation of NLRP3. Indeed, depletion of p62 by siRNA restored IRGM-mediated NLRP3 degradation (Figures 4Q and S3E). ULK1 plays an important role in autophagy initiation, whereas Beclin1 and ATG16L1 are required for autophagosome assembly and elongation. Since IRGM interacts with ULK1, Beclin 1, and ATG16L1 for assembly of the autophagy

---

Figure 3. IRGM Impedes the Homo- and Hetero-oligomerization of NLRP3 and ASC

(A) Left panel, coIP analysis to map the binding of IRGM over the NLRP3 domains in HEK293T cell lysates. Right panel, the domain organization map of NLRP3 and deletion constructs cloned as FLAG-tagged proteins. S.E., short exposure; L.E., long exposure.

(B) The western blotting analysis of DSS cross-linked insoluble fraction of LPS and nigericin-treated control and IRGM knockdown THP-1 cells.

(C) The soluble and insoluble fractions of DSS cross-linked HEK293T cells lysates expressing NLRP3 and GFP or GFP-IRGM were subjected to western blotting.

(D–F) CoIP analysis of interaction between (D) FLAG-NLRP3 and GFP-NLRP3, (E) FLAG-NLRP3-NACHT and NLRP3, and (F) FLAG-NLRP3-NACHT and mcherrry-NLRP3-NACHT in the absence and presence of GFP-IRGM in HEK293T cells lysates.

(G) Super-resolution micrograph of control and IRGM siRNA-transfected THP-1 cells stably expressing LPS-inducible GFP-ASC.

(H) Average ASC speck size measured (n = 2, mean ± SD [40 specks], *p < 0.05).

(I) IP analysis from HEK293T cell lysates expressing HA-ASC, FLAG-ASC, and NLRP3 along with GFP control vector or GFP-IRGM vector.

(J) The western blot analysis with DSS cross-linked insoluble fraction and soluble fractions of control and IRGM knockdown THP-1 cells stimulated with LPS (1 μg/mL, 3 hr) and nigericin (5 μM, 15 min).

(K) IP analysis of interaction between NLRP3 and ASC in the absence and presence of GFP-IRGM.

*In order to reduce the artifact coming from IRGM-mediated degradation of NLRP3 and ASC, the inputs ratios were adjusted to have equal inputs in both the conditions and the IP samples were run in the same ratios as of the inputs.

Scale bars are as indicated in figures. See also Figure S2.
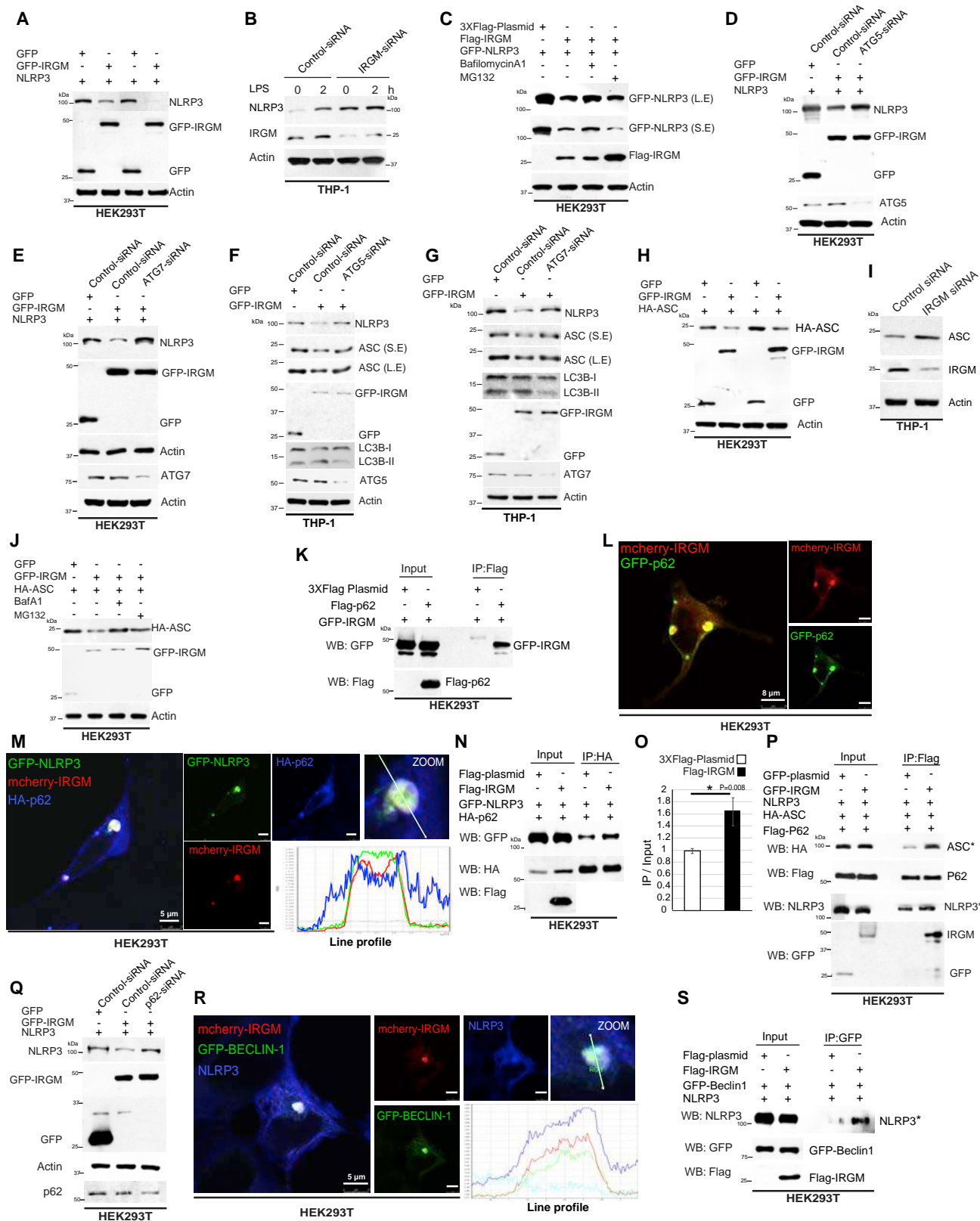
(legend on next page)

machinery (Chauhan et al., 2015), we next asked which of these autophagy proteins are utilized by IRGM for autophagy of NLRP3. NLRP3 and IRGM co-localized with all three autophagy regulatory proteins (Figures 4R, S3F, and S3G). Further, in coIP experiments, IRGM robustly increased NLRP3-Beclin1 and NLRP3-ATG16L1 interactions (Figures 4S and S3H) but did not affect NLRP3-ULK1 interaction (Figure S3I). Taken together, the data suggested a scaffolding role for IRGM in bringing the autophagy adaptor protein (p62), autophagy initiation (Beclin 1), and elongation protein (ATG16L1) over the NLRP3 inflammasomes.

We performed time-chase immunofluorescence experiments to understand whether the p62 docks to NLRP3/ASC complex first or the Beclin1/ATG16L1 reaches the complex first. The IRGM-p62-ASC showed co-localization in 5 min of stimulation, whereas ATG16L1 came later at 15 min or more prominently on 30 min post stimulation (Figures S4A and S4B). We also performed time-chase immunofluorescence experiments in overexpression system in HEK293T cells. The data show that, in the presence of p62, the NLRP3-IRGM puncta formation are fast, and all three p62, IRGM, and NLRP3 co-localized with each other 6 hr post-transfection (Figures S4C and S4D), whereas in the presence of Beclin1 the IRGM-NLRP3 complex appeared at 12 hr post-transfection (Figures S4C and S4D). Taken together, the data suggest that p62 being an adaptor protein recognizes the inflammasome first followed by docking of other autophagy proteins.

NLRC4 and AIM2 are other well-studied inflammasomes. The NLRC4 levels were unchanged, whereas, surprisingly, AIM2 levels were decreased on knocking down IRGM (Figures 5A and 5B). However, the overexpression of IRGM did not significantly affect the levels of overexpressed AIM2 in HEK293T (Figures S5C and S5D) suggesting that the reduction in AIM2 expression observed in IRGM knockdown THP-1 cells is not a direct effect of IRGM low expression but could be a secondary event. This notion is supported by negligible AIM2-IRGM co-localization (Figures S5E and S5F). Taken together, our data show that AIM2

or NLRC4 are not degraded by IRGM-mediated selective autophagy, and the discovered mechanism is specific to NLRP3.

Next, we investigated whether the LPS and inflammasome activator-induced general autophagy flux is controlled by IRGM. The results suggest that LPS-, LPS+nigericin-, and LPS+ATP-induced autophagy flux is inhibited upon IRGM depletion (Figures 5A and 5B), whereas the LPS+poly(dA-dT) (an AIM2 inflammasome inducer)-induced autophagy flux was not affected by knockdown of IRGM (Figure S5G).

IRGM mediates selective autophagy of NLRP3 and ASC and also regulates basal autophagy. We asked whether IRGM itself is an autophagy target. In cycloheximide chase experiments, we found that MG132 but not BafA1 could protect IRGM from degradation suggesting that IRGM is degraded by proteasome but not by the autophagy (Figures S5H and S5I).

Two Distinct Mechanisms Governed by IRGM Regulate NLRP3 Inflammasome Suppression

IRGM utilizes two mechanisms: (1) suppression of oligomerization and (2) autophagic degradation of NLRP3/ASC to inhibit the inflammasome activation. Next, we performed experiments to determine whether these two mechanisms are distinct or dependent on each other. In oligomerization assays, in the presence of autophagy inhibitor chloroquine, although the IRGM-mediated degradation of NLRP3 and ASC monomers (soluble fraction) was significantly restored, the oligomerization defect of NLRP3 and ASC was not rescued (Figures 5C and 5D). These data indicate that the IRGM-mediated autophagic degradation of NLRP3 and ASC is independent of IRGM-regulated inhibition of oligomerization. Next, we found that IRGM was able to inhibit the oligomerization of NLRP3, as well as ASC even in the presence of autophagy inhibitor (Figures 5E and 5F) suggesting that IRGM-mediated oligomerization defect is independent of IRGM-controlled autophagic degradation of NLRP3 and ASC.

A recent study showed that a single mutation in the GTPase domain (S47N) of IRGM makes it incompetent in interaction

---

Figure 4. IRGM Mediates Autophagic Degradation of NLRP3 and ASC

(A) Western blotting experiment with HEK293T cells expressing NLRP3 and GFP or GFP-IRGM plasmids.

(B) Western blot analysis with untreated or LPS-treated (100 ng/mL, 2 hr) control or IRGM siRNA-transfected THP-1 cells lysates.

(C) HEK293T cells expressing FLAG control vector, FLAG-IRGM, and GFP-NLRP3 were treated with MG132 or Bafilomycin A1, and lysates were subjected to western blotting. S.E., short exposure; L.E., long exposure.

(D and E) The control and (D) ATG5 siRNA or (E) ATG7 siRNA-transfected HEK293T cells expressing NLRP3, GFP, or/and GFP-IRGM were subjected to immunoblotting.

(F and G) The control and the (F) ATG5 siRNA or (G) ATG7 siRNA-transfected THP-1 cells expressing GFP or GFP-IRGM were stimulated with LPS (1 μg/mL, 3 hr), and the cell lysates were subjected to immunoblotting.

(H) HEK293T cells expressing HA-ASC and GFP or GFP-IRGM were subjected to immunoblotting.

(I) The control and IRGM siRNA-transfected THP-1 cells lysates were subjected to immunoblotting.

(J) Western blotting analysis with lysates from HEK293T cells transfected with HA-ASC and GFP or GFP-IRGM, untreated or treated with BafA1 or MG132.

(K) CoIP analysis of interaction between FLAG-p62 and GFP-IRGM in HEK293T cell lysates.

(L and M) Representative confocal images of HEK293T cells expressing (L) GFP-p62 and mcherry-IRGM (M) HA-p62, mcherry-IRGM, and GFP-NLRP3.

(N) CoIP analysis of interaction between HA-p62 and GFP-NLRP3 in the absence and presence of FLAG-IRGM.

(O) Graph depicts the quantification of GFP-NLRP3 band intensity in IP (normalized compared to inputs) (n = 3, mean ± SD, *p ≤ 0.05, Student's unpaired t test)

(P) CoIP analysis of interaction between p62 and ASC in the absence and presence of IRGM in HEK293T cell.

(Q) Analysis of degradation of NLRP3 in the absence and presence of IRGM and in HEK293T cells transfected with control siRNA and p62 siRNA.

(R) Representative confocal images of HEK293T cells expressing mcherry-IRGM, GFP-Beclin-1, and NLRP3.

(S) CoIP analysis of interaction between NLRP3 and Beclin-1 in the absence and presence of IRGM in HEK293T cells expressing the indicated plasmids.

*In order to reduce the artifact coming from IRGM-mediated degradation of NLRP3 and ASC, the inputs ratios were adjusted to have equal inputs in both the conditions, and the IP samples was run in the same ratios as of the inputs. Scale bars are as indicated in figures. S.E., short exposure; L.E., long exposure. See also Figures S2 and S3.
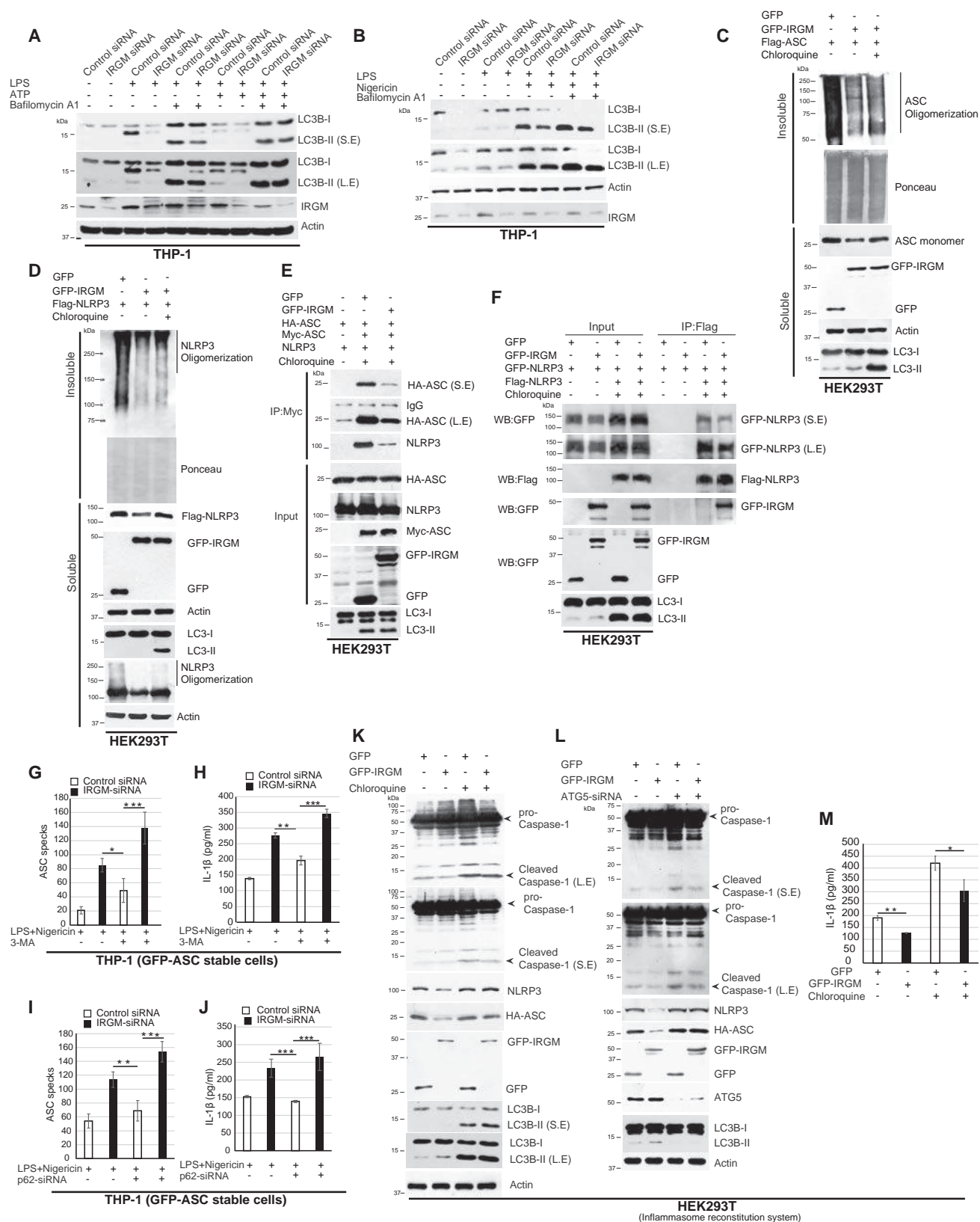
(legend on next page)

with Syntaxin 17, an autophagosome-lysosome fusion protein (Kumar et al., 2018). We found that this mutation (S47N, IRGM GTPase activity defective) in IRGM renders it inefficient in degrading NLRP3 suggesting the importance of IRGM GTPase activity in autophagy-mediated cargo degradation (Figure S5J). Very interestingly, this mutation was able to rescue the IRGM-mediated autophagic degradation of NLRP3 but not the oligomerization defect mediated by IRGM (Figure S5J). Taken together, the results suggest that IRGM controls two distinct mechanisms, autophagic degradation of NLRP3 (GTPase-dependent function) and inhibition of oligomerization of NLRP3 (GTPase-independent function).

Next, we performed several experiments to parse out the relative contribution of these two mechanisms in inhibiting NLRP3 inflammasome activation. We observed that the treatment of 3-MA (an autophagy inhibitor) results in increased inflammasomes (ASC specks) numbers and IL-1β secretion compared to the untreated THP-1 cells suggesting that autophagy reduces the NLRP3 inflammasome formation and activation (Figures 5G and 5H and S5K). We found that knockdown of IRGM induces significantly more ASC specks formation and also IL-1β secretion as compared to the 3-MA-treated THP-1 cells (Figures 5G and 5H). These data indicate that IRGM-mediated suppression of inflammasomes includes mechanisms more than autophagy-mediated degradation. The 3-MA-treated IRGM knockdown cells showed significantly higher ASC speck formation and IL-1β secretion than 3-MA-treated control cells (Figures 5G and 5H) suggesting that, in addition to autophagy-mediated suppression, the IRGM-mediated inhibition of oligomerization of inflammasomes may play a significant role in suppressing NLRP3 inflammasomes. Similar results were obtained when selective autophagic degradation of inflammasome was inhibited by knocking down of p62 in IRGM-depleted THP-1 cells (Figures 5I and 5J). Next, in HEK293T inflammasome reconstitution system, the overexpression of IRGM reduces caspase-1 cleavage (Figures 5K and 5L cf. lane 1 and 2 in SE) and also the IL-1β secretion (Figure 5M). The inhibition of autophagy (using chloroquine or ATG5 knockdown) in IRGM-overexpressing cells increased the caspase-1 cleavage and also IL-1β secretion but to lesser extent than autophagy-inhibited control cells (Figures 5K and 5L, cf. lane 4 with 3 in long exposure [L.E.], Figure 5M) suggesting yet again that IRGM mediates suppression of NLRP3 inflammasome by at least two distinct mechanisms discovered here.

IRGM Protects from Pyroptosis

Pyroptosis is an inflammatory cell death mediated by activation of inflammasomes (also called pyroptosomes) (Fernandes-Alnemri et al., 2007; Shi et al., 2017). Annexin V and propidium iodide (PI) double staining was used to access the role of IRGM in pyroptosis. Due to the formation of pores, pyroptotic cells are mainly stained by PI (PI is cell membrane impermeant). Annexin-V cannot distinguish between apoptotic cells and pyroptotic cells and stains both of them. In flow cytometry experiments, on exposure of inflammatory threats, both the apoptotic and pyroptotic populations were increased considerably in IRGM-depleted THP-1 cells compared to control cells (Figures 6A–6G, S6A, and S6B). These results suggest that IRGM protects the cells from inflammation-induced cell death. In the lactate dehydrogenase (LDH) release assays, there was a significant increase in the LDH amount in supernatant collected from LPS- and DAMP-treated IRGM-depleted THP-1 cells compared to the control cells (Figure S6C). Similar results were obtained using a trypan blue exclusion assay that accesses the integrity of the cell membrane during cell death (Figure S6D).

Recent studies identified Gasdermin D (GSDMD) as an effector protein for pyroptosis (Liu et al., 2016; Shi et al., 2015). In agreement with caspase-1 cleavage data presented in Figure 1, the cleavage of GSDMD was increased in IRGM-depleted cells compared to the control cells (Figure 6H). In agreement with flow cytometry data, apoptosis was also increased in IRGM knockdown cells compared to control cells as clear from the enhanced PARP1 (Poly [ADP-ribose] polymerase 1) cleavage (Figure 6I). Taken together, our data show that IRGM protects cells from inflammation-induced cell death.

Next, we blocked the caspase's activity using the pan-caspase inhibitor z-VAD-FMK or selective caspase-1 inhibitor Ac-YVAD-CMK to determine whether the inflammatory cell death observed in IRGM-depleted cells is caspase dependent or independent. The results (both by flow cytometry and western blotting) show that z-VAD-FMK and Ac-YVAD-CMK can block pyroptosis and also can reduce apoptosis induced by IRGM depletion (Figures 6J–6N) suggesting that IRGM suppresses caspase-1-dependent inflammatory cell death.

Mouse Irgm1 Suppresses the Gut Inflammation by Inhibiting the NLRP3 Inflammasome Activation

Although human IRGM and mouse Irgm1 possess biochemical differences, they have been found to have overlapping functions,

---

Figure 5. Both Autophagy and Inflammasome Assembly Defect Triggered by IRGM Leads to Inhibition of NLRP3 Inflammasome Activation

(A and B) Analysis of regulation of autophagy flux in control and IRGM knockdown THP-1 cells stimulated with LPS (1 μg/mL, 3 hr) or (A) LPS +ATP (5 mM, 60 min) or (B) LPS+nigericin (5 μM, 15 min) with or without Bafilomycin A1 (300 nM, 3 hr).

(C and D) Western blotting analysis of the DSS cross-linked insoluble and soluble fraction of HEK293T cells expressing (C) FLAG-ASC or (D) FLAG-NLRP3 and GFP or GFP-IRGM in absence or presence of chloroquine (50 μM, 5 hr).

(E and F) CoIP analysis of interaction between (E) myc-ASC and HA-ASC or (F) GFP-NLRP3 and FLAG-NLRP3 in the absence and presence of GFP-IRGM in HEK293T cells treated or untreated with chloroquine (50 μM, 5 hr).

(G–J) Average number of (G and I) ASC specks or (H and J) secreted IL-1 β from THP-1 GFP-ASC stable cells transfected with control and IRGM siRNA and stimulated with LPS+nigericin, in the absence and presence of (G and H) 3-MA (10 mM, 3 hr) or (I and J) p62 siRNA (n = 3, mean ± SD, *p ≤ 0.05, **p ≤ 0.005, ***p ≤ 0.0005, Student's unpaired t test).

(K–M) HEK293T cells transfected with NLRP3, HA-ASC, caspase-1, pro-IL-1β, GFP-IRGM, and GFP for 30 hr and (K and M) treated with chloroquine for next 6 hr or (L) transfected with ATG5 siRNA. (K and L) The cell lysates were subjected to western blotting and (M) supernatant used in ELISA to measure IL-1β. (n = 3, mean ± SD, *p ≤ 0.05, **p ≤ 0.005, Student's unpaired t test).

S.E., short exposure; L.E., long exposure. See also Figures S4 and S5.
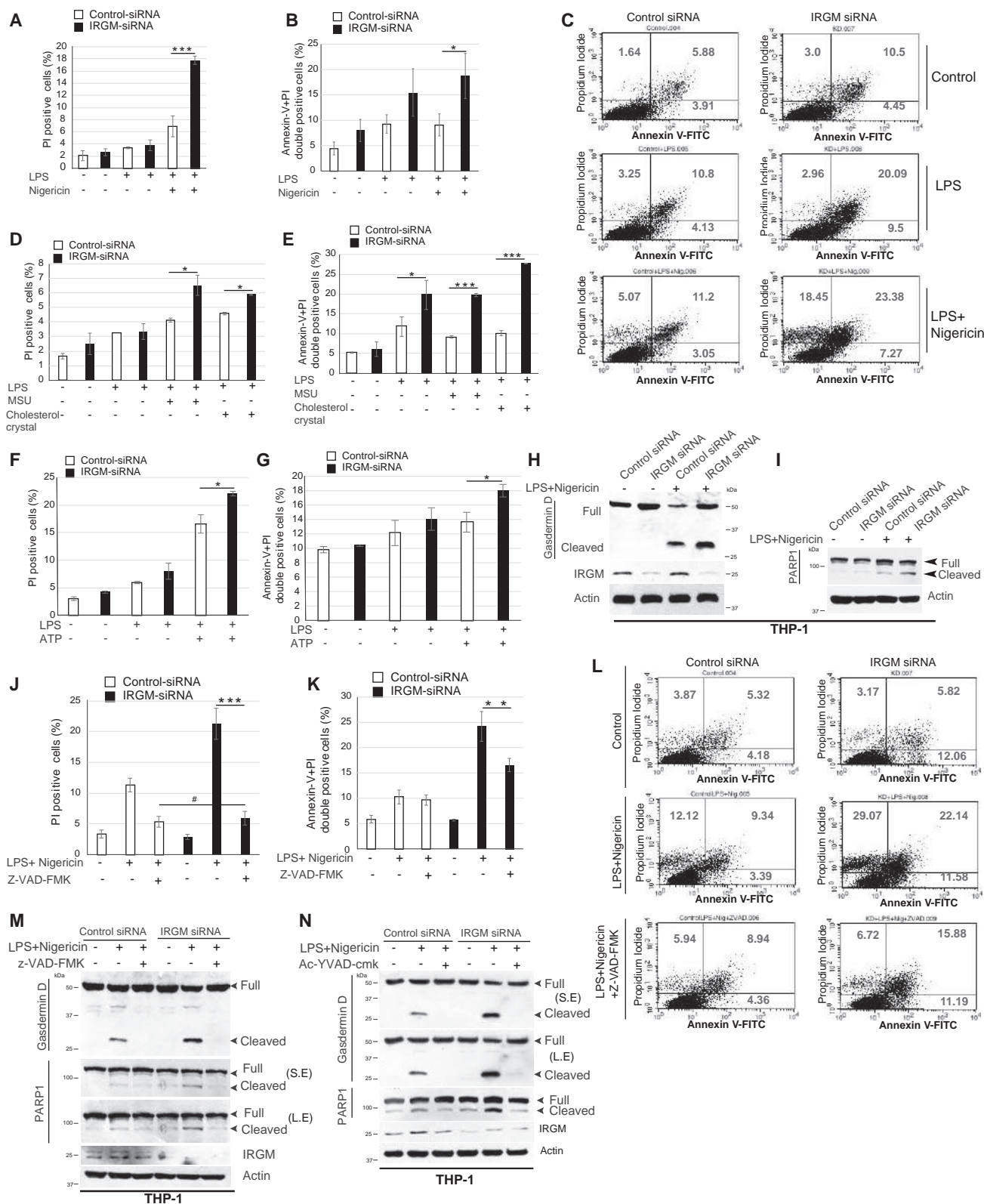
particularly as related to innate immunity and autophagy. Given the role of IRGM in inflammatory bowel disease (IBD) and Crohn's, we utilized the dextran-sulfate (DSS)-induced colitis model to investigate the role of Irgm1 in Nlrp3 inflammasome activation. $Irgm1^{-/-}$ mice have previously been shown to exhibit enhanced inflammation following DSS administration (Liu et al., 2013). Consistent with this report, we found here that the administration of DSS led to decreased body weight and colon length in $Irgm1^{-/-}$ mice relative to those responses in littermate $Irgm1^{+/+}$ mice (Figures S7A–S7D). Like in human colon cells, the expression of $IL-1\beta$, $TNF-\alpha$, and $IL-18$ was significantly increased in DSS-treated $Irgm1^{-/-}$ compared to $Irgm1^{+/+}$ mice (Figure 7A). Next, we scrutinized the expression of inflammasome components. In untreated mice, Nlrp3 expression was increased in $Irgm1^{-/-}$ mice compared to $Irgm1^{+/+}$ mice (Figure 7B); however, expression of ASC was not different (Figure 7B). In DSS-treated mice, the expression of both Nlrp3 and ASC in bone-marrow-derived macrophages and colon was more in $Irgm1^{-/-}$ mice compared to $Irgm1^{+/+}$ mice (Figures 7C and 7D). Also, ASC oligomerization was considerably higher in $Irgm1^{-/-}$ mice compared to $Irgm1^{+/+}$ mice (Figures 7C and 7D). In a cross-linking experiment with bone marrow-derived macrophages (BMDMs), both ASC and Nlrp3 oligomerization was found to be increased in $Irgm1^{-/-}$ mice compared $Irgm1^{+/+}$ mice (Figures 7E and S7E; STAR Methods). Under inflammasome-inducing conditions, the active caspase-1 amount was significantly higher in $Irgm1^{-/-}$ mice compared to control $Irgm1^{+/+}$ mice (Figure 7F). Similar to human cell lines studies, the basal autophagy and also the LPS-induced autophagy flux in BMDMs were dependent on the expression of Irgm1 (Figure 7G). Altogether, the data show that Irgm1, like its human ortholog, suppresses the activation of the NLRP3 inflammasome by inhibiting its assembly and by increasing autophagy.

Next, we analyzed whether increased Nlrp3 inflammasome activation is the cause for exacerbated outcomes of DSS-induced colitis in $Irgm1$ knockout mice. MCC950 is the most potent and the most specific small-molecule inhibitor of activation of NLRP3 known to date (Coll et al., 2015; Strangward et al., 2018; Yao et al., 2018). We investigated whether selective pharmacologic blockade of the Nlrp3 inflammasome using MCC950 would reduce the colitis symptoms in $Irgm1^{-/-}$ mice. Indeed, we found that all the intensified outcomes of DSS-induced colitis in the Irgm1 knockout mice were reversed in

the presence of MCC950 (Figures 7H–7J, S7F, and S7G). At molecular levels, in colon tissues, the increased amount of inflammasome components (Nlrp3, ASC monomers, and dimers) and also the enhanced inflammasome activity as measured by cleaved caspase-1 by western blot (Figure 7K) and fluorescent caspase-1 cleavage assay (Figure 7L) in $Irgm1^{-/-}$ mice were reversed by MCC950 treatment. Next, we isolated the BMDMs from these mice and induced the inflammasome (using LPS+ nigericin) in the absence and presence of MCC950. Again, the data show that inactivation of Nlrp3 by MCC950 considerably reduced the enhanced inflammasome activity in $Irgm1^{-/-}$ mice as measured by fluorescent caspase-1 cleavage assay (Figure 7M) and western blotting (Nlrp3, ASC dimer, and caspase-1 cleavage) (Figure 7N). Next, we used a genetic approach to determine whether enhanced inflammasome activation in Irgm1$^{-/-}$ mice BMDMs is because of increased activation of the Nlrp3/ASC inflammasome. In LPS+nigericin-stimulated BMDMs, the increased caspase-1 cleavage (Figures 7O and S7H) and the IL-1β secretion (Figures 7P and S7H) in $Irgm1^{-/-}$ mice BMDMs was blunted when Nlrp3 was depleted in these cells using siRNA.

Taken together, several lines of evidence suggest that NLRP3 activation is the primary factor behind enhanced inflammasome activity in IRGM-depleted cells, and also the activation of NLRP3 inflammasome is one of the major reasons for exacerbated outcomes of DSS-induced colitis in the $Irgm1$ knockout mice. We conclude that the IRGM/Irgm1 suppresses the NLRP3 inflammasome to keep the gut inflammation under check.

DISCUSSION

In landmark genome-wide association studies conducted by Wellcome Trust Case Control Consortium to understand the genetic determinants of inflammatory diseases, SNPs in the *IRGM* locus were found to be strongly associated with Crohn's disease (Wellcome Trust Case Control, 2007; Craddock et al., 2010). Later, several studies showed similar genetic linkages of IRGM with Crohn's disease and other inflammatory and autoimmune diseases in different populations worldwide (Baskaran et al., 2014; Glas et al., 2013; Li et al., 2014; McCarroll et al., 2008; Xia et al., 2017; Yang et al., 2014). Most of these studies suggested a protective role of IRGM against the

Figure 6. IRGM Protects from Caspase-Dependent Inflammatory Cell Death

(A and B) Flow cytometry analysis of control and IRGM siRNA knockdown cells untreated or treated with LPS (1 μg/mL, 3 hr) and nigericin (5 μM, 30 min). Bar graphs show percentage of (A) PI positive or (B) Annexin V/PI double-positive cells.

(C) Representative dot plot showing flow cytometry analysis of control and IRGM siRNA knockdown cells untreated or treated with LPS and nigericin.

(D–G) Flow cytometry analysis of control and IRGM siRNA knockdown cells untreated or treated with LPS, MSU, cholesterol crystal, and ATP as indicated. Bar graph showing percentage of (D and F) PI positive and (E and G) Annexin V/PI double-positive cells.

(H and I) The control and IRGM siRNA-transfected THP-1 cells treated with LPS and nigericin were subjected to immunoblot analysis with (H) Gasdermin D or (I) PARP1 and actin antibodies.

(J and K) Flow cytometry analysis of control and IRGM siRNA knockdown cells untreated or treated with LPS, nigericin, and Z-VAD-FMK (5 μM, 30 min) as indicated. Bar graph showing the percentage of (J) PI positive and (K) Annexin V/PI double-positive cells.

(L) Representative dot plot is showing flow cytometry analysis of control and IRGM siRNA knockdown cells untreated or treated with LPS and nigericin and Z-VAD FMK as depicted.

(M and N) Western blot analysis of control and IRGM knockdown THP-1 cells untreated or treated with LPS, nigericin, and (M) Z-VAD-FMK or (N) Ac-YVAD-cmk. Unless otherwise stated, n = 3, mean ± SD, *p ≤ 0.05**p ≤ 0.005, ***p ≤ 0.0005, #insignificant, Student's unpaired t test). S.E., short exposure; L.E., long exposure. See also Figure S6.
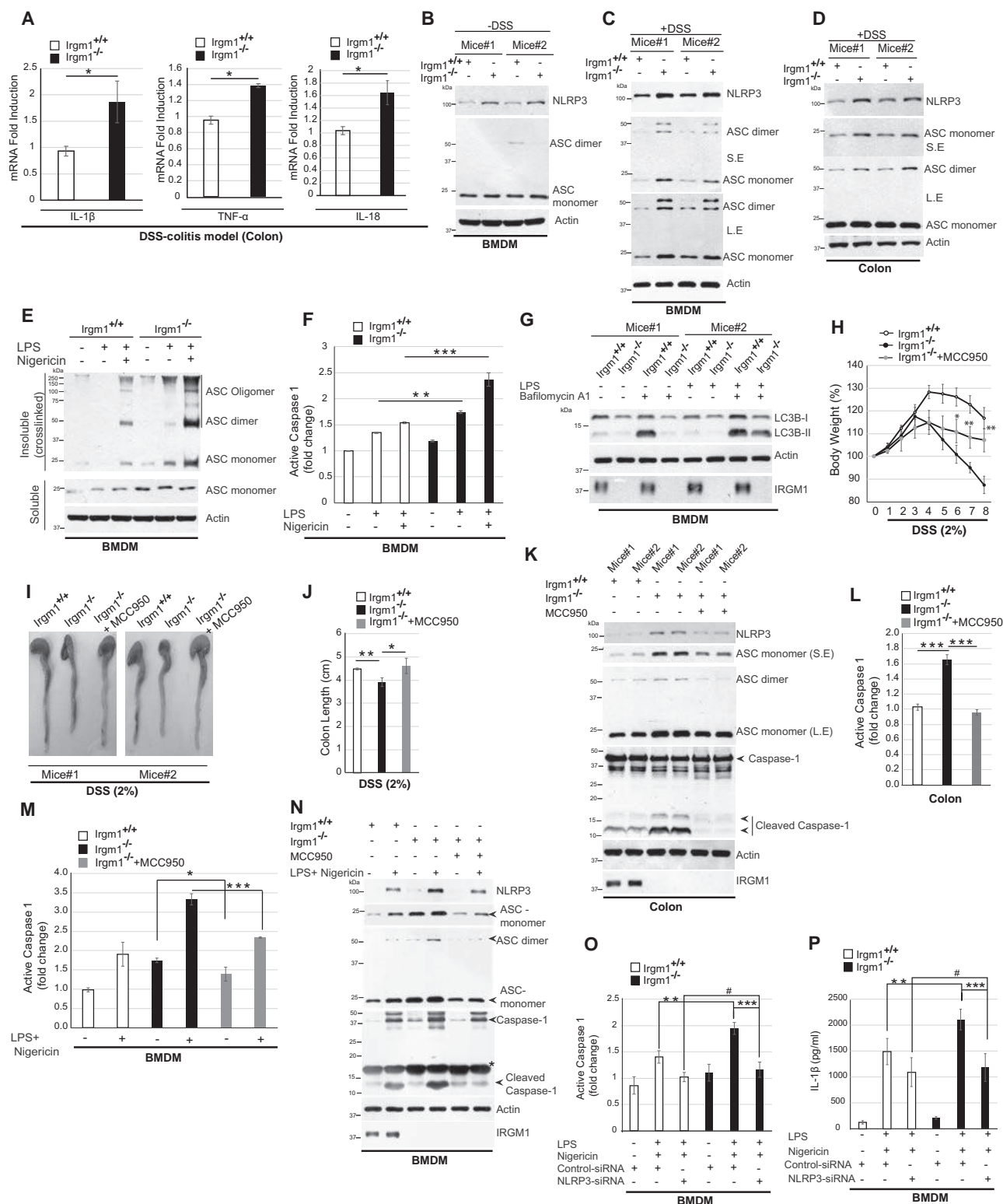
Figure 7. Irgm1 Suppresses Colitis via Inhibition of NLRP3 Inflammasome

(A) The qPCR analysis from the total RNA isolated from colon of DSS-treated *Irgm1*$^{+/+}$ and *Irgm1*$^{-/-}$ knockout mice (n = 3, mean ± SE, *p < 0.05, Student's unpaired t test).

(legend continued on next page)

inflammatory diseases; however, none of the studies revealed the mechanism(s).

This study defined the mechanism by which IRGM/Irgm1 regulates cellular inflammation in immune and gut epithelial cells (Figure S7I). We found here that IRGM suppresses IL-1β production by limiting the activation of the NLRP3 inflammasome (Figure S7I). Remarkably, IRGM performs this function by complexing directly with inflammasome components including NLRP3 and ASC. By binding to the oligomerization domain (NACHT) of NLRP3, it impedes the oligomerization of NLRP3. IRGM also hinders polymerization of ASC protein (Figure S7I), which is a key event for activation of inflammasome (Cai et al., 2014; Lu et al., 2014). Previous studies demonstrated the role of autophagy process in limiting the IL-1β production, and one of the mechanisms was by degrading the inflammasome and its components in a p62-dependent manner (Shi et al., 2012). Here, we found that IRGM is a key player in mediating p62-dependent selective autophagy of NLRP3 and ASC (Figure S7I). Thus, IRGM limits IL-1β production by two mechanisms: (1) by interfering in the assembly of the inflammasome and (2) by mediating autophagy of inflammasome. In the inflammatory bowel disease experimental mice model, Irgm1 suppresses the colitis by inhibiting the NLRP3 inflammasome. Taken together, this work revealed IRGM-mediated anti-inflammatory immune homeostasis mechanism by which IRGM could be protective against inflammatory diseases.

As compared to humans, where IRGM is a lone member of the IRG family, mice have 20 more homologs of Irgm1, presumably providing the compensation when the Irgm1 is knockout in the mice. Although human IRGM and mice Irgm1 are of different size (21 versus 47 kDa), they are strikingly similar in the regulation of autophagy and inflammation.

The dysregulated NLRP3 inflammasome has been linked to the pathogenesis of several inflammatory diseases including gout, type 2 diabetes, cancer, cardiovascular diseases, Alzheimer's, Parkinson's, and prion diseases (Alcocer-Gómez and Cordero, 2017; Lee et al., 2013; Song et al., 2017). Also, mutations in the NLRP3 gene have been linked with a range of dominantly inherited auto-inflammatory diseases (Masters et al., 2009). Therefore, it is of high importance to the medical science to understand the mechanisms by which the cell restrains the activation of NLRP3 inflammasome and IL-1β production. For

similar reasons, understanding the protective nature of IRGM in human inflammatory diseases is crucial. This study delineates both. The therapeutic strategies to increase IRGM activity or targeting the IRGM-NLRP3 interaction could be useful for treating IRGM- and NLRP3-associated diseases.

STAR★METHODS

Detailed methods are provided in the online version of this paper and include the following:

- KEY RESOURCES TABLE
  - Cell Culture
  - Isolation of human peripheral blood mononuclear cells (PBMCs)
  - Plasmid Constructs and Transfection
  - Transient transfection with siRNA
  - Transient transfection with plasmids
  - Enzyme-linked immunosorbent assay (ELISA)
  - Bacterial Infections
  - ASC Oligomerization Assay
  - Western Blotting
  - Antibodies and dilution
  - Co-Immunoprecipitation
  - GST pull-down assay
  - Immunofluorescence Analysis
  - Cycloheximide chase assay
  - Macrophage differentiation and stimulation
  - Chloroform-methanol protein precipitation
  - Annexin-V/Propidium Iodide staining
  - Caspase-1 inhibition Assay
  - Soluble and Insoluble proteins fractionation
  - RNA Isolation and Quantitative Real-time PCR
  - Caspase 1 activity measurement assay
  - Mice experiments
  - Mice Bone marrow cells isolation and differentiation into macrophages
- DATA AND SOFTWARE ACCESSIBILITY

SUPPLEMENTAL INFORMATION

Supplemental Information includes seven figures and can be found with this article online at https://doi.org/10.1016/j.molcel.2018.11.018.

(B and C) Western blot analysis with BMDM lysates from (B) untreated or (C) DSS-treated Irgm1+/+ and Irgm1−/− knockout mice with indicated antibodies.

(D) Western blot analysis with colon lysates from DSS-treated Irgm1+/+ and Irgm1−/− mice.

(E) Western blotting analysis of cross-linked insoluble and soluble cell fraction from LPS- and nigericin-treated Irgm1+/+ and Irgm1−/− BMDMs.

(F) The quantification of activated caspase-1 (FLICA assay) in LPS- and nigericin-treated Irgm1+/+ and Irgm1−/− BMDM lysates.

(G) Western blotting analysis from LPS- and Bafilomycin A1-treated Irgm1+/+ and Irgm1−/− BMDM cell lysates.

(H) Graph depicting the percentage of change in body weight during the course of DSS treatment.

(I) Representative pictures of colons of DSS- and MCC950-treated and -untreated Irgm1+/+ and Irgm1−/− mice.

(J) Graph depicts colon length of DSS- and MCC950-treated and -untreated Irgm1+/+ and Irgm1−/− mice.

(K) Western blot analysis from colon lysates of DSS- and MCC950-treated and -untreated Irgm1+/+ and Irgm1−/− mice.

(L and M) The quantification of activated caspase-1 (FLICA assay) in (L) colon lysates of DSS and MCC950 or (M) BMDM lysates of LPS, nigericin, and MCC950 (1 μM)-treated and -untreated Irgm1+/+ and Irgm1−/− mice.

(N) Western blot analysis from of LPS, nigericin, and MCC950 (1 μM)-treated or -untreated BMDM cell lysates from Irgm1+/+ and Irgm1−/− mice. *Non-specific.

(O and P) Quantification of active caspase-1 (caspase-1 FLICA assay) (O) and secreted IL-1β (ELISA) (P) in LPS- (100 ng/mL, 3 hr) and nigericin- (5 μM, 15 min) treated NLRP3-depleted BMDMs from Irgm1+/+ and Irgm1−/− mice.

S.E., short exposure; L.E., long exposure. n = 3, mean ± SD, *p < 0.05, **p < 0.005, ***p < 0.0005, #insignificant Student's t test unpaired). See also Figure S7.

AUTHOR CONTRIBUTIONS

Santosh Chauhan secured funding, conceived the project, designed experiments, and wrote the manuscript. S.M., K.K.J., P.N., Swati Chauhan, S.P.K., S.K.D., P.K.S., and A.J. carried out the experiments. G.A.T. provided critical inputs for experiments and edited the manuscript.

DECLARATION OF INTERESTS

The authors declare no competing interests.

REFERENCES

Alcocer-Gómez, E., and Cordero, M.D. (2017). NLRP3 inflammasome: Common nexus between depression and cardiovascular diseases. Nat. Rev. Cardiol. 14, 124.

Bafica, A., Feng, C.G., Santiago, H.C., Aliberti, J., Cheever, A., Thomas, K.E., Taylor, G.A., Vogel, S.N., and Sher, A. (2007). The IFN-inducible GTPase LRG47 (Irgm1) negatively regulates TLR4-triggered proinflammatory cytokine production and prevents endotoxemia. J. Immunol. 179, 5514–5522.

Baskaran, K., Pugazhendhi, S., and Ramakrishna, B.S. (2014). Association of IRGM gene mutations with inflammatory bowel disease in the Indian population. PLoS ONE 9, e106863.

Brest, P., Lapaquette, P., Souidi, M., Lebrigand, K., Cesaro, A., Vouret-Craviari, V., Mari, B., Barbry, P., Mosnier, J.F., Hébuterne, X., et al. (2011). A synonymous variant in IRGM alters a binding site for miR-196 and causes deregulation of IRGM-dependent xenophagy in Crohn's disease. Nat. Genet. 43, 242–245.

Burada, F., Plantinga, T.S., Ioana, M., Rosentul, D., Angelescu, C., Joosten, L.A., Netea, M.G., and Saftoiu, A. (2012). IRGM gene polymorphisms and risk of gastric cancer. J. Dig. Dis. 13, 360–365.

Cai, X., Chen, J., Xu, H., Liu, S., Jiang, Q.X., Halfmann, R., and Chen, Z.J. (2014). Prion-like polymerization underlies signal transduction in antiviral immune defense and inflammasome activation. Cell 156, 1207–1222.

Chauhan, S., Mandell, M.A., and Deretic, V. (2015). IRGM governs the core autophagy machinery to conduct antimicrobial defense. Mol. Cell 58, 507–521.

Chauhan, S., Kumar, S., Jain, A., Ponpuak, M., Mudd, M.H., Kimura, T., Choi, S.W., Peters, R., Mandell, M., Bruun, J., et al. (2016). TRIMs and Galectins Globally Cooperate and TRIM16 and Galectin-3 Co-direct Autophagy in Endomembrane Damage Homeostasis. Dev. Cell 39, 13–27.

Che, N., Li, S., Gao, T., Zhang, Z., Han, Y., Zhang, X., Sun, Y., Liu, Y., Sun, Z., Zhang, J., et al. (2010). Identification of a novel IRGM promoter single nucleotide polymorphism associated with tuberculosis. Clin. Chim. Acta 411, 1645–1649.

Chen, M., Meng, Q., Qin, Y., Liang, P., Tan, P., He, L., Zhou, Y., Chen, Y., Huang, J., Wang, R.F., and Cui, J. (2016). TRIM14 inhibits cGAS degradation mediated by selective autophagy receptor p62 to promote innate immune responses. Mol. Cell 64, 105–119.

Choi, A.J., and Ryter, S.W. (2014). Inflammasomes: Molecular regulation and implications for metabolic and cognitive diseases. Mol. Cells 37, 441–448.

Coll, R.C., Robertson, A.A., Chae, J.J., Higgins, S.C., Muñoz-Planillo, R., Inserra, M.C., Vetter, I., Dungan, L.S., Monks, B.G., Stutz, A., et al. (2015). A small-molecule inhibitor of the NLRP3 inflammasome for the treatment of inflammatory diseases. Nat. Med. 21, 248–255.

Craddock, N., Hurles, M.E., Cardin, N., Pearson, R.D., Plagnol, V., Robson, S., Vukcevic, D., Barnes, C., Conrad, D.F., Giannoulatou, E., et al.; Wellcome Trust Case Control Consortium (2010). Genome-wide association study of CNVs in 16,000 cases of eight common diseases and 3,000 shared controls. Nature 464, 713–720.

Deretic, V., and Klionsky, D.J. (2018). Autophagy and inflammation: A special review issue. Autophagy 14, 179–180.

Deretic, V., Saitoh, T., and Akira, S. (2013). Autophagy in infection, inflammation and immunity. Nat. Rev. Immunol. 13, 722–737.

Duncan, J.A., Bergstralh, D.T., Wang, Y., Willingham, S.B., Ye, Z., Zimmermann, A.G., and Ting, J.P. (2007). Cryopyrin/NALP3 binds ATP/dATP, is an ATPase, and requires ATP binding to mediate inflammatory signaling. Proc. Natl. Acad. Sci. USA 104, 8041–8046.

Fernandes-Alnemri, T., Wu, J., Yu, J.W., Datta, P., Miller, B., Jankowski, W., Rosenberg, S., Zhang, J., and Alnemri, E.S. (2007). The pyroptosome: A supramolecular assembly of ASC dimers mediating inflammatory cell death via caspase-1 activation. Cell Death Differ. 14, 1590–1604.

Glas, J., Seiderer, J., Bues, S., Stallhofer, J., Fries, C., Olszak, T., Tsekeri, E., Wetzke, M., Beigel, F., Steib, C., et al. (2013). IRGM variants and susceptibility to inflammatory bowel disease in the German population. PLoS ONE 8, e54338.

Guo, H., Callaway, J.B., and Ting, J.P. (2015). Inflammasomes: Mechanism of action, role in disease, and therapeutics. Nat. Med. 21, 677–687.

Henry, S.C., Daniell, X., Indaram, M., Whitesides, J.F., Sempowski, G.D., Howell, D., Oliver, T., and Taylor, G.A. (2007). Impaired macrophage function underscores susceptibility to Salmonella in mice lacking Irgm1 (LRG-47). J. Immunol. 179, 6963–6972.

Hunn, J.P., Feng, C.G., Sher, A., and Howard, J.C. (2011). The immunity-related GTPases in mammals: A fast-evolving cell-autonomous resistance system against intracellular pathogens. Mamm. Genome 22, 43–54.

Jo, E.K., Kim, J.K., Shin, D.M., and Sasakawa, C. (2016). Molecular mechanisms regulating NLRP3 inflammasome activation. Cell. Mol. Immunol. 13, 148–159.

Kimura, T., Jain, A., Choi, S.W., Mandell, M.A., Schroder, K., Johansen, T., and Deretic, V. (2015). TRIM-mediated precision autophagy targets cytoplasmic regulators of innate immunity. J. Cell Biol. 210, 973–989.

Kumar, S., Jain, A., Farzam, F., Jia, J., Gu, Y., Choi, S.W., Mudd, M.H., Claude-Taupin, A., Wester, M.J., Lidke, K.A., et al. (2018). Mechanism of Stx17 recruitment to autophagosomes via IRGM and mammalian Atg8 proteins. J. Cell Biol. 217, 997–1013.

Lamkanfi, M., and Dixit, V.M. (2012). Inflammasomes and their roles in health and disease. Annu. Rev. Cell Dev. Biol. 28, 137–161.

Lee, H.M., Kim, J.J., Kim, H.J., Shong, M., Ku, B.J., and Jo, E.K. (2013). Upregulated NLRP3 inflammasome activation in patients with type 2 diabetes. Diabetes 62, 194–204.

Li, Y., Feng, S.T., Yao, Y., Yang, L., Xing, Y., Wang, Y., and You, J.H. (2014). Correlation between IRGM genetic polymorphisms and Crohn's disease risk: A meta-analysis of case-control studies. Genet. Mol. Res. 13, 10741–10753.

Liu, B., Gulati, A.S., Cantillana, V., Henry, S.C., Schmidt, E.A., Daniell, X., Grossniklaus, E., Schoenborn, A.A., Sartor, R.B., and Taylor, G.A. (2013). Irgm1-deficient mice exhibit Paneth cell abnormalities and increased susceptibility to acute intestinal inflammation. Am. J. Physiol. Gastrointest. Liver Physiol. 305, G573–G584.

Liu, X., Zhang, Z., Ruan, J., Pan, Y., Magupalli, V.G., Wu, H., and Lieberman, J. (2016). Inflammasome-activated gasdermin D causes pyroptosis by forming membrane pores. Nature *535*, 153–158.

Lu, A., Magupalli, V.G., Ruan, J., Yin, Q., Atianand, M.K., Vos, M.R., Schröder, G.F., Fitzgerald, K.A., Wu, H., and Egelman, E.H. (2014). Unified polymerization mechanism for the assembly of ASC-dependent inflammasomes. Cell *156*, 1193–1206.

Ma, Y., Galluzzi, L., Zitvogel, L., and Kroemer, G. (2013). Autophagy and cellular immune responses. Immunity *39*, 211–227.

Masters, S.L., Simon, A., Aksentijevich, I., and Kastner, D.L. (2009). Horror autoinflammaticus: The molecular pathophysiology of autoinflammatory disease (*). Annu. Rev. Immunol. *27*, 621–668.

McCarroll, S.A., Huett, A., Kuballa, P., Chilewski, S.D., Landry, A., Goyette, P., Zody, M.C., Hall, J.L., Brant, S.R., Cho, J.H., et al. (2008). Deletion polymorphism upstream of IRGM associated with altered IRGM expression and Crohn's disease. Nat. Genet. *40*, 1107–1112.

Okin, D., and Medzhitov, R. (2012). Evolution of inflammatory diseases. Curr. Biol. *22*, R733–R740.

Parkes, M., Barrett, J.C., Prescott, N.J., Tremelling, M., Anderson, C.A., Fisher, S.A., Roberts, R.G., Nimmo, E.R., Cummings, F.R., Soars, D., et al.; Wellcome Trust Case Control Consortium (2007). Sequence variants in the autophagy gene IRGM and multiple other replicating loci contribute to Crohn's disease susceptibility. Nat. Genet. *39*, 830–832.

Samie, M., Lim, J., Verschueren, E., Baughman, J.M., Peng, I., Wong, A., Kwon, Y., Senbabaoglu, Y., Hackney, J.A., Keir, M., et al. (2018). Selective autophagy of the adaptor TRIF regulates innate inflammatory signaling. Nat. Immunol. *19*, 246–254.

Schroder, K., Kanneganti, T.D., Shao, F., and Broz, P. (2018). Mechanisms and Consequences of Inflammasome Activation. J. Mol. Biol. *430*, 131–132.

Shi, C.S., Shenderov, K., Huang, N.N., Kabat, J., Abu-Asab, M., Fitzgerald, K.A., Sher, A., and Kehrl, J.H. (2012). Activation of autophagy by inflammatory signals limits IL-1β production by targeting ubiquitinated inflammasomes for destruction. Nat. Immunol. *13*, 255–263.

Shi, J., Zhao, Y., Wang, K., Shi, X., Wang, Y., Huang, H., Zhuang, Y., Cai, T., Wang, F., and Shao, F. (2015). Cleavage of GSDMD by inflammatory caspases determines pyroptotic cell death. Nature *526*, 660–665.

Shi, J., Gao, W., and Shao, F. (2017). Pyroptosis: Gasdermin-mediated programmed necrotic cell death. Trends Biochem. Sci. *42*, 245–254.

Singh, S.B., Davis, A.S., Taylor, G.A., and Deretic, V. (2006). Human IRGM induces autophagy to eliminate intracellular mycobacteria. Science *313*, 1438–1441.

Song, H., Liu, B., Huai, W., Yu, Z., Wang, W., Zhao, J., Han, L., Jiang, G., Zhang, L., Gao, C., and Zhao, W. (2016). The E3 ubiquitin ligase TRIM31 attenuates NLRP3 inflammasome activation by promoting proteasomal degradation of NLRP3. Nat. Commun. *7*, 13727.

Song, L., Pei, L., Yao, S., Wu, Y., and Shang, Y. (2017). NLRP3 inflammasome in neurological diseases, from functions to therapies. Front. Cell. Neurosci. *11*, 63.

Strangward, P., Haley, M.J., Albornoz, M.G., Barrington, J., Shaw, T., Dookie, R., Zeef, L., Baker, S.M., Winter, E., Tzeng, T.C., et al. (2018). Targeting the IL33-NLRP3 axis improves therapy for experimental cerebral malaria. Proc. Natl. Acad. Sci. USA *115*, 7404–7409.

Strowig, T., Henao-Mejia, J., Elinav, E., and Flavell, R. (2012). Inflammasomes in health and disease. Nature *481*, 278–286.

Wellcome Trust Case Control, C.; Wellcome Trust Case Control Consortium (2007). Genome-wide association study of 14,000 cases of seven common diseases and 3,000 shared controls. Nature *447*, 661–678.

Xia, Q., Wang, M., Yang, X., Li, X., Zhang, X., Xu, S., Shuai, Z., Xu, J., Fan, D., Ding, C., and Pan, F. (2017). Autophagy-related IRGM genes confer susceptibility to ankylosing spondylitis in a Chinese female population: A case-control study. Genes Immun. *18*, 42–47.

Yan, Y., Jiang, W., Liu, L., Wang, X., Ding, C., Tian, Z., and Zhou, R. (2015). Dopamine controls systemic inflammation through inhibition of NLRP3 inflammasome. Cell *160*, 62–73.

Yang, D., Chen, J., Shi, C., Jing, Z., and Song, N. (2014). Autophagy gene polymorphism is associated with susceptibility to leprosy by affecting inflammatory cytokines. Inflammation *37*, 593–598.

Yao, C., Veleva, T., Scott, L., Jr., Cao, S., Li, L., Chen, G., Jeyabal, P., Pan, X., Alsina, K.M., Abu-Taha, I., et al. (2018). Enhanced cardiomyocyte NLRP3 inflammasome signaling promotes atrial fibrillation. Circulation. Published online May 25, 2018. https://doi.org/10.1161/CIRCULATIONAHA.118.035202.

Zhong, Z., Umemura, A., Sanchez-Lopez, E., Liang, S., Shalapour, S., Wong, J., He, F., Boassa, D., Perkins, G., Ali, S.R., et al. (2016). NF-κB restricts inflammasome activation via elimination of damaged mitochondria. Cell *164*, 896–910.

Cancer Research

RNA-Binding RING E3-Ligase DZIP3/hRUL138 Stabilizes Cyclin D1 to Drive Cell-Cycle and Cancer Progression

Srinivasa P. Kolapalli, Rinku Sahu, Nishant R. Chauhan, et al.

Updated version	Access the most recent version of this article at: doi:10.1158/0008-5472.CAN-20-1871
Supplementary Material	Access the most recent supplemental material at: http://cancerres.aacrjournals.org/content/suppl/2020/10/16/0008-5472.CAN-20-1871.DC1

Visual Overview	**A diagrammatic summary of the major findings and biological implications:** http://cancerres.aacrjournals.org/content/81/2/315/F1.large.jpg

Cited articles	This article cites 63 articles, 23 of which you can access for free at: http://cancerres.aacrjournals.org/content/81/2/315.full#ref-list-1

E-mail alerts	Sign up to receive free email-alerts related to this article or journal.
Reprints and Subscriptions	To order reprints of this article or to subscribe to the journal, contact the AACR Publications Department at pubs@aacr.org.
Permissions	To request permission to re-use all or part of this article, use this link http://cancerres.aacrjournals.org/content/81/2/315. Click on "Request Permissions" which will take you to the Copyright Clearance Center's (CCC) Rightslink site.

CANCER RESEARCH | MOLECULAR CELL BIOLOGY

RNA-Binding RING E3-Ligase DZIP3/hRUL138 Stabilizes Cyclin D1 to Drive Cell-Cycle and Cancer Progression 🄰🄲
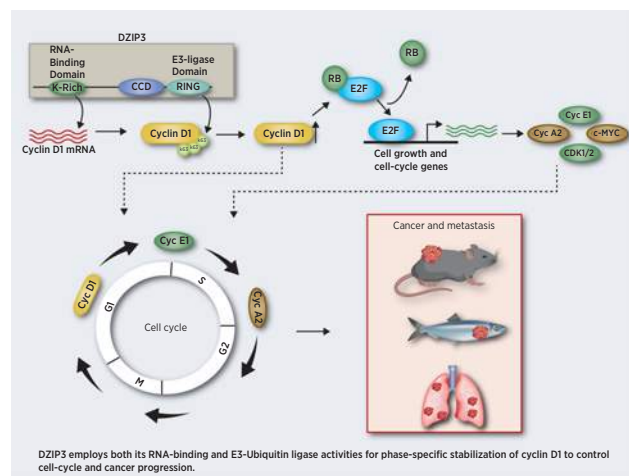
Srinivasa P. Kolapalli[1], Rinku Sahu[1], Nishant R. Chauhan[1], Kautilya K. Jena[1], Subhash Mehto[1], Saroj K. Das[2], Ashish Jain[3], Manaswini Rout[4], Rupesh Dash[5], Rajeeb K. Swain[4], David Y. Lee[6], Tor Erik Rusten[3], Santosh Chauhan[1], and Swati Chauhan[5]

ABSTRACT

DZIP3/hRUL138 is a poorly characterized RNA-binding RING E3-ubiquitin ligase with functions in embryonic development. Here we demonstrate that DZIP3 is a crucial driver of cancer cell growth, migration, and invasion. In mice and zebrafish cancer models, DZIP3 promoted tumor growth and metastasis. In line with these results, DZIP3 was frequently overexpressed in several cancer types. Depletion of DZIP3 from cells resulted in reduced expression of Cyclin D1 and a subsequent G_1 arrest and defect in cell growth. Mechanistically, DZIP3 utilized its two different domains to interact and stabilize Cyclin D1 both at mRNA and protein levels. Using an RNA-binding lysine-rich region, DZIP3 interacted with the AU-rich region in 3′ untranslated region of Cyclin D1 mRNA and stabilized it. Using a RING E3-ligase domain, DZIP3 interacted and increased K63-linked ubiquitination of Cyclin D1 protein to stabilize it. Remarkably, DZIP3 interacted with, ubiquitinated, and stabilized Cyclin D1 predominantly in the G_1 phase of the cell cycle, where it is needed for cell-cycle progression. In agreement with this, a strong positive correlation of mRNA expression between DZIP3 and Cyclin D1 in different cancer types was observed. Additionally, DZIP3 regulated several cell cycle proteins by modulating the Cyclin D1–E2F axes. Taken together, this study demonstrates for the first time that DZIP3 uses a unique two-pronged mechanism in its stabilization of Cyclin D1 to drive cell-cycle and cancer progression.

Significance: These findings show that DZIP3 is a novel driver of cell-cycle and cancer progression via its control of Cyclin D1 mRNA and protein stability in a cell-cycle phase-dependent manner.

Graphical Abstract: http://cancerres.aacrjournals.org/content/canres/81/2/315/F1.large.jpg.

DZIP3 employs both its RNA-binding and E3-Ubiquitin ligase activities for phase-specific stabilization of cyclin D1 to control cell-cycle and cancer progression.

[1]Cell and Cancer Biology Lab, Institute of Life Sciences, Bhubaneswar, Odisha, India. [2]Centre for Biotechnology, Siksha 'O' Anusandhan (Deemed to be University), Bhubaneswar, Odisha, India. [3]Centre for Cancer Cell Reprogramming, Institute of Clinical Medicine, Faculty of Medicine, University of Oslo, Oslo; Department of Molecular Cell Biology, Institute for Cancer Research, Oslo University Hospital, Oslo, Norway. [4]Vascular Biology Lab, Institute of Life Sciences, Bhubaneswar, Odisha, India. [5]Gene Therapy and Cancer Lab, Institute of Life Sciences, Bhubaneswar, Odisha, India. [6]Department of Internal Medicine, Radiation Oncology, and University of New Mexico Comprehensive Cancer Center, University of New Mexico School of Medicine, Albuquerque, New Mexico.

Note: Supplementary data for this article are available at Cancer Research Online (http://cancerres.aacrjournals.org/).

S.P. Kolapalli and R. Sahu contributed equally to this work.

N.R. Chauhan and K.K. Jena contributed equally to this work.

Corresponding Authors: Santosh Chauhan, Cell and Cancer Biology Lab, Institute of Life Sciences, Bhubaneswar 751023, Odisha, India. Phone: 7077702598; E-mail: schauhan@ils.res.in; and Swati Chauhan, Gene Therapy and Cancer Lab, Institute of Life Sciences, Bhubaneswar 751023, Odisha, India. Phone: 91-674-2301476; E-mail: swaticchauhan09@gmail.com

Introduction

The human genome encodes more than 600 E3 ligases and a similar number of RNA-binding proteins (RBP) with a variety of functions in protein and RNA metabolism (1, 2). RNA-binding RING E3 ligases (RBRL) are a unique group of a small number of proteins (20 in number) with a remarkable capability of regulating both RNA and protein metabolism, and also coupling them (3–7). However, the RBRL family proteins remain poorly characterized. Given the role of these proteins in cancer progression and innate immunity (5, 6, 8), it is crucial to understand the mechanisms by which the RBRLs regulate the turnover of their target RNA and proteins.

The DAZ (Deleted in Azoospermia) family genes are essential for gametogenesis and other developmental processes (9). DAZ family proteins interact with several other zinc finger proteins, including DZIP1, DZIP2 (DZIP1L), and DZIP3. DZIP1 and DZIP1L are centrosomal proteins and have been shown to regulate the Hedgehog signaling pathway, ciliogenesis, and cell cycle (10–12). DZIP3 (DAZ-interacting protein 3) is a poorly characterized RNA-binding RING-H2 ubiquitin E3 ligase, which was originally identified as a Hepatitis B virus interacting protein (13). The RNA-binding and E3 ligase functions of DZIP3 were more clearly identified in a recent study where it was shown to interact with HOTAIR (a long noncoding RNA)

to mediate ubiquitination and degradation of Ataxin 1 (14). DZIP3 is important for controlling the genes during embryonic development (15, 16). DZIP3 interacts with CARM1 (an arginine methyltransferase) and acts as a transcriptional coactivator of estrogen receptor alpha-responsive genes (17). Although DZIP3 is undercharacterized, the studies indicate that it is a multifunctional protein.

In eukaryotic cells, the levels of cell-cycle proteins are precisely maintained to ensure an orderly progression of the cell cycle. Dysregulated expression of cell-cycle proteins can result in uncontrolled cell growth and cancer. Cyclin D1 plays a critical role in cell-cycle progression. Overexpression of Cyclin D1 is a driving feature in a large number of cancer types, including leukemia, head and neck, breast, non–small cell lung cancer, and prostate (18, 19). Multiple mechanisms comprising genomic alterations, posttranscriptional regulation, and posttranslational protein stabilization result in Cyclin D1 overexpression leading to a deregulated cell cycle, resulting in uncontrolled cell growth and cancer (18–22).

Two E3 ligase complexes, APC/C (anaphase promoting complex/cyclosome) and Skp/cullin/F-box (SCF) act by increasing K48-linked ubiquitination of cell-cycle proteins and mediate their timely degradation for precise cell-cycle progression (23). The cell-cycle protein expression is also regulated at mRNA levels by RBPs, such as HuR, which bind and stabilize the mRNA of several cell-cycle proteins, including *p53, p21, cyclin A, cyclin B1, cyclin E, cyclin D*, and *cdk1* (24–31). Another recently recognized mechanism of regulation of cyclin proteins is by deubiquitinating enzymes such as OTUD7B, USP22, and USP27 in a cell-cycle phase-specific manner (32–34). This modification antagonizes the proteasomal degradation of cell-cycle proteins, leading to their cell-cycle phase-specific stabilization. Another layer of regulation is provided by certain E3 ligases, which can increase the K63-linked ubiquitination of specific cell-cycle proteins in one particular phase of the cell cycle, resulting in their stabilization (35–37).

In this study, we found that DZIP3 is a novel oncogene with a capacity to drive cancer cells 'anchorage-independent growth, migration, and invasion. Increased expression of DZIP3 was observed in human cancer patients' tumor samples. In agreement, DZIP3 was found to be crucial for cancer progression and metastasis in mice and zebrafish. We show that DZIP3 controls cancer cell growth by regulating the cell cycle and Cyclin D1 stability. DZIP3 utilizes a two-pronged mechanism to positively regulate the expression of Cyclin D1. First, DZIP3 stabilizes the Cyclin D1 transcripts by binding to its 3′ untranslated region (UTR), and secondly, DZIP3 interacts and increases K63-linked ubiquitination of Cyclin D1 to stabilize it posttranslationally. In addition, DZIP3 controls several of the E2F transcription factor regulated cell cycle and proliferation genes, including Cyclin E1, Cyclin A2, CDK1, CDK2, and c-MYC. Taken together, this study identifies DZIP3 as a novel driver of cell-cycle and cancer progression by regulating the expression of Cyclin D1 in a unique manner.

Materials and Methods

Cell culture

Cell lines used in the study were obtained from the ATCC. MCF7, MDA-MB-231, HT-29 (RRID:CVCL_0320), UM-UC3 (RRID: CVCL_1783), HeLa (RRID:CVCL_0030), HEK293, and HEK293T (RRID:CVCL_0063) cells were cultured in DMEM supplemented with 10% fetal bovine serum (FBS, Gibco) and penicillin/streptomycin (10,000 units/mL). The cells were tested for *Mycoplasma* contamination routinely (every 2–3 months) using the PCR method. The cell lines were maintained below passage number 20.

Reagents and inhibitors

Cycloheximide (cat. #C7698; 100 μg/mL), puromycin (cat. #p8833; 2 μg/mL), thymidine (cat. #T1895; 2 mmol/L), nocodazole (cat. #M1404; 100 ng/mL), PMSF (cat. #P7626-5G) were from Sigma. Protease inhibitor (cat. #11836170001) and phosphatase inhibitors (cat. #04906845001) were obtained from Roche.

Plasmids, siRNA, and transfection

pRK5-HA-Ubiquitin-K48 (#17605; RRID: Addgene_17604), HA-Ubiquitin (#18712; RRID: Addgene_18712), pRK5-HA-Ubiquitin-K63 (#17606; RRID:Addgene_17606), and Rc/CMV Cyclin D1 HA (#8948) plasmids were purchased from Addgene. pSG5HA-DZIP3 and pSG5FLAG-DZIP3 were described previously (17). Flag-DZIP3 and Flag-DZIP3 deletion constructs were cloned in gateway cloning vectors as per standard protocol (Invitrogen). For transient knockdown, cells were transfected by electroporation using the Neon transfection system (Invitrogen) and also using INTERFERin (Polyplus) or RNAimax (Invitrogen) as per the manufacturer's instruction. For transient overexpression, Lipofectamine 2000 (Invitrogen) and CALPHOS (Clontech) were used according to the manufacturer's instructions.

CRISPR knockout cell generation

The HEK293T or MCF7 cells were transfected with DZIP3 CRISPR Cas9 (Santacruz; sc-403972) containing a pool of 3 sgRNAs along with DZIP3 HDR plasmids (Santacruz; sc-403972). After 48 hours, media were changed, and cells were selected in puromycin (2 μg/mL). Individual colonies were picked, grown, and knockout was evaluated by using Western blot analysis.

Western blotting

Cell lysates were prepared in NP-40 (FNN0021, Thermo Fisher Scientific) or RIPA buffer [20 mmol/L Tris, pH 8.0; 1 mmol/L, EDTA; 0.5 mmol/L, EGTA; 0.1% sodium deoxycholate; 150 mmol/L NaCl; 1% IGEPAL (Sigma); 10% glycerol] supplemented with protease inhibitor cocktail and 1 mmol/L PMSF. Western blotting is performed as described previously (38–40).

Cycloheximide chase assay

Cycloheximide chase assay experiments were performed by treating the cells with 100 μg/mL cycloheximide. Cell lysates were prepared at indicated time points and were subjected to Western blot analysis with indicated antibodies.

Immunoprecipitation assay

For immunoprecipitation (IP) assays, cells were lysed in NP-40 lysis buffer supplemented with protease inhibitor cocktail and 1 mmol/L PMSF for 20 minutes at 4 C and centrifuged. The supernatant was incubated with the respective antibody at 4 C for 2 hours on rotospin followed by incubation with Protein G Dynabeads (Invitrogen, #10004D) for 2 hours at 4 C. The beads were washed with 1 NP40 and 3 ice-cold PBS. The proteins were eluted from washed beads by boiling for 5 minutes in 2 SDS gel loading dye and proceeded for immunoblot analysis.

GST pull-down assay

GST pull-down assay was performed according to the methods previously described (39, 40). GST or GST-DZIP3 (CCD-RING) proteins were expressed in SoluBL21 (Amsbio), and the proteins were purified on Glutathione Sepharose 4 Fast-Flow beads (GE Healthcare). [35S]-labeled HA-CCND1 protein was *in vitro*–translated using TnT

T7–coupled reticulocyte lysate system (Promega). GST proteins were incubated with [35S]-labeled HA-CCND1 in 250 mL of NETN-E buffer (50 mmol/L Tris, pH 8.0, 100 mm NaCl, 6 mm EDTA, 6 mm EGTA, 0.5% NP-40, and 1 mm dithiothreitol supplemented with complete mini EDTA-free protease inhibitor cocktail; Roche) for 2 hours at 4°C. Then, GST beads were added, and the mixture was incubated for 30 minutes at room temperature. The beads were washed with NETN-E buffer five times, boiled with loading buffer, and subjected to SDS-PAGE. The gel was stained with Coomassie Blue and vacuum-dried. The GST or GST-DZIP3 (CCD-RING) was detected by staining with Coomassie Blue, whereas the [35S]-labeled HA-CCND1 was detected in PharosFX imager (Bio-Rad Laboratories).

Colony-forming assay

A total of 1,000 cells in 2-mL cell culture medium were seeded in triplicate in 6-well plates and allowed to grow for 2 to 3 weeks until the colonies were formed. Cells were fixed in methanol:acetic acid (3:1) for 5 minutes at room temperature and stained with 0.5% crystal violet for 15 minutes and washed with water. The images were captured using a digital camera, and colonies were counted.

MTT assay

Five thousand cells were seeded in triplicate in 25-cm^2 flask and allowed to grow for 5 days. Subsequently, at each time point, media were removed, cells were washed with PBS, and were incubated in the dark with MTT (3-[4,5-dimethylthiazolyl-2]-2,5-diphenyltetrazolium bromide; 5 mg/mL, Sigma) for 2 to 4 hours. Dye precipitates were dissolved in DMSO, and absorbance was measured at 590 nm.

In vitro scratch assay

Cells were grown in 6-well plates with a 60% to 70% confluency and were subjected to a uniform (approximately 1 mm^2 in area) scratch with 10-µL pipette tip across the width of the well. EVOS inverted fluorescence microscope (cell imaging system, Thermo Scientific) was used to measure and photomicrograph the cell migration rate after wounding at every 24 hours (0, 24, 48, and 96 hours).

Immunofluorescence

About 10^5 cells were seeded on a coverslip. The next day, cells were fixed in 4% paraformaldehyde for 10 minutes, permeabilized with 0.1% Triton X-100 for 10 minutes, and followed by blocking with 1% BSA for 30 minutes at room temperature. Further, cells were incubated with primary antibody for 1 hour at room temperature, washed thrice with PBS followed by 1-hour incubation with Alexa Flour–conjugated secondary antibody. Cells were washed thrice with PBS, mounted (Prolong gold antifade, Invitrogen), air dried, and visualized using a confocal microscope.

Proximity ligation assay

Proximity ligation assay (PLA) was performed using a Duolink *in situ* detection (Sigma #DUO92008) kit as per the manufacturer's protocol. The complete protocol is described in Supplementary Materials and Methods.

Synchronization of cells

For G$_1$ cell-cycle arrest, cells were subjected to serum starvation (DMEM without FBS) for 24 hours. For G$_1$–S arrest, MCF7 cells were subjected to double thymidine block (2 mmol/L thymidine for 16 hours followed by a release for 8 hours and treated again with 2 mmol/L thymidine for 16 hours). To arrest HEK293T cells in G$_1$–S phase, cells were cultured in 2 mmol/L thymidine for 16 hours. For G$_2$–M arrest, cells were cultured in 2 mmol/L thymidine for 16 hours, followed by

release into medium containing nocodazole (100 ng/mL) for 16 hours. The efficiency of synchronization was confirmed by propidium iodide–based cell-cycle analysis using flow cytometry.

Cell-cycle analysis

For performing cell-cycle analysis, cultured cells were harvested and washed with PBS. The cells were resuspended in PBS containing 2% FBS and fixed by adding 70% ice-cold ethanol dropwise and incubated overnight at 4 C. Next day, the cells were washed with 2 PBS and permeabilized with 0.25% Triton x-100 for 15 minutes. Then, the cells were washed with 1 PBS and resuspended in PBS containing 100 µg RNase A and incubated at 37 C for 15 minutes, followed by propidium iodide (PI) staining (10 µg/mL) at room temperature for 1 hour. Flow-cytometric analysis was performed using BD FACSCalibur. The data were analyzed using Cell Quest Pro or FlowJo software (RRID: SCR_008520).

RNA isolation and quantitative real-time PCR

RNA isolation and qRT-PCR was performed as previously described (38). Briefly, total RNA was extracted using TRIzol reagent according to the manufacturer's protocols (Invitrogen). RNA (1 µg) was used for reverse transcription using a high-capacity DNA reverse transcription kit (Applied Biosystems; cat. #4368813), and qRT-PCR was performed using Power SYBR Green PCR Master Mix (Applied Biosystems; #4367659) according to the manufacturer's protocols. The fold change in expression was calculated by the $2^{-\Delta\Delta C_t}$ methods. mRNA expression profiles were normalized to levels of housekeeping gene glyceraldehyde 3-phosphate dehydrogenase (GAPDH) in each sample. The primers used in qRT-PCR are listed in Supplementary Materials and Methods.

Ni-NTA pull-down assay

HEK-293T cells were transfected with indicated plasmids. The cells were lysed in NP-40 lysis buffer containing 6M guanidine hydrochloride for 20 minutes at 4 C. The lysates were clarified at 12,000 g for 15 minutes. Fifty microliters of Ni-NTA beads was washed with NP-40 lysis buffer and incubated with cell lysates for 4 hours at 4 C. The beads were sedimented at 2,000 g, followed by washing with 1 lysis buffer and 4 PBS. The beads were boiled in 50 µL of 2 Lamelli sample buffer and subjected to Western blot analysis with indicated antibodies.

Biotin RNA pull-down

Biotinylated RNA preparation: Template PCR fragments were generated using forward primer containing T7 RNA polymerase promoter (TAATACGACTCACTATAGGGAGA). PCR products containing the region of interest were purified for *in vitro* transcription. Biotinylated RNA transcripts were generated in a 50-µL reaction containing T7 transcription buffer, 100 mmol/L rNTPs, 40 units RNasin (cat. #N2111; Promega), 10 mmol/L Biotin-14-CTP (cat. #16519–016; Thermo Fisher Scientific), 100 ng T7 DNA template, and 1 µL of T7 RNA polymerase (cat. #EP0113; 200 u/µL). The reaction mix was incubated at 37 C for 2 hours, and RNA was purified using RNA easy spin columns (cat. #74104; Qiagen). To remove template DNA, on-column DNAse (cat. #79254; Qiagen) treatment was performed.

HEK293T cells were transiently transfected with indicated plasmid DNA. Cells were lysed using Polysome Extraction Buffer (20 mmol/L Tris-HCl pH 7.5, 100 mmol/L KCl, 5 mmol/L MgCl$_2$, and 0.5% Nonidet P-40) containing Protease inhibitor cocktail, 1 mmol/L PMSF and 200 u/mL RNase inhibitor for 10 minutes at 4 C and centrifuged. Five hundred micrograms of lysate was diluted in an equal volume of 2 TENT buffer (20 mmol/L Tris-HCl pH 8.0, 2 mmol/L EDTA

pH 8.0, 500 mmol/L NaCl, 1% (v/v) Triton X-100) and incubated with 1 µg of biotinylated RNA for 30 minutes at room temperature. Streptavidin-coated dynabeads were washed thrice with TENT buffer and added to the protein–RNA mix and further incubated on rotospin at room temperature for 30 minutes. Finally, the beads were washed thrice with TENT buffer, and the bound proteins were eluted by boiling for 5 minutes in 2 SDS-sample loading dye and subjected to Western blot analysis with indicated antibody.

Human breast cancer tissue microarray, IHC, and scoring

Human breast cancer tissue array slides were purchased from US Biomax, Inc. (#BR1008a and #BRM961a). Details of BR1008a are as follows: human breast carcinoma, lymph node metastatic carcinoma, and adjacent normal tissue microarray containing 46 cases of invasive ductal carcinoma, neuroendocrine carcinoma, 3 medullary carcinomas, 40 metastatic carcinomas (4 metastatic carcinomas matched with breast carcinoma), 10 adjacent normal tissue, single core per block. Details of BRM961a are as follows: human breast carcinoma with matched metastatic carcinoma or breast tissue microarray, containing 48 cases of breast carcinoma, 36 metastatic carcinomas (35 matched with breast carcinoma), 12 matched cancer adjacent or adjacent normal breast tissue, single core per block. DZIP3 IHC staining is described in Supplementary Methods and Materials.

Mice xenograft and lung metastasis model

The animal work was performed in accordance with a protocol approved by Institutional Animal Care and Use Committee, ILS. Six- to 8-week-old BALB/C-nude male mice weighing 16 to 20 g were maintained under specific pathogen-free conditions at the Institutional animal experimental facility. The tumor xenograft model was established by subcutaneous injection of DZIP3 shRNA knockdown and control shRNA UC3 cells suspension under sterile conditions, and the cell number was adjusted to 5×10^6 cells in PBS containing 50% (V/V) Matrigel (BD corning) into right and left flanks, respectively (n 7 mice). After 8 days, tumor volume was measured every day until the volume reached 1,000 mm^3 in a group. The mice (n 7) were sacrificed, and tumors were collected for further analysis. For tumor volume analysis, mean ± SEM tumor volume was plotted (using Excel) for each experimental group.

For the lung metastasis study, 2×10^5 MDA-MB-231 control shRNA and DZIP3 shRNA cells were injected into the lateral tail vein of BALB/C-nude male mice (n 3). Eight weeks after injection, mice were sacrificed, and lungs were dissected out to count numbers of tumor nodules and other analysis.

Zebrafish xenograft

Animal work was performed in accordance with a protocol approved by the Institutional Animal Care and Use Committee, ILS. The tumor was developed in Zebrafish (Danio rerio) [Tg(fli1:nEGFP)] using the protocol described previously (41). The complete protocol is described in Supplementary Material and Methods.

Migration and invasion assay

Trypsinized cells were washed with PBS and resuspended in serum-free medium. Cells were plated at a density of 10^4 per well in the inserts (Costar, 8.0 µm). For invasion assay, inserts were coated with 100 µL Matrigel (BD Biosciences) before plating cells. The inserts were placed into 24-well plates containing 500 µL DMEM containing FBS (chemoattractant). After 24 hours of incubation, the cells inside the insert were completely removed by wiping with a cotton swab, and the

meshes were fixed and stained with crystal violet. Migration/invasion was quantitated by manual counting using microsope.

Results

DZIP3 is an important driver for growth, migration, and invasion of cancer cells

To understand the cellular functions of DZIP3, we generated stable DZIP3 shRNA knockdown cell lines of different origins (Supplementary Fig. S1A). We observed a significant growth defect in the knockdown cells (transient and stable) compared with the control cells in all the cell lines we checked (**Fig. 1A**; Supplementary Fig. S1B and S1C). Clonogenic assays are gold standard to assess the oncogenic potential of a single cell to grow into a colony under *in vitro* conditions. DZIP3-depleted MCF7 cells were highly attenuated for colony formation as compared with the control cells (**Fig. 1B**). Next, we tested whether the overexpression of DZIP3 will result in increased cell growth. Indeed, transient overexpression of DZIP3 in HEK293 cells resulted in increased cell growth (Supplementary Fig. S1D) and considerably increased capability to form colonies in clonogenic assays (**Fig. 1C**). We performed wound-healing assays (or scratch assays) to evaluate the migration capacity of DZIP3 knockdown cells. MCF7 cells depleted of DZIP3 showed a reduction in migration capability and wound closure as compared with control cells (**Fig. 1D**). In transwell migration assays and Matrigel invasion assays, we found significantly reduced migration and invasion of DZIP3 knockdown cells (**Fig. 1E** and **F**). Also, in soft-agar assays a significant decrease in anchorage-independent growth was observed in DZIP3 knockdown cells as compared with the control cells (**Fig. 1G**). Taken together, the data show that DZIP3 regulates cancer cell growth, migration, and invasion.

Expression of DZIP3 is increased in several cancer types

Oncomine database (a cancer microarray database, www.oncomine.org) analysis suggests that DZIP3 mRNA levels were significantly increased in several of the cancer types, including sarcoma, lung, gastric, breast, colon, liver, and pancreatic cancers (**Fig. 1H**; Supplementary Fig. S1E). Next, we analyzed DZIP3 mRNA expression in tumors in The Cancer Genome Atlas (TCGA) data set using the GEPIA2 platform (42). DZIP3 levels were found to be significantly higher in tumors as compared with normal control tissues in several cancer types (**Fig. 1I**).

The levels of DZIP3 expression in human breast carcinomas were investigated using two human tissue microarrays (168 patient cases and 22 adjacent normal controls). DZIP3 was found to be expressed in low levels (scores 0 or 1) in adjacent normal tissues (**Fig. 1J** and **K**), and most of the ducts and lobules were devoid of staining in all the cases (**Fig. 1J**). In breast invasive ductal carcinoma tissues, an intense (score 2; 88 cases) to very intense staining (score 3; 38 cases) of DZIP3 was observed (**Fig. 1J**). In some tissues, DZIP3 was exclusively present inside the nucleus, whereas, in most of the tissues, both cytoplasmic and nuclear staining was observed (**Fig. 1J**). About 126 breast cancer patient cases (metastatic and nonmetastatic) out of a total of 168 cases showed increased expression of DZIP3, much above adjacent control tissues (**Fig. 1K**). The ducts and lobules in these samples were strongly immunoreactive for DZIP3 (**Fig. 1K**). Altogether, the data suggest that the protein expression of DZIP3 is increased during tumorigenesis.

DZIP3 promotes tumor growth and metastasis in mice and zebrafish

To investigate whether DZIP3 can promote cancer cell growth *in vivo*, we subcutaneously injected an equal number of control and
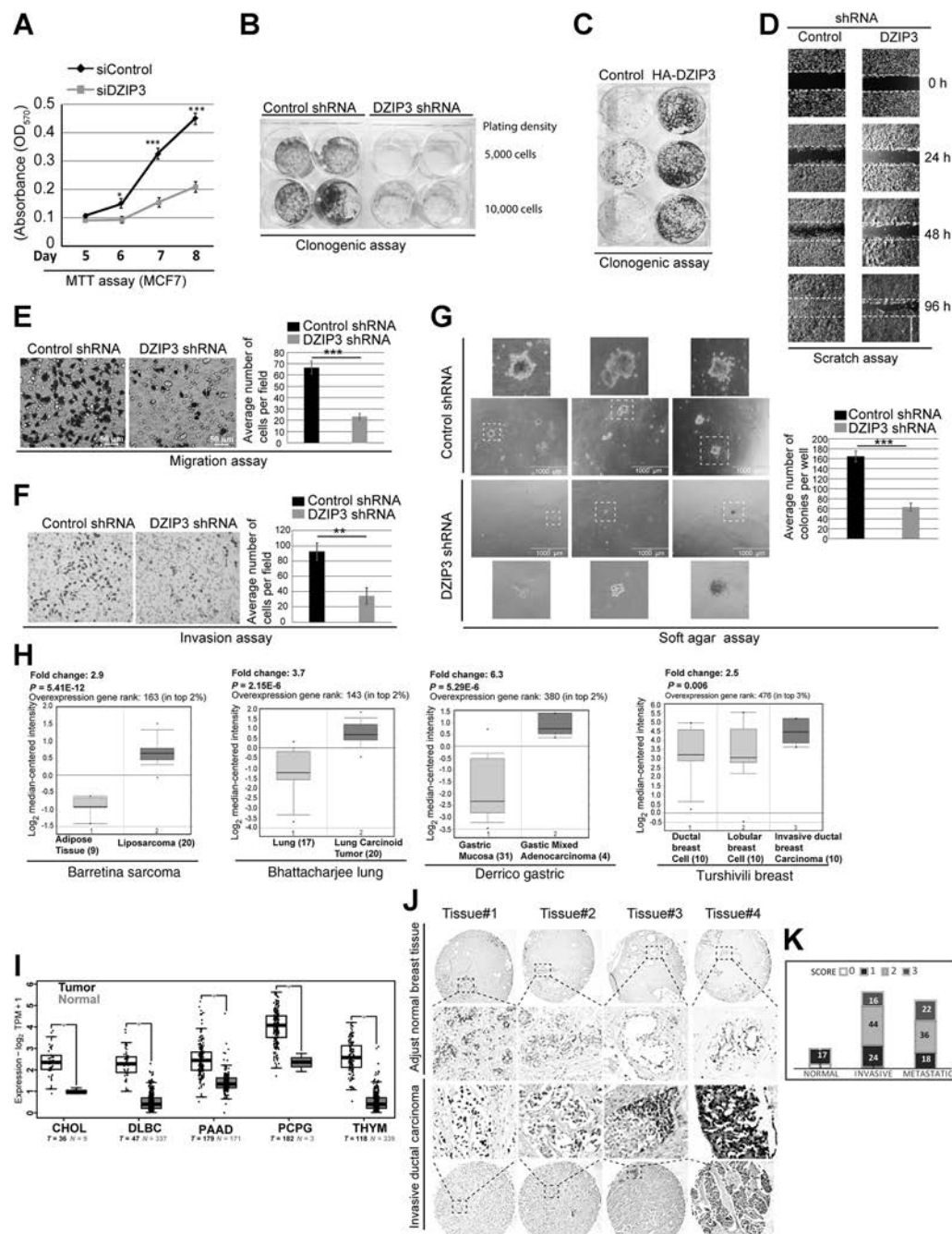
Figure 1.

DZIP3 drives growth, migration, and invasion of cancer cells. **A,** MTT assays were performed in MCF7 breast cancer cells transfected with control and DZIP3 siRNA. Data are presented as mean $\pm$ SD; n 3; , $P < 0.05$; , $P < 0.0005$. **B,** Clonogenic assay was performed with MCF7 control and DZIP3 stable knockdown cells with an initial plating density of 5,000 and 10,000 cells. **C,** Clonogenic assay was performed in HEK293 cells transiently transfected with control and HA-DZIP3. **D,** Wound healing or scratch assay was performed to examine migration capacity in control and DZIP3 stable knockdown MCF7 cells. **E** and **F,** Transwell migration and Matrigel invasion assay were performed in UM-UC3 control and DZIP3 stable knockdown cells. Data in bar graph are presented as mean $\pm$ SD; n 3; , $P < 0.005$; , $P < 0.0005$. **G,** Soft-agar colony formation assay was performed to check tumorigenicity of UM-UC3 control and DZIP3 stable knockdown cells. Data in bar graph presented are mean $\pm$ SD; n 3; , $P < 0.0005$. **H,** Oncomine analysis of DZIP3 mRNA expression levels in different cancer types (liposarcoma, lung carcinoma, gastric adenocarcinoma, and breast carcinoma) as compared with normal tissues. Fold change and P values are indicated in the graph. **I,** DZIP3 mRNA expression in tumors and normal control patient samples were evaluated in the TCGA data set using the GEPIA2 platform. TPM, transcripts per million, $Log_2FC|$ cutoff 1; P value cutoff 0.01. **J,** Representative images of tissue microarray analysis of DZIP3 protein expression in normal breast tissue (n 22) and invasive human breast cancer tissue (n 164) samples. **K,** The intensity of staining was scored using a four-tier scale and defined as follows: 0, 0%–20%; 1, weak staining (20%–50%); 2, moderate staining (50%–75%); and 3, strong staining (75%–100%). Based on these scores, the number of tissue samples in each group of tissue array (normal, invasive, and metastatic) having these scores were plotted.

Kolapalli et al.

DZIP3 knockdown UM-UC3 bladder cancer cells in BALB/C-nude mice. To nullify the variations due to innate immunity, we injected both control and knockdown cells in either flank of the same mice. Tumor growth was monitored daily for a period of 3 weeks and at the termination of the experiment. The growth rate of DZIP3 knockdown tumors was found to be considerably lower than the control tumors (**Fig. 2A**). In agreement, upon dissection, the volumes of DZIP3-depleted tumors were found to be significantly less than control tumors for all the mice (**Fig. 2B** and **C**).

The expression of nuclear Ki-67 is strongly associated with tumor cell proliferation, aggressiveness, and growth. IHC analysis revealed a significant decrease in nuclear Ki-67–positive cells in DZIP3 knockdown tumors as compared with the controls (**Fig. 2D** and **E**). During mitosis, Ki-67 forms perichromosomal layer and prevents chromosomes from collapsing into a single chromatin mass (43). Thus, the cells undergoing mitosis can be easily recognized using Ki-67 immunostaining as it gives a floral appearance (**Fig. 2F**; white arrows, **Fig. 2D**). We observed a significantly higher number of mitotic cells in control tumors as compared with DZIP3 knockdown tumors (**Fig. 2D–G**).

We used a tail-vein-injection metastasis model to validate the reduced migration and invasion phenotypes of DZIP3-depleted cells. MDA-MB-231 breast cancer cells (control and DZIP3 knockdown) were injected intravenously into the lateral tail vein of nude mice, and lung colonization was evaluated. Although the weight of mice in two groups did not change significantly, a considerably fewer number of tumor nodules were observed in the lungs of mice that were injected with DZIP3 knockdown cells (**Fig. 2H** and **I**). An increased number of metastatic foci were observed in the control group lung sections as compared with the DZIP3 knockdown group (**Fig. 2J**). The Western blot analysis from mouse lung lysates using human-specific antibody confirmed the reduced levels of DZIP3 (and Cyclin D1) in DZIP3 knockdown samples (Supplementary Fig. S2A). These observations suggest that the depletion of DZIP3 reduces the metastatic capacity of the cancer cells.

Next, we used Zebrafish (*Danio rerio*) [Tg(fli1:nEGFP)] tumor xenograft model (44) to further validate results. An equal number of the control and DZIP3-depleted MDA-MB-231 cells were stained with Dil (1,1′-dioctadecyl-3,3,3′,3′-tetramethylindocarbocyanine perchlorate) and injected into perivitelline space of 48-hour post fertilized zebrafish embryos. After 5 days of injection, primary tumors and metastatic dissemination of cancer cells were documented using a fluorescence microscope. Tumor growth, as measured by fluorescence intensity of primary tumors, was found to be significantly higher in the case of control cells compared with the DZIP3-depleted cells (**Fig. 2K** and **L**). The images were captured at the same microscopic settings (intensity, exposure, and thresholds) throughout the experiments. At 5 days after injection, cancer cells showed distal migration from the primary site in the case of control cells but not in the case of DZIP3 knockdown tumors (Supplementary Fig. S2B).

Taken together, the data from different *in vivo* models suggest that DZIP3 is an important driver of tumor growth and metastasis.

Depletion of DZIP3 results in cell-cycle arrest in the G_1–S phase

Next, we asked whether the reduced cell growth *in vitro* and *in vivo* in DZIP3-depleted cells is due to increased cell death. The Annexin-V/PI double staining of control and DZIP3 knockdown MCF7 cells showed no differences in the apoptotic population (Supplementary Fig. S3A). In an agreement, no difference in caspase-3 cleavage was observed in cultured cells and xenograft tumors (Supplementary

Fig. S3B and S3C), suggesting that increased apoptotic cell death is not the reason for the reduced proliferation of DZIP3-depleted cells.

The cell-cycle analysis was performed to test whether the defect in growth is due to reduced cell division. The DZIP3 knockdown in MCF7, UM-UC3, and HeLa cells resulted in the disconcerted cell cycle where a significant increase in the percentage of cells in G_1 phase and a significant decrease in the percentage of cells in S and G_2–M phase was observed in all the cell types tested (**Fig. 3A–C**; Supplementary Fig. S3D and S3E). Next, we synchronized the MCF7 cells using the serum starvation method (48 hours) and then released the cells in full media to track the progression of the cell cycle (Supplementary Fig. S3F). Control cells progressed to different cell-cycle phases normally. However, knockdown cells were arrested in the G_1 phase even after 12 hours of release. Taken together, the data suggest that DZIP3 is required for cell-cycle progression, and in its absence, cells are arrested in the G_1 phase of the cell cycle.

DZIP3 controls cell growth by regulating the expression of Cyclin D1

The Cyclin D1 drives the G_1 to S phase transition (45). Because we observed that DZIP3-depleted cells were arrested in the G_1 phase, we examined the levels of Cyclin D1 in different cell lines and xenograft tumors. In all of the cell lines tested (MCF7, UM-UC3, and MDA-MB-231), the expression of Cyclin D1 protein was considerably lower in DZIP3-depleted cells (**Fig. 3D**; Supplementary Fig. S3G–S3I). These data were validated using DZIP3 shRNA stable knockdown cells and transient siRNA knockdown cells using two different sets of siRNA and shRNA in three different cell lines (**Fig. 3D** and **E**; Supplementary Fig. S3G–S3I). Further, DZIP3 was knocked out using the CRISPR-Cas9 technique in two different cell lines. There was a considerable reduction in levels of Cyclin D1 in the DZIP3 knockout clones (**Fig. 3F** and **G**).

The levels of Cyclin D1 in DZIP3 knockdown tumors were lower than control tumors (**Fig. 3H**). Next, to understand whether Cyclin D1 regulation by DZIP3 is direct or is a consequence of growth defect (cause or consequence), we transiently overexpressed DZIP3 in HEK293 cells for a very short duration (6 hours). No growth difference and cell-cycle defect were observed in these cells, but the overexpression of DZIP3 was able to strongly stabilize the endogenous Cyclin D1 (**Fig. 3I**). Taken together, the results suggest that DZIP3 positively regulates the expression of Cyclin D1. To further strengthen this conclusion, we complemented DZIP3 knockdown cells with exogenous DZIP3 (transient expression) and assessed its ability to restore Cyclin D1 protein levels (**Fig. 3J**). The Cyclin D1 protein levels were restored completely in DZIP3-complemented cells.

Extensive literature suggests that depletion of Cyclin D1 results in reduced growth, migration, and invasion in several cancer types. We also validated these results using scratch assays, migration assays, and invasion assays (Supplementary Fig. S3J–S3L). To understand whether the growth, migration, and invasion defect observed in DZIP3 depleted cells are due to lower Cyclin D1 expression in these cells, we complemented DZIP3 knockdown cells with Cyclin D1 and performed the assays. The Cyclin D1 complementation significantly rescued the growth defect of DZIP3 knockdown cells in clonogenic assays and MTT assays (**Fig. 3K** and **L**). Also, Cyclin D1 complementation rescued the defective migration and invasion phenotype of DZIP3 knockdown cells (**Fig. 3M** and **N**). Taken together, the data suggest that DZIP3 controls the growth and invasion properties of cancer cells by regulating the expression of Cyclin D1.
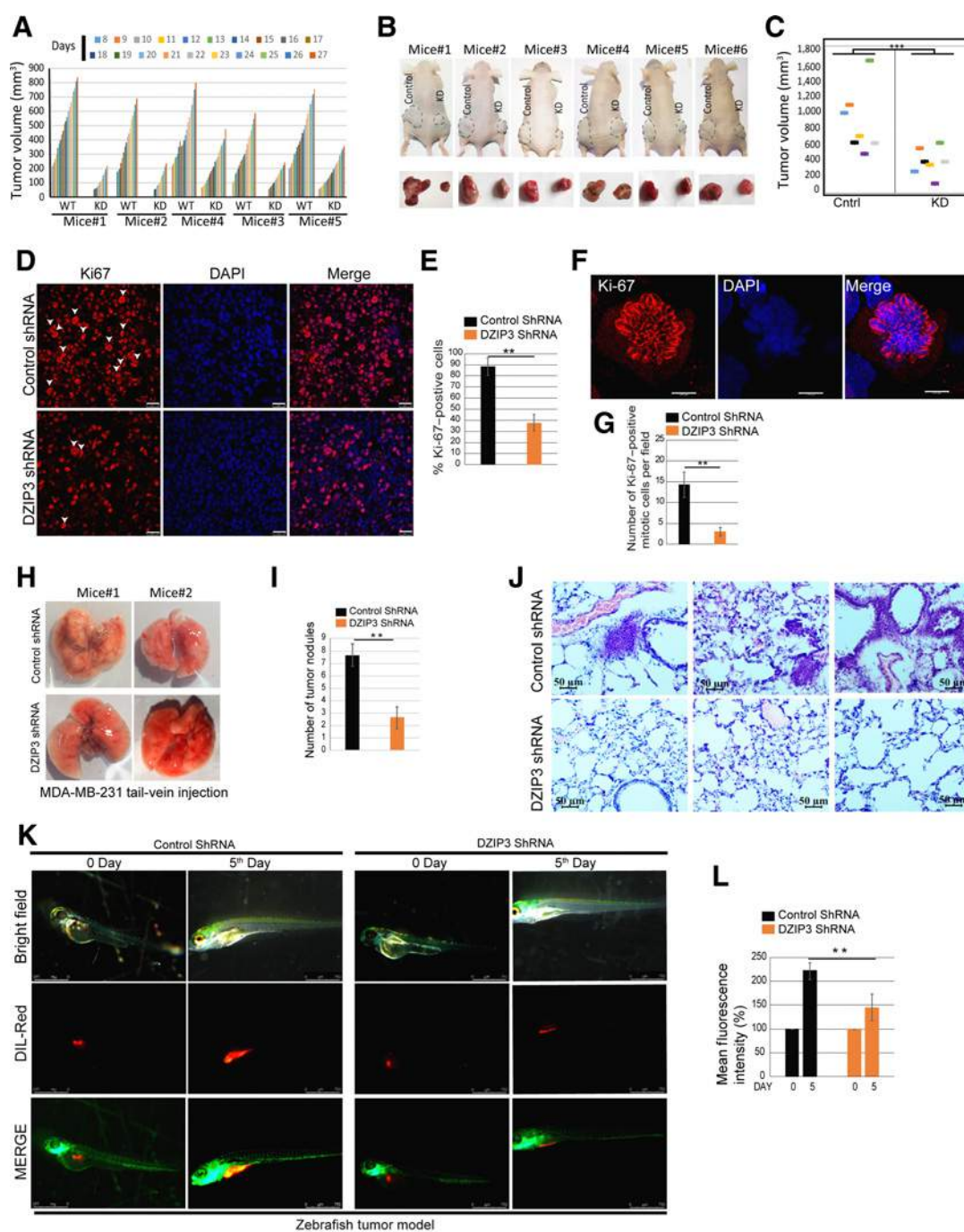
Figure 2.

DZIP3 promotes tumor growth and metastasis in animal models. **A,** The graph depicts tumor volumes (mm^3) of UM-UC3 control and DZIP3 stable knockdown cells. **B,** Images of tumors formed in the nude mice and pictures of the dissected tumors. **C,** The graph represents the final tumor volume. $n = 7$; mean $\pm$ SE; $, P < 0.0005$. **D,** IHC analysis was performed with the Ki-67 cell proliferation marker in control and DZIP3 stable knockdown tumor sections. White arrowhead, Ki-67–positive mitotic cells. **E,** The graph represents percentage of cells with Ki-67–positive staining. >400 cells were analyzed from different sections from different animals; mean $\pm$ SD; $, P < 0.005$. **F,** Representative images of Ki-67–positive mitotic cells. **G,** The graph represents percentage of Ki-67–positive mitotic cells in control and DZIP3 stable knockdown tumors in IHCs microscopic fields. >10 microscopic fields were analyzed from different sections from three different animals; mean $\pm$ SD; $, P < 0.005$. **H,** Representative images of lungs of mice injected (tail vein) with MDA-MB-231 control and DZIP3 stable knockdown cell line. **I,** The average number of nodules were counted manually. $n = 3$; mean $\pm$ SD; $, P < 0.005$. **J,** Representative lung sections showing metastatic foci in control groups. **K,** Lateral view of fluorescent transgenic [Tg(fli1:nEGFP)] zebrafish embryos at days 0 and 5 injected with Dil-Red–stained MDA-MB-231 control and DZIP3 stable knockdown cells. **L,** The tumor growth was assessed by an increase in fluorescence intensity on the fifth day compared with the day of injection. $n = 10$; mean $\pm$ SD; $, P < 0.005$. The quantitation of fluorescence intensity was performed using ImageJ software and is represented as % mean fluorescence intensity, where day 0 reading was taken as baseline.

Kolapalli et al.
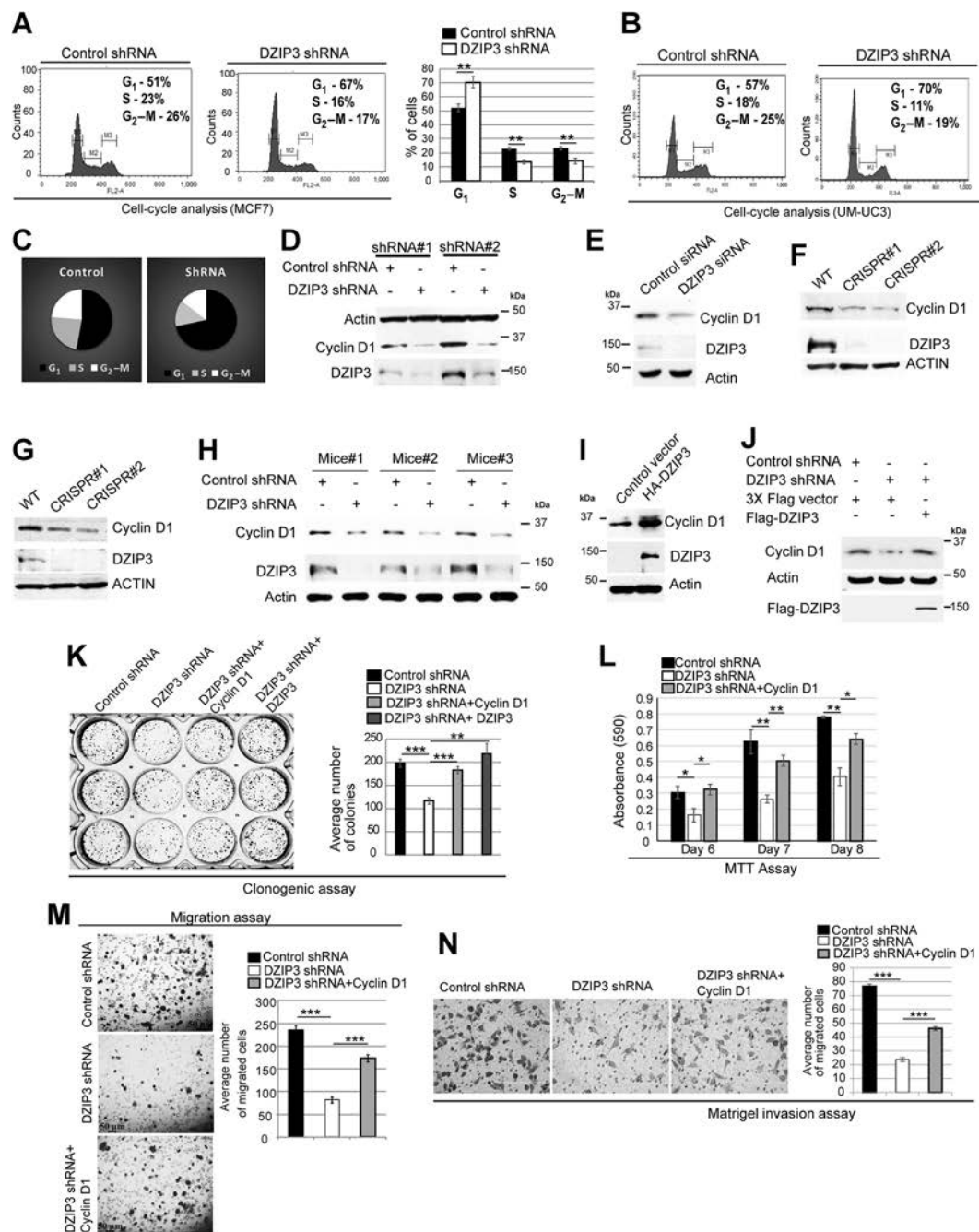
Figure 3.
DZIP3 controls cell-cycle progression and cell growth by regulating the expression of Cyclin D1. **A,** Cell-cycle analysis of MCF7 control and DZIP3 stable knockdown cell line. The graph represents the percentage of cells in different cell-cycle phases. Mean ± SD; n   3; , P < 0.005. **B,** Cell-cycle analysis of UM-UC3 control and DZIP3 stable knockdown cells. **C,** Pie charts represent the percentage of cells in different cell-cycle phases. **D** and **E,** Western blot analysis of MCF7 control and DZIP3 shRNA cell lysates probed with indicated antibodies (**D**). **E,** Control and DZIP3 siRNA-transfected MCF7 cell lysates probed with indicated antibodies. **F** and **G,** Western blot analysis of HEK293T (**F**), MCF7 (**G**), control, and DZIP3 CRISPR knockout clone cell lysates probed with indicated antibodies. **H,** Western blot analysis of UM-UC3 control and DZIP3 shRNA tumor lysates probed with indicated antibodies. **I,** Western blot analysis of control and HA-DZIP3 plasmid–transfected HEK293 cell lysates probed with indicated antibodies. **J,** Western blot analysis of cell lysates of indicated plasmid–transfected MCF7 control and DZIP3 shRNA cells probed with indicated antibodies. **K,** Clonogenic assay was performed with control, DZIP3 stable knockdown cells, and knockdown cells complemented with HA-Cyclin D1 or Flag-DZIP3. The graph depicts the average number of colonies in these conditions. Mean ± SE; n   3; , P < 0.005;   , P < 0.0005. **L,** Cell proliferation was evaluated by performing MTT assay in MCF7 control, DZIP3 stable knockdown, and Cyclin D1–complemented DZIP3 knockdown cells. Data are presented as mean ± SD; n   2; , P < 0.05;   , P < 0.005. **M,** Migration assay was performed with MCF7 control, DZIP3 stable knockdown, and Cyclin D1–complemented DZIP3 knockdown cells. Data are presented as mean ± SE; n   3;   , P < 0.0005. **N,** Matrigel invasion assay was performed with UM-UC3 control, DZIP3 stable knockdown, and Cyclin D1–complemented DZIP3 knockdown cells. Data, mean ± SE; n   3;   , P < 0.0005.

DZIP3 interacts at 3′UTR of Cyclin D1 mRNA and stabilizes it

The aberrant overexpression of Cyclin D1 is strongly associated with the pathogenesis and progression of several cancer types (46). So, we analyzed whether the mRNA expression of DZIP3 and Cyclin D1 is correlated in human cancer patients database using the Gene Expression profiling Interactive analysis (GEPIA) platform (http://gepia.cancer-pku.cn/; ref. 47). We found a strong positive correlation of mRNA expression between *DZIP3* and *Cyclin D1* in different cancer types, including thymus, breast, kidney, rectum, and prostate (**Fig. 4A**; Supplementary Fig. S4A), indicating a possible regulation of *Cyclin D1* by DZIP3 in cancer patients. However, no significant correlation was found between *DZIP3* and *Cyclin B1* mRNA expression (Supplementary Fig. S4B).

We then investigated the mechanism by which DZIP3 positively controls the expression of Cyclin D1. DZIP3 contains an RNA-binding motif called lysine (K)-rich region (or KR motif), a RING domain, and several coiled–coiled domains (CCD; Supplementary Fig. S4C and S4D; ref. 13). Previous studies showed that DZIP3 could interact with RNA utilizing the KR motif (13, 14). RBPs such as HuR (Human antigen R) and AUF1 (AU-rich element RNA-binding protein 1) were shown to regulate the stability of the cyclins mRNA by interacting with AU-rich element (ARE sites) in 3′ untranslated regions (3′ UTR; refs. 25, 26, 48). We hypothesized that DZIP3 being RNA-binding protein regulates expression of Cyclin D1 by interacting with its mRNA at 3′ UTR and subsequently stabilizing the Cyclin D1 transcripts. To test this hypothesis, first, we performed RNA pull-down assays with either the DZIP3 antibody or control IgG antibody, followed by a real-time qPCR (**Fig. 4B**) or reverse transcriptase-PCR (**Fig. 4C**) with *Cyclin D1* and GAPDH primers (Supplementary Fig. S4E). Significant enrichment of *Cyclin D1* mRNA was observed in RNA pull-down by the DZIP3 antibody compared with IgG control (**Fig. 4B** and **C**). No enrichment was observed with GAPDH mRNA (Supplementary Fig. S4E). Similar results were obtained with Flag-DZIP3 overexpressing cells (**Fig. 4D**; Supplementary Fig. S4F). The data suggest that DZIP3 specifically interacts with *Cyclin D1* mRNA.

Next, we performed *in vitro* biotin RNA pull-down assays with 5′ and 3′ UTR's RNA fragments of *cyclin d1* mRNA (**Fig. 4E**). The *in vitro*–transcribed RNA fragments were biotinylated and incubated with lysates expressing Flag-DZIP3 or just Flag epitope subjected to pull-down by streptavidin beads. The Western blot with DZIP3 showed that DZIP3 interacted specifically and strongly with *cyclin D1* 3′ UTR but very faintly with 5′ UTR, and no interaction was observed in bead controls (**Fig. 4F**). Within 3′ UTR of *cyclin D1*, DZIP3 was bound with 3D (∼2,286 bp to ∼2,730 bp) and 3E regions (∼2,681 bp to ∼3,130 bp; **Fig. 4E–G**). Thus, DZIP3 specifically interacts with 3′ UTR of *cyclin D1* mRNA.

Next, we attempted to identify the binding sites of DZIP3 in Cyclin D1 3′UTR (**Fig. 4E**). Most of the RBPs control the stability of mRNA via interaction with the ARE with the core-binding element "AUUUA" (ATTTA in DNA; ref. 49). Using ARE prediction software (AREsit2; http://rna.tbi.univie.ac.at/AREsite2/welcome), we found four ATTTA elements in 3D region and one such site in the 3E region of *cyclin D1* 3′UTR (**Fig. 4E**). We mutated these sites in the 3D region (ATTTA AGGGA; **Fig. 4H** and **I**) and compared them with wild-type mRNA for the capability to interact with DZIP3. In biotinylated RNA pull-down assays, ARE site mutations dramatically reduced the affinity of the 3D region for DZIP3 (**Fig. 4J** and **K**), indicating that AUUUA is binding sites of DZIP3 in 3′ UTR of cyclin D1.

In unsynchronized cells and in steady-state conditions, the effect of DZIP3 on total *Cyclin D1* mRNA levels was marginal. A slight induction of *Cyclin D1* mRNA levels was observed in DZIP3-overexpressing cells (Supplementary Fig. S4G). Similarly, DZIP3 knockdown cells or tumors showed a minor reduction in the *Cyclin D1* mRNA amount compared with the control cells (Supplementary Fig. S4H and S4I). However, unsynchronized cells are in different phases of the cell cycle, which is not an ideal condition to determine the effect of RBPs on the stability of cyclins mRNA's (26). To delineate the role of DZIP3 in mRNA stability, we synchronized the cells into the G_1 phase by serum starvation and performed the actinomycin D pulse-chase assays to examine the rate of degradation of *Cyclin D1* mRNA in the absence and presence of DZIP3. The data showed that the rate of degradation of *Cyclin D1* mRNA was significantly less in DZIP3-overexpressing cells compared with the control cells (**Fig. 4L**). On the other hand, the rate of degradation of cyclin D1 mRNAs was higher in DZIP3 stable knockdown cells compared with control cells (**Fig. 4M**). Altogether, these results suggest that DZIP3 interacts and stabilizes *cyclin D1* mRNA.

The RNA-binding KR motif of DZIP3 is important for its interaction with RNA (13). To validate the specificity of DZIP3–cyclin D1 mRNA interaction and to confirm that the KR motif is important for this interaction, we deleted the KR motif in DZIP3 (**Fig. 4N**) and compared this protein with the wild-type DZIP3 for its ability to bind and stabilize the *cyclin D1* mRNA. In biotin RNA-pull-down assay, the KR motif–deleted DZIP3 (DZIP3-ΔKR) was defective in its ability to interact with 3′UTR of *cyclin D1* mRNA (**Fig. 4O**) and also failed to stabilize the *cyclin D1* transcripts in actinomycin D chase assays (**Fig. 4P**). These results are significant as the deletion of a small region (∼90 bp) containing the KR motif in the DZIP3 protein (3,624 bp gene) crippled its RNA-binding and RNA stabilizing potential. The data suggest that the KR motif of DZIP3 plays an important role in DZIP3–cyclin D1 mRNA interaction and stability.

DZIP3 interacts, colocalizes, and stabilizes Cyclin D1 in G_1 phase

DZIP3 localizes in both the nucleus and cytoplasm in four different cell lines we tested (**Fig. 5A**; Supplementary Fig. S5A–S5C). In the cytoplasm, DZIP3 was found in perinuclear regions as well as in punctuated structures (**Fig. 5A**; Supplementary Fig. S5A–S5C). DZIP3 is a bona fide E3-ubiquitin ligase, and several of the E3 ligases are known to modulate the stability of cell-cycle proteins (36, 50–52). Next, we tested whether DZIP3, in addition to controlling the stability of *cyclin D1* mRNA, can modulate Cyclin D1 protein levels. We synchronized the cells by serum starvation and then performed cycloheximide chase experiments both in DZIP3-overexpressing HEK293 cells (**Fig. 5B**) and DZIP3-depleted MCF7 cells (**Fig. 5C**) and monitored the stability of the endogenous Cyclin D1 proteins over a period of time. In the DZIP3-overexpressing cells, Cyclin D1 was well stabilized till 8 hours. On the other hand, in control vector–transfected cells, Cyclin D1 was degraded rapidly within 2 hours and almost entirely degraded by 6 hours (**Fig. 5B**). In DZIP3-stable knockdown cells, the degradation of the Cyclin D1 proteins was faster as compared with the control cells (**Fig. 5C**). The data suggest that DZIP3 provides stability to the Cyclin D1 at the protein levels also.

To understand how DZIP3 imparts stability to Cyclin D1 at protein levels, we first tested whether DZIP3 interacts with Cyclin D1. We performed IP assays with endogenous as well as overexpressed proteins. In endogenous IP assays, we used IgG and Cyclin D1 antibodies for IP, and the immunoblotting was performed with the DZIP3 antibody (**Fig. 5D**). The Cyclin D1 but not IgG antibody was able to pull down DZIP3, suggesting a specific interaction between DZIP3 and Cyclin D1 (**Fig. 5D**). Next, we overexpressed HA-Cyclin D1 and Flag-DZIP3 and performed coimmunoprecipitation (co-IP) assay with HA antibody. A strong interaction between DZIP3 and Cyclin
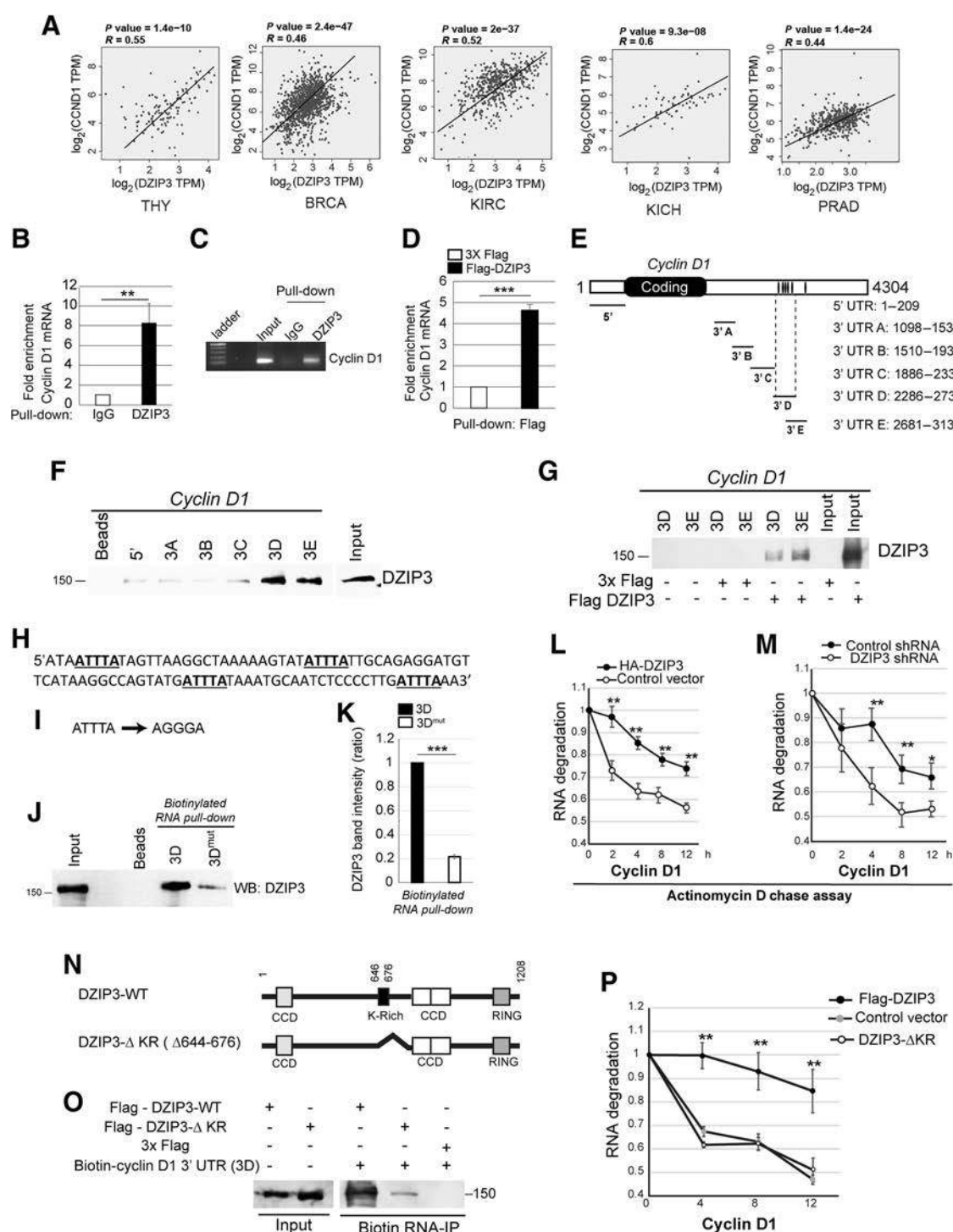
Kolapalli et al.

Figure 4.

DZIP3 interacts with Cyclin D1 mRNA and stabilizes it. **A,** The graphs depict the correlation of mRNA expression of *DZIP3* and *Cyclin D1* in different cancer types. *r*, Spearman rank correlation coefficient. TPM, transcripts per million; THY, thymoma; BRCA, breast invasive carcinoma; KIRC, kidney renal clear cell carcinoma; KICH, kidney chromophobe; PRAD, prostate adenocarcinoma. **B** and **C,** qRT-PCR analysis of enrichment of *Cyclin D1* mRNA in RNA IP assay using IgG and DZIP3 antibody. The fold enrichment was calculated by taking IgG values as a baseline. Data are presented as mean ± SD; n　3;　, $P < 0.005$. **C,** Agarose gel analysis of Cyclin D1 RT-PCR product from the same experiment. **D,** qRT-PCR analysis of enrichment of *Cyclin D1* mRNA in RNA IP assay using Flag antibody. The fold enrichment was calculated by taking control values as a baseline. Data are presented as mean ± SD; n　3;　, $P < 0.0005$. **E,** Schematic representation of different RNA fragments of *Cyclin D1* mRNA 3′-UTRs and 5′-UTR used in RNA pull-down assays. The black bars in 3′UTR represent the AU-rich elements. **F,** The biotinylated 5′UTR region and 3′UTR's of *Cyclin D1* transcripts were incubated with lysates of HEK293T cells, followed by pull-down with streptavidin-tagged beads.　(*Continued on the following page.*)

D1 was observed (**Fig. 5E**). Next, using Flag antibody-tagged beads, we performed pull-down assays with cells overexpressing Flag-DZIP3. We used stringent conditions (6 times NP-40 buffer) for washing the beads to remove weak interactions with DZIP3. The Flag-DZIP3 was eluted from beads using Flag-peptide, and Western blotting was performed with the Cyclin D1 antibody. We observed a single band of endogenous Cyclin D1 suggestive of a strong interaction between DZIP3 and endogenous Cyclin D1 (Supplementary Fig. S5D).

PLA is a powerful quantitative technique that allows *in situ* detection of protein–protein interactions with high specificity and sensitivity (53). Because the PLA-positive signals (puncta's) are detected only when the two proteins are at close proximities of < 40 nm, such protein interactions are most likely to be the direct interactions (53). In PLA assays, we found a robust increase in the number of PLA-positive punctas in the cells expressing DZIP3 and Cyclin D1, suggestive of direct interactions between DZIP3 and Cyclin D1 (**Fig. 5F** and **G**). To further strengthen the direct interaction data, we tested whether purified GST-DZIP3 (CCD-RING domain) directly interact with Cyclin D1 *in vitro*. For this, we performed GST pull-down assays with purified GST-DZIP3 (CCD-RING domain) and *in vitro*–translated Cyclin D1 in the cell-free milieu. A direct and specific interaction was observed between DZIP3 and Cyclin D1 (**Fig. 5H**). Taken together, several lines of evidence suggest that DZIP3 directly interacts with Cyclin D1.

Next, we asked whether DZIP3 interacts with Cyclin D1 constitutively or in a cell-cycle phase-dependent manner. For this, we overexpressed DZIP3 and Cyclin D1 proteins and then synchronized the cells in the G_1 phase, S phase, and G_2 phase by using serum starvation, single thymidine block, and nocodazole block, respectively. Serum starvation blocks the cell cycle at the G_1 phase, whereas thymidine in the early S phase and nocodazole at the border of the G_2 and M phase. The synchronized cells were used in co-IP assays. DZIP3 interacts with Cyclin D1 preferentially during the G_1 phase of the cell cycle, suggesting that DZIP3 interacts and stabilizes Cyclin D1 typically during the G_1 phase (**Fig. 5I**). We also performed the PLA assay in serum-synchronized G_1-arrested cells. We observed a significant increase in the number of punctas in synchronized cells than in unsynchronized cells, strengthening our conclusions that DZIP3 interacts with and regulates Cyclin D1 predominantly in the G_1 phase of the cell cycle (**Fig. 5F** and **G**). This is an interesting finding that DZIP3 interacts with Cyclin D1 only when the latter is required to be stabilized for the cell-cycle progression.

Because Cyclin D1 is localized in the nucleus during the G_1 phase (54), next, we performed immunofluorescence assays with the G_1 phase (serum starvation)–synchronized cells to monitor the localization of DZIP3 and Cyclin D1. DZIP3 was found to be completely

colocalized with nuclear Cyclin D1 in G_1 phase–synchronized cells (**Fig. 5J**). Interestingly, in IHC of xenograft tumor tissues, Cyclin D1 showed increased immunoreactivity in the nucleus of the control tumor cells. Whereas considerably less Cyclin D1 nuclear immunostaining was observed in DZIP3-depleted tumors cells (**Fig. 5K**). The data indicate that DZIP3 is required not only for the stability of Cyclin D1 but might also for its nuclear localization.

CCD and RING domains of DZIP3 are important for its interaction with Cyclin D1

DZIP3 contains three CCDs, a RING domain, and an RNA-binding KR motif (**Fig. 5L**). To identify the domain/s of DZIP3 required for interaction with Cyclin D1, we generated several DZIP3 domain deletion variants (**Fig. 5L**). The deletion constructs were coexpressed with HA-Cyclin D1, and co-IP assays were performed. To reduce the effect of DZIP3-mediated stability on Cyclin D1–DZIP3 interaction, in this experiment, we have adjusted the ratio of Cyclin D1 to equalize it in the input, and then the IP was run in the same ratio. There was no apparent change in binding affinity of DZIP3–Cyclin D1 upon KR domain deletion (**Fig. 5M**). RING domain deletion reduced the interaction, and it was further reduced on the deletion of the CCD2/3 domain (**Fig. 5M**), suggesting that both domains are important of DZIP3–Cyclin D1 interactions. However, where the RING domain itself cannot interact with Cyclin D1, an interaction was observed between the CCD2/3 domain and Cyclin D1 (**Fig. 5M**), suggesting that the CCD2/3 domain provides a primary interface for the interaction, and the RING domain assists in increasing the interactions.

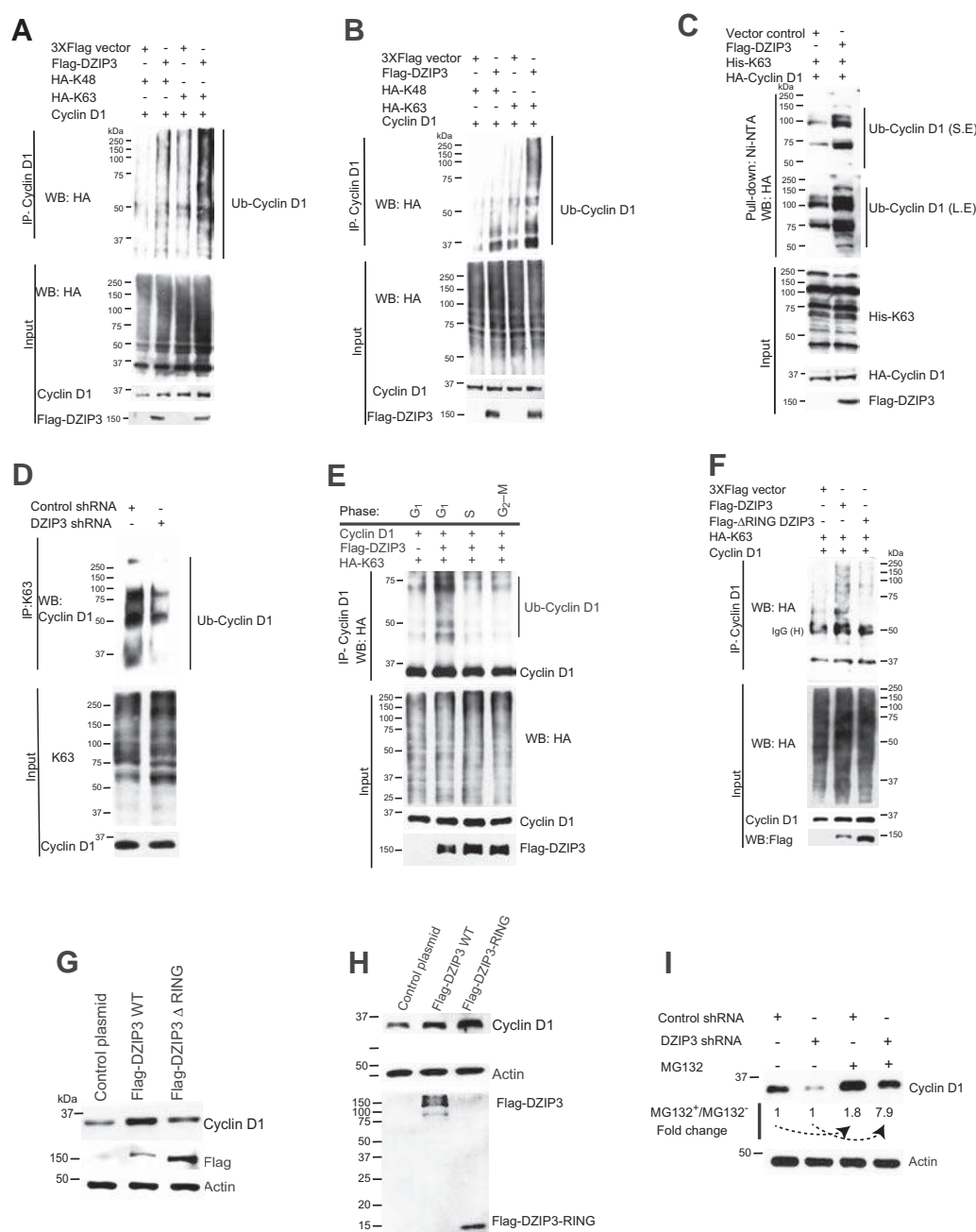### DZIP3 enhances K63-linked ubiquitination of Cyclin D1

DZIP3 is a RING domain–containing E3 ubiquitin ligase (13, 14). Next, we examined whether DZIP3 can modulate the ubiquitination status of Cyclin D1. K48-linked ubiquitination of proteins is associated with proteasomal degradation, whereas K63-linked ubiquitination plays a proteasomal degradation-independent role and is shown to be important in signaling, trafficking, sorting, and stabilization of the proteins (36, 55–58). DZIP3 and Cyclin D1 were coexpressed in HEK293 cells along with the two ubiquitin variants, HA-K48 and HA-K63. In HA-K48 ubiquitin, all lysine residues were mutated except at amino acid position 48 (K48). In HA-K63, all lysine residues were mutated except at amino acid position 63 (K63). The co-IP assays were performed to understand whether DZIP3 ubiquitinates Cyclin D1. DZIP3 considerably increased the K63-linked ubiquitination of Cyclin D1 with minimally effecting K48-linked ubiquitination (**Fig. 6A**). Next, to reduce the effect of DZIP3-mediated stability on Cyclin D1–DZIP3 interaction, we repeated the experiment, where we have

---

(*Continued.*) The pull-down complexes were subjected to Western blotting with Flag antibody. Bead control does not contain RNA. **G,** The biotinylated 3′UTR's of *Cyclin D1* transcripts were incubated with lysates of 3X Flag vector or Flag-DZIP3 expressing HEK293T cells, followed by pull-down with streptavidin-tagged beads. The pull-down complexes were subjected to Western blotting with Flag antibody. **H,** The nucleotide sequence of the 3D region of 3′UTR of *Cyclin D1* mRNA containing four ATTTA sites. **I,** The mutation of ATTTA to AGGGA was introduced in all the four sites in the indicated 3D region. **J,** The biotinylated 3′-UTR of *Cyclin D1*-D fragment (3D) wild-type and its mutant were incubated with Flag-DZIP3–expressing HEK293T cell lysates, followed by pull-down with streptavidin-tagged beads. The pull-down complexes were subjected to Western blotting with Flag antibody. **K,** Graph depicts the ratio of binding affinity of 3D and 3D-mut regions for Flag-DZIP3 as measured by ImageJ analysis of Western blots of biotin pull-down assays (**J**). Data are presented as mean ± SD; n 3; , $P < 0.0005$. **L** and **M,** Control HA-vector and HA-DZIP3 transiently transfected HEK293T cells (**L**) and control and DZIP3 shRNA stable knockdown MCF7 cells (**M**) were serum starved for 16 hours and released into a full medium for 3 hours and treated with actinomycin D (5 μg/mL) for indicated time points. The total RNA was isolated and subjected to qRT-PCR with *Cyclin D1*–specific primers. Data were normalized with GAPDH (transcript level of GAPDH was not affected by actinomycin D). Data, mean ± SD; n 3; $P < 0.05$; , $P < 0.005$. **N,** Schematic representation of wild-type (WT) and lysine-rich (KR) deletion mutant of DZIP3. **O,** Biotinylated 5′ and 3′D UTRs of *Cyclin D1* were used for RNA pull-down experiments with lysates of HEK293T cells transiently transfected with vector control, WT Flag-DZIP3, and Flag-DZIP3-ΔKR and subjected to Western blot analysis with Flag antibody. **P,** Actinomycin D chase assay and qRT-PCR assays were performed with HEK293T cells transiently transfected with control, Flag-DZIP3, and Flag DZIP3-ΔKR. Data, mean ± SD; n 3; , $P < 0.005$.

Kolapalli et al.
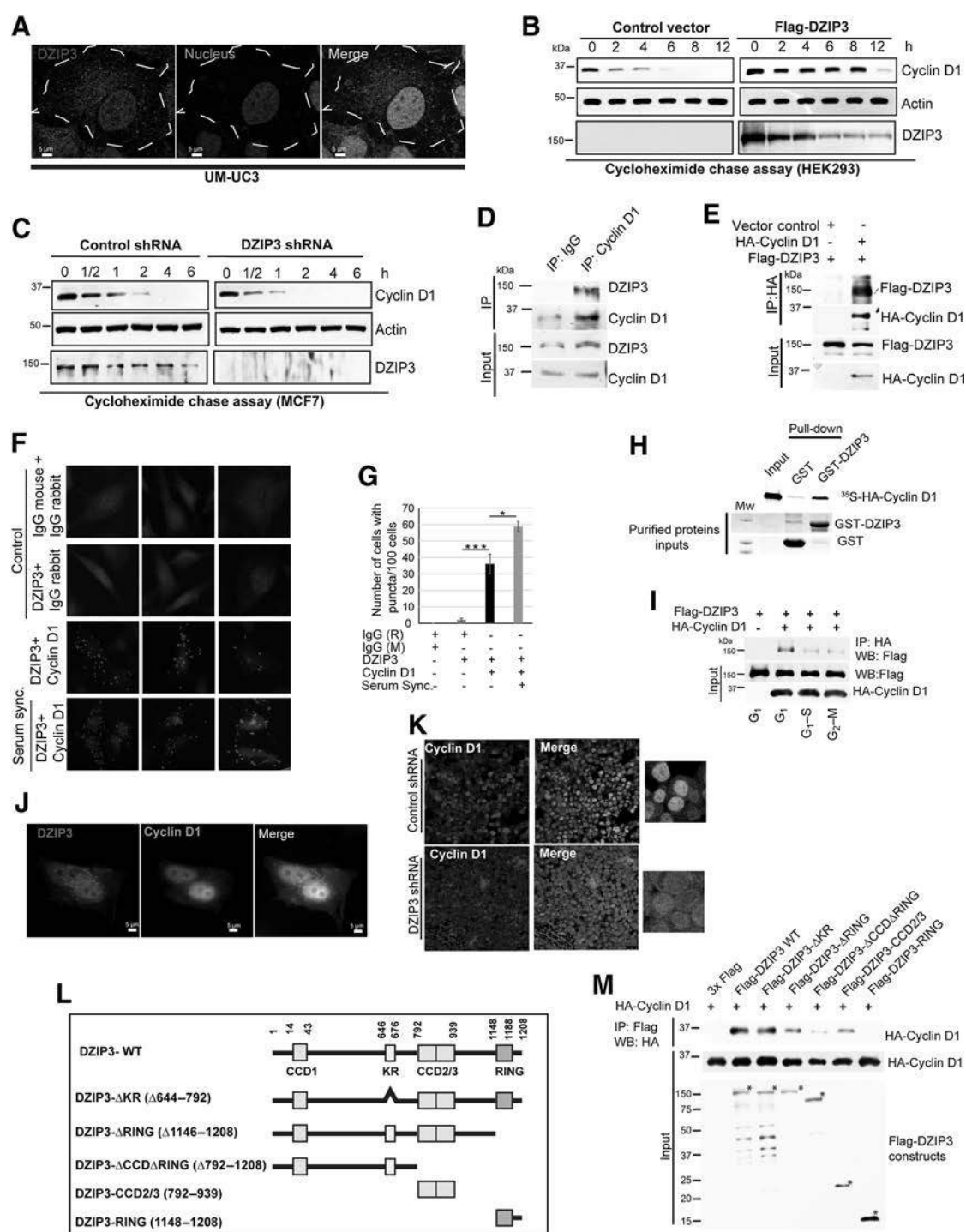
Figure 5.
DZIP3 interacts, colocalizes, and stabilizes Cyclin D1. **A,** Representative confocal images of DZIP3 localization in UM-UC3. **B** and **C,** Western blot analysis of cycloheximide chase experiment performed with HEK293T transiently transfected with indicated plasmids (**B**) and shControl and shDZIP3 MCF7 cells (**C**). **D** and **E,** IP analysis of the interaction between endogenous DZIP3 and endogenous Cyclin D1 (**D**) and Flag-DZIP3 and HA-Cyclin D1 (**E**). **F**, Representative images of PLA performed with unsynchronized and serum synchronized HeLa cells that were transfected with indicated plasmids. **G,** The graph represents the number of punctas present per 100 cells. Data, mean ± SD; n 3; , $P < 0.05$; , $P < 0.0005$. **H,** GST pull-down assay using purified GST or GST-tagged DZIP3 (CCD-RING domain. and *in vitro*–translated and S^{35}-labeled HA-Cyclin D1. **I,** The Western blot analysis of co-IP assays performed with HEK293 cells transiently cotransfected with Flag-DZIP3, HA-Cyclin D1, and synchronized in G_1 (serum starvation), G_1/S (single thymidine block), or G_2–M (nocodazole block) phases. **J,** Representative confocal images of DZIP3 and Cyclin D1 protein localization in serum synchronized MCF7 cells. **K,** Representative confocal images of immunofluorescence analysis of Cyclin D1 expression in tumor xenograft sections. **L,** The domain organization map of DZIP3 and its truncated mutants cloned as Flag-tagged proteins. **M,** Co-IP analysis to map the domain interaction between Flag-DZIP3 constructs and HA-Cyclin D1.

Figure 6.
DZIP3 increases the K63-linked ubiquitination of Cyclin D1 to stabilize it. **A** and **B,** Western blot analysis of co-IP experiments performed with lysates of HEK293T cells transiently transfected with Flag-DZIP3, Cyclin D1, HA-K48-Ubiquitin, and HA-K63-Ubiquitin plasmids [variants of ubiquitin that can only be ubiquitinated at either lysine 48 (K48) or lysine 63 (K63)]. **C,** Western blot analysis of Cyclin D1 ubiquitination in the absence and presence of DZIP3 by Ni-NTA pull-down assays using transiently transfected plasmid constructs as indicated. His-tagged ubiquitin (His-K63 was mutated at all lysines except at 63 position) was used in these assays. SE, short exposure; LE, long exposure. **D,** Western blot analysis of endogenous Cyclin D1 ubiquitination in MCF7 Control and DZIP3 knockdown cells (IP was run in a ratio of adjusted equalized inputs to reduce the artifact of DZIP3 mediated stability). **E,** Western blot analysis of co-IP experiments performed with HEK293T cells transiently transfected with Flag-DZIP3, Cyclin D1, HA-K48-Ubiquitin, and HA-K63-Ubiquitin plasmids, and synchronized in G_1 (serum starvation), G_1–S (single thymidine block), or G_2–M (Nocodazole block) phases (IP was run in a ratio of adjusted equalized inputs to reduce the artifact of DZIP3 mediated stability). **F,** Western blot analysis of co-IP experiments performed with HEK293T cells transiently transfected with Flag-DZIP3, FLAG ΔRING DZIP3, Cyclin D1, and HA-K63-Ubiquitin plasmids (IP was run in a ratio of adjusted equalized inputs to reduce the artifact of DZIP3 mediated stability). **G,** Western blot analysis of Cyclin D1 in HEK293T cells overexpressing Flag-DZIP3 and FLAG ΔRING DZIP3. **H,** Western blot analysis of Cyclin D1 in HEK293T cells overexpressing Flag-DZIP3 and FLAG-DZIP3-RING. **I,** Western blot analysis of MG132-untreated or treated, shcontrol, and shDZIP3 MCF7 cells lysates probed with indicated antibodies. The ImageJ quantification of Western band intensity was performed and fold change was depicted, where MG132-untreated samples were used as baseline.

adjusted the ratio of Cyclin D1 to equalize it in the inputs and then the IP sample are run in the same ratio. Here also, we observed considerably increased K63-linked ubiquitination of Cyclin D1 in the presence of DZIP3 (**Fig. 6B**).

Because in the above experiments, we have performed IP with Cyclin D1 and Western blot with HA (ubiquitin), it could be argued that DZIP3 is not directly ubiquitinating Cyclin D1 but possibly one of the Cyclin D1-interacting protein. To eliminate this possibility and also to determine whether DZIP3 directly induce the ubiquitination of Cyclin D1, we performed a classic experiment. The His-K63-Ub (Ubiquitin mutated for all lysines except 63 positions) was coexpressed with Cyclin D1 in the absence and presence of DZIP3. His-K63-Ub was pulled down with Ni-NTA agarose beads and probed with the Cyclin D1 antibody. Because the Ni-NTA affinity pull-down assays were performed in highly denaturing conditions (6M guanidine-HCl), a state in which no protein–protein interaction can exist, any increase in ubiquitination of Cyclin D1 depict direct conjugation of ubiquitin. We found a considerable increase in the direct conjugation of K63-linked ubiquitin of Cyclin D1 (high molecular weight) in the presence of DZIP3 (**Fig. 6C**), showing that indeed DZIP3 enhances K63-linked ubiquitination of Cyclin D1.

To determine whether DZIP3 controls K63-linked ubiquitination of endogenous Cyclin D1, next, we performed IP with K63-linkage specific polyubiquitin antibody from the lysates of control and DZIP3 knockdown cells. The results demonstrate that upon DZIP3 depletion, K63-linked ubiquitination of endogenous Cyclin D1 is considerably reduced (**Fig. 6D**). Note that to avoid the artifact of DZIP3-mediated Cyclin D1 stability, we have loaded the IP samples in a ratio that can equalize the Cyclin D1 in inputs. Therefore, more IP samples were loaded in the second lane. Still, we found that the ubiquitination was less in DZIP3 knockdown cells, suggesting that indeed DZIP3 plays a significant role in K63-linked ubiquitination of Cyclin D1.

DZIP3 interacts with Cyclin D1 in a cell-cycle phase-specific manner, predominantly in the G_1 phase. So, we asked whether the DZIP3-mediated K63-linked ubiquitination of Cyclin D1 is also phase specific. For this, we overexpressed DZIP3, Cyclin D1, and HA-K63, and then synchronized the cells in the G_1 phase, S phase, and G_2 phase. Indeed, we found that DZIP3-mediated K63-linked ubiquitination of Cyclin D1 was increased primarily in the G_1 phase (**Fig. 6E**). Altogether, the results suggest that DZIP3 interactions with Cyclin D1 proteins and subsequent K63-linked ubiquitination are cell-cycle phase-specific events.

The RING domain of DZIP3 is important for the K63-linked ubiquitination and stability of Cyclin D1

The RING domain of DZIP3 was shown to be essential for auto-ubiquitination and ubiquitination of other proteins (13, 14). The RING domain-deleted DZIP3 (Flag-ΔRING DZIP3) variant was found to be inefficient in increasing the K63-linked ubiquitination of the Cyclin D1 proteins (**Fig. 6F**), suggesting that the RING domain of DZIP3 is absolutely required for enhancing K63-linked ubiquitination of Cyclin D1. Next, we asked whether the RING domain is important for the stability of Cyclin D1. RING-deleted DZIP3 was not able to increase the stability of Cyclin D1 (**Fig. 6G**), whereas, to our surprise, over-expression of the RING domain itself was sufficient to increase the stability of Cyclin D1 (**Fig. 6H**). Overall, the data suggest that DZIP3 utilizes its RING domain to increase the K63-linked ubiquitination and stability of the Cyclin D1.

Further, we tested whether the presence of DZIP3 protects from proteasomal degradation. The control and DZIP3 shRNA stable cell lines were treated with MG132, a proteasomal degradation inhibitor

(**Fig. 6I**). The MG132-treated control cells, as compared with untreated cells, showed 2-fold induction of Cyclin D1, whereas DZIP3 knockdown cells showed 8-fold induction (**Fig. 6I**), indicating a considerably higher proteasomal degradation flux of Cyclin D1 in the absence of DZIP3.

DZIP3 controls E2F target genes

The Cyclin D1–CDK4/6 complex phosphorylates the tumor suppressor retinoblastoma (RB) protein and inactivates it, leading to the release of E2F transcription factors (59). E2Fs then activate a large number of genes required for cellular proliferation, including the genes essential for the G_1–S phase transition and DNA replication (**Fig. 7A**; ref. 60). We performed qRT-PCR for several E2F target genes, including CCNE1, CCNA2, CDK1, CHK1, SKP2, RBL1, E2F5, AURKB, RAD17, and RAD52, in control and DZIP3 knockdown cell lines (**Fig. 7B** and **C**). The data show that the depletion of DZIP3 significantly reduces the expression of E2F-regulated cell proliferation-related genes, including the genes required for cell-cycle progression. The expression of some of these genes was also validated in tumors (Supplementary Fig. S6A). In addition, we performed Western blotting experiments with few of the E2F regulated cell-cycle genes, including Cyclin A2, Cyclin E1, CDK1, CDK2, and c-MYC in control and DZIP3-depleted xenograft tumors and cell lines (**Fig. 7D** and **E**; Supplementary Fig. S6B). A marked reduction in expressions of all these essential cell-cycle proteins was observed in DZIP3-depleted conditions. In contrast, the overexpression of DZIP3 induced the expression of these proteins (**Fig. 7F**). Further, the complementation of DZIP3-depleted cells with Flag-DZIP3 restored the levels of Cyclin E1 and Cyclin A2, demonstrating the specificity of the control (**Fig. 7G**). Taken together, the data show that DZIP3 controls Cyclin D1–E2F axes to regulate cell growth and cell-cycle progression.

In this study, we found that DZIP3 is a novel regulator of cell-cycle progression by controlling the expression of Cyclin D1 in a unique manner. DZIP3 using its RNA-binding domain, interacts with AU-rich elements in 3′UTR of Cyclin D1 mRNA to increase its stability (**Fig. 7H**). Additionally, using its RING domain, DZIP3 increases the K63-linked ubiquitination of Cyclin D1 protein and stabilizes it (**Fig. 7H**). Predominantly, the interaction and stabilization of Cyclin D1 take place during the G_1 phase of the cell cycle, the phase during which Cyclin D1 is required for the progression of the cell cycle (**Fig. 7H**). By maintaining the expression of Cyclin D1, DZIP3 is an important regulator for E2F-mediated transcription of genes required for proliferation and cell-cycle progression (**Fig. 7H**). In agreement, DZIP3 is necessary for cell-cycle progression, cell growth, and cell migration/invasion of cancer cells and thus promotes tumor progression and metastasis (**Fig. 7H**). Overall, this study identifies DZIP3 as a novel driver of cell cycle and cancer progression.

Discussion

DZIP3 is a developmentally important gene with a capability to suppress differentiation in mouse embryonic stem cells and hematopoietic stem cells (15, 16). The mice homozygous for an ENU-induced mutation in the DZIP3 allele exhibit embryonic lethality (http://www.informatics.jax.org/marker/MGI:1917433), suggesting that DZIP3 may be critical for embryonic development. This study, for the first time, underscores the importance and functional relevance of DZIP3 in the progression of the cell cycle and cancer.

Cyclin D1 is a critical regulator of cell-cycle progression in the G_1–S phase, and thus overexpression or amplification of Cyclin D1 is associated with unregulated cell growth and oncogenic transformations (18–22).
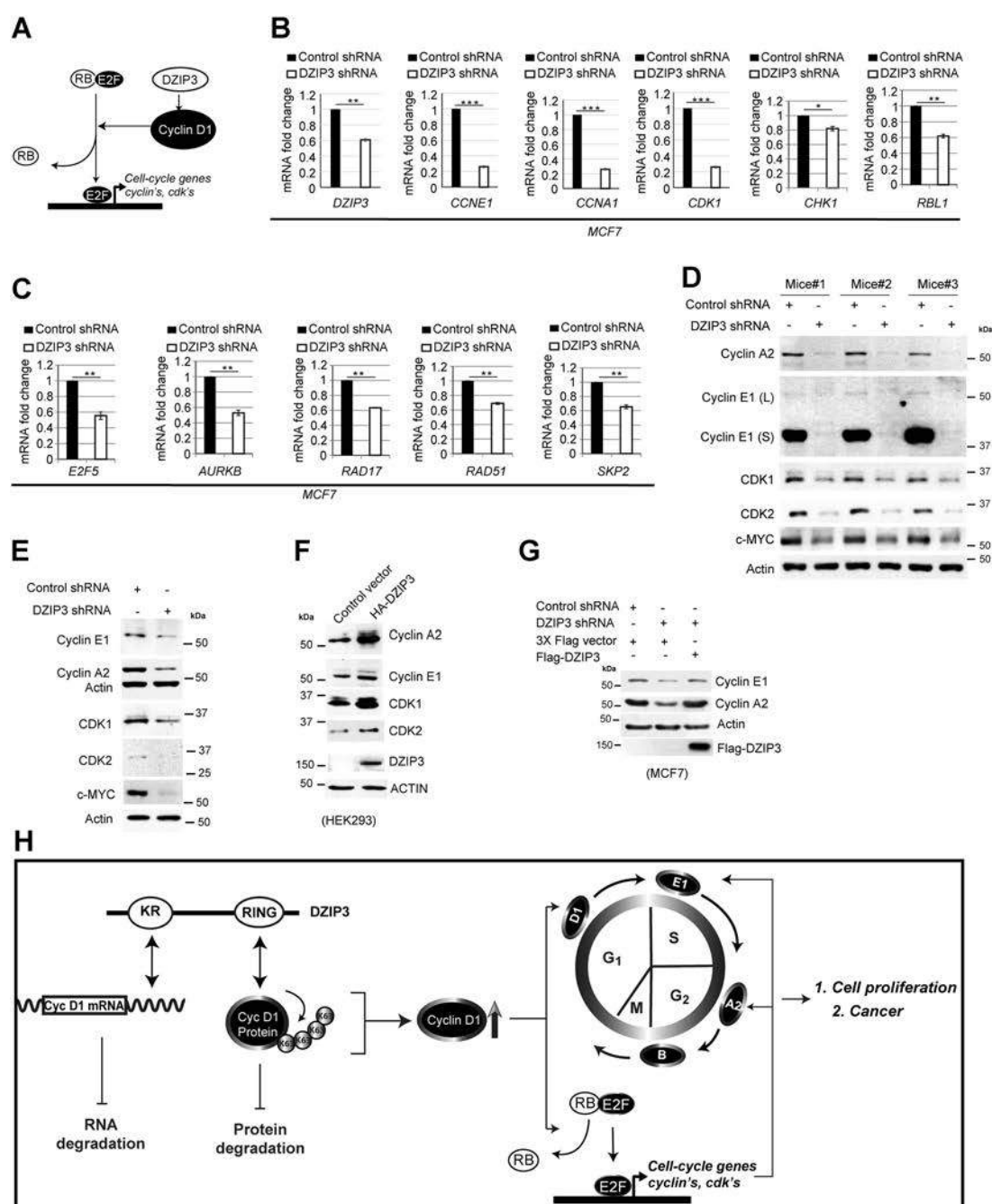
Figure 7.
DZIP3 controls Cyclin D1–E2F axes. **A,** Schematic representation of DZIP3 controlling E2F downstream genes via Cyclin D1. **B** and **C,** A qRT-PCR analysis to evaluate the expressions of indicated genes from the total RNA of MCF7 control and DZIP3 stable knockdown cells. Data, mean $\pm$ SE; n 3; , $P < 0.05$; , $P < 0.005$; , $P < 0.0005$. **D,** Western blot analysis of UM-UC3 control and DZIP3 stable knockdown tumor xenograft lysates probed with indicated antibodies. (L), large isoform; (S), small isoform. **E,** Western blot analysis of MCF7 control and DZIP3 stable knockdown cell lysates probed with indicated antibodies. **F,** Western blot analysis of HEK293 control and HA-DZIP3 transiently transfected cell lysates with indicated antibodies. **G,** Western blot analysis of MCF7 control and DZIP3 stable knockdown cells transfected with indicated plasmids and probed with indicated antibodies. **H,** Schematic presentation of work presented in this study.

A large number of studies identify Cyclin D1 as a proto-oncogene. This study provides evidence that DZIP3 controls cell cycle and cell growth by controlling the expression of Cyclin D1. DZIP3 is a member of RNA-binding RING E3-ligases (RBRL), a unique class of E3 ligases with the capability to interact with both RNA and protein. The presence of both

RNA-binding domain and E3-ligase domain in RBRL proteins provides them the capability to perform unique combinatorial spatial and temporal functions. The RBRLs, MEX3B, and DZIP3 were shown to interact with a long noncoding RNA, *HOTAIR*, to induce K48-linked ubiquitination and degradation of Ataxin-1 and Snurportin-1, respectively (14).

Another RBRL, MEX3C, interacts with 3′UTR of *HLA-A2* mRNA and causes its RING-dependent degradation (7). One more interesting kind of regulation is mediated by MDM2. MDM2 promotes polyubiquitination and proteasomal degradation of p53. On the other hand, it also binds to p53 mRNA to stabilize it, resulting in a balance of the p53 expression (61). A recent study showed that the mRNA binding activity of TRIM25 induces its ubiquitination capacity, suggesting a kind of regulation where the RNA level of one protein can regulate its own proteasomal degradation or degradation of other related proteins (62). In the present study, we revealed another unique kind of regulation by RBRL, where DZIP3 binds with mRNA and protein of the same gene to maintain their stability. The factors involved in phase-specific degradation of cyclins are very well defined; however, the factors that stabilize the cyclins during the specific cell-cycle phase remain elusive. Here, we describe one of such factor and one such mechanism. Further, we also demonstrate that DZIP3, via Cyclin D1, controls the expression of E2F transcription factor–regulated genes, including cyclins (A2 and E1) and CDKs.

Cyclins are regulated at both RNA and protein levels. The HuR protein is known to interact with 3′UTR of pan-cyclin mRNA and impart stability (24–27), whereas AUF1 binds with Cyclin D1 mRNA and increases its degradation (48, 63). DZIP3 is similar to HuR in the regulation of the stability of cyclin mRNAs. Several other proteins, including E3 ubiquitin ligases, were shown to interact with cyclin proteins and mediate their degradation or stabilization. The best examples are the APC/C complex and Skp1-Cul1-F-box (SCF) family of E3 ubiquitin ligases. They mediate the degradation of cyclins for the controlled progression of the cell cycle (23). The Cullin-3 mediates ubiquitination and degradation of Cyclin E (64). Hec1 interacts with Cyclin B1 during the early M phase and protects it from degradation by the APC/C complex; however, at the late M phase, interaction is broken, resulting in the destruction of Cyclin B1 (52). A recent study shows that ERLIN2 stabilizes Cyclin B1 in the G_2–M phase by inducing its K63-linked ubiquitination (36). In future studies, it will be interesting to determine whether DZIP3 could cooperate or antagonize activities of some of the known cell-cycle regulatory factors to orchestrate Cyclin D1 protein levels during cell-cycle progression.

Authors' Contributions

S.P. Kolapalli: Conceptualization, investigation, and methodology**. R. Sahu:** Validation, investigation, and methodology. **N.R. Chauhan:** Investigation. **K.K. Jena:** Investigation. **S. Mehto:** Investigation. **S.K. Das:** Investigation. **A. Jain:** Investigation. **M. Rout:** Investigation. **R. Dash:** Supervision. **R.K. Swain:** Supervision. **D.Y. Lee:** Supervision. **T.E. Rusten:** Supervision. **S. Chauhan:** Conceptualization, resources, data curation, software, formal analysis, supervision, funding acquisition, investigation, methodology, writing–original draft, writing–review, and editing. **S. Chauhan:** Conceptualization, resources, data curation, formal analysis, supervision, funding acquisition, validation, investigation, methodology, and writing–original draft.

The costs of publication of this article were defrayed in part by the payment of page charges. This article must therefore be hereby marked *advertisement* in accordance with 18 U.S.C. Section 1734 solely to indicate this fact.

References

1. Berndsen CE, Wolberger C. New insights into ubiquitin E3 ligase mechanism. Nat Struct Mol Biol 2014;21:301–7.
2. Lukong KE, Chang KW, Khandjian EW, Richard S. RNA-binding proteins in human genetic disease. Trends Genet 2008;24:416–25.
3. Hildebrandt A, Alanis-Lobato G, Voigt A, Zarnack K, Andrade-Navarro MA, Beli P, et al. Interaction profiling of RNA-binding ubiquitin ligases reveals a link between posttranscriptional regulation and the ubiquitin system. Sci Rep 2017; 7:16582.
4. Garzia A, Jafarnejad SM, Meyer C, Chapat C, Gogakos T, Morozov P, et al. The E3 ubiquitin ligase and RNA-binding protein ZNF598 orchestrates ribosome quality control of premature polyadenylated mRNAs. Nat Commun 2017; 8:16056.
5. Zhang Q, Fan L, Hou F, Dong A, Wang YX, Tong Y. New insights into the RNA-binding and E3 ubiquitin ligase activities of roquins. Sci Rep 2015;5:15660.
6. Kuniyoshi K, Takeuchi O, Pandey S, Satoh T, Iwasaki H, Akira S, et al. Pivotal role of RNA-binding E3 ubiquitin ligase MEX3C in RIG-I-mediated antiviral innate immunity. Proc Natl Acad Sci U S A 2014;111:5646–51.
7. Cano F, Bye H, Duncan LM, Buchet-Poyau K, Billaud M, Wills MR, et al. The RNA-binding E3 ubiquitin ligase MEX-3C links ubiquitination with MHC-I mRNA degradation. EMBO J 2012;31:3596–606.
8. Huang L, Malu S, McKenzie JA, Andrews MC, Talukder AH, Tieu T, et al. The RNA-binding protein MEX3B mediates resistance to cancer immunotherapy by downregulating HLA-A expression. Clin Cancer Res 2018;24:3366–76.
9. Fu XF, Cheng SF, Wang LQ, Yin S, De Felici M, Shen W. DAZ family proteins, key players for germ cell development. Int J Biol Sci 2015;11:1226–35.
10. Zhang B, Wang G, Xu X, Yang S, Zhuang T, Wang G, et al. DAZ-interacting protein 1 (Dzip1) phosphorylation by polo-like kinase 1 (Plk1) regulates the centriolar satellite localization of the BBSome protein during the cell cycle. J Biol Chem 2017;292:1351–60.
11. Shigunov P, Sotelo-Silveira J, Stimamiglio MA, Kuligovski C, Irigoin F, Badano JL, et al. Ribonomic analysis of human DZIP1 reveals its involvement in ribonucleoprotein complexes and stress granules. BMC Mol Biol 2014;15:12.
12. Wang C, Li J, Takemaru KI, Jiang X, Xu G, Wang B. Centrosomal protein Dzip1l binds Cby, promotes ciliary bud formation, and acts redundantly with Bromi to regulate ciliogenesis in the mouse. Development 2018;145:dev164236.
13. Kreft SG, Nassal M. hRUL138, a novel human RNA-binding RING-H2 ubiquitin-protein ligase. J Cell Sci 2003;116:605–16.
14. Yoon JH, Abdelmohsen K, Kim J, Yang X, Martindale JL, Tominaga-Yamanaka K, et al. Scaffold function of long non-coding RNA HOTAIR in protein ubiquitination. Nat Commun 2013;4:2939.
15. De La Fuente R, Baumann C, Viveiros MM. ATRX contributes to epigenetic asymmetry and silencing of major satellite transcripts in the maternal genome of the mouse embryo. Development 2015;142:1806–17.
16. Inoue D, Aihara H, Sato T, Mizusaki H, Doiguchi M, Higashi M, et al. Dzip3 regulates developmental genes in mouse embryonic stem cells by reorganizing 3D chromatin conformation. Sci Rep 2015;5:16567.
17. Purcell DJ, Chauhan S, Jimenez-Stinson D, Elliott KR, Tsewang TD, Lee YH, et al. Novel CARM1-interacting protein, DZIP3, is a transcriptional coactivator of estrogen receptor-alpha. Mol Endocrinol 2015;29:1708–19.
18. Kim JK, Diehl JA. Nuclear cyclin D1: an oncogenic driver in human cancer. J Cell Physiol 2009;220:292–6.
19. Sauter ER, Yeo UC, von Stemm A, Zhu W, Litwin S, Tichansky DS, et al. Cyclin D1 is a candidate oncogene in cutaneous melanoma. Cancer Res 2002;62:3200–6.

20. Bates S, Peters G. Cyclin D1 as a cellular proto-oncogene. Semin Cancer Biol 1995;6:73–82.

21. Callender T, el-Naggar AK, Lee MS, Frankenthaler R, Luna MA, Batsakis JG. PRAD-1 (CCND1)/cyclin D1 oncogene amplification in primary head and neck squamous cell carcinoma. Cancer 1994;74:152–8.

22. Tashiro E, Tsuchiya A, Imoto M. Functions of cyclin D1 as an oncogene and regulation of cyclin D1 expression. Cancer Sci 2007;98:629–35.

23. Vodermaier HC. APC/C and SCF: controlling each other and the cell cycle. Curr Biol 2004;14:R787–96.

24. Guo X, Connick MC, Vanderhoof J, Ishak MA, Hartley RS. MicroRNA-16 modulates HuR regulation of cyclin E1 in breast cancer cells. Int J Mol Sci 2015; 16:7112–32.

25. Guo X, Hartley RS. HuR contributes to cyclin E1 deregulation in MCF-7 breast cancer cells. Cancer Res 2006;66:7948–56.

26. Wang W, Caldwell MC, Lin S, Furneaux H, Gorospe M. HuR regulates cyclin A and cyclin B1 mRNA stability during cell proliferation. EMBO J 2000;19: 2340–50.

27. Kakuguchi W, Kitamura T, Kuroshima T, Ishikawa M, Kitagawa Y, Totsuka Y, et al. HuR knockdown changes the oncogenic potential of oral cancer cells. Mol Cancer Res 2010;8:520–8.

28. Nakamura H, Kawagishi H, Watanabe A, Sugimoto K, Maruyama M, Sugimoto M. Cooperative role of the RNA-binding proteins Hzf and HuR in p53 activation. Mol Cell Biol 2011;31:1997–2009.

29. Mazan-Mamczarz K, Galban S, Lopez de Silanes I, Martindale JL, Atasoy U, Keene JD, et al. RNA-binding protein HuR enhances p53 translation in response to ultraviolet light irradiation. Proc Natl Acad Sci U S A 2003;100:8354–9.

30. Cho SJ, Zhang J, Chen X. RNPC1 modulates the RNA-binding activity of, and cooperates with, HuR to regulate p21 mRNA stability. Nucleic Acids Res 2010; 38:2256–67.

31. Wang W, Furneaux H, Cheng H, Caldwell MC, Hutter D, Liu Y, et al. HuR regulates p21 mRNA stabilization by UV light. Mol Cell Biol 2000;20:760–9.

32. Dong L, Yu L, Bai C, Liu L, Long H, Shi L, et al. USP27-mediated Cyclin E stabilization drives cell cycle progression and hepatocellular tumorigenesis. Oncogene 2018;37:2702–13.

33. Lin Z, Tan C, Qiu Q, Kong S, Yang H, Zhao F, et al. Ubiquitin-specific protease 22 is a deubiquitinase of CCNB1. Cell Discov 2015;1:15028.

34. Bonacci T, Suzuki A, Grant GD, Stanley N, Cook JG, Brown NG, et al. Cezanne/ OTUD7B is a cell cycle-regulated deubiquitinase that antagonizes the degradation of APC/C substrates. EMBO J 2018;37:e98701.

35. Li L, Li W, Xiao L, Xu J, Chen X, Tang M, et al. Viral oncoprotein LMP1 disrupts p53-induced cell cycle arrest and apoptosis through modulating K63-linked ubiquitination of p53. Cell Cycle 2012;11:2327–36.

36. Zhang X, Cai J, Zheng Z, Polin L, Lin Z, Dandekar A, et al. A novel ER-microtubule-binding protein, ERLIN2, stabilizes cyclin B1 and regulates cell cycle progression. Cell Discov 2015;1:15024.

37. Tripathi E, Smith S. Cell cycle-regulated ubiquitination of tankyrase 1 by RNF8 and ABRO1/BRCC36 controls the timing of sister telomere resolution. EMBO J 2017;36:503–19.

38. Jena KK, Kolapalli SP, Mehto S, Nath P, Das B, Sahoo PK, et al. TRIM16 controls assembly and degradation of protein aggregates by modulating the p62-NRF2 axis and autophagy. EMBO J 2018;37:e98358.

39. Jena KK, Mehto S, Nath P, Chauhan NR, Sahu R, Dhar K, et al. Autoimmunity gene IRGM suppresses cGAS-STING and RIG-I-MAVS signaling to control interferon response. EMBO Rep 2020:e50051.

40. Mehto S, Jena KK, Nath P, Chauhan S, Kolapalli SP, Das SK, et al. The Crohn's disease risk factor IRGM limits NLRP3 inflammasome activation by impeding its assembly and by mediating its selective autophagy. Mol Cell 2019;73:429–45 e7.

41. Ren J, Liu S, Cui C, Ten Dijke P. Invasive behavior of human breast cancer cells in embryonic zebrafish. J Vis Exp 2017;122:55459.

42. Tang Z, Kang B, Li C, Chen T, Zhang Z. GEPIA2: an enhanced web server for large-scale expression profiling and interactive analysis. Nucleic Acids Res 2019; 47:W556–W60.

43. Cuylen S, Blaukopf C, Politi AZ, Muller-Reichert T, Neumann B, Poser I, et al. Ki-67 acts as a biological surfactant to disperse mitotic chromosomes. Nature 2016;535:308–12.

44. Letrado P, de Miguel I, Lamberto I, Diez-Martinez R, Oyarzabal J. Zebrafish: speeding up the cancer drug discovery process. Cancer Res 2018;78:6048–58.

45. Motokura T, Arnold A. Cyclin D and oncogenesis. Curr Opin Genet Dev 1993;3: 5–10.

46. Musgrove EA, Caldon CE, Barraclough J, Stone A, Sutherland RL. Cyclin D as a therapeutic target in cancer. Nat Rev Cancer 2011;11:558–72.

47. Tang Z, Li C, Kang B, Gao G, Li C, Zhang Z. GEPIA: a web server for cancer and normal gene expression profiling and interactive analyses. Nucleic Acids Res 2017;45:W98–W102.

48. Al-Khalaf HH, Colak D, Al-Saif M, Al-Bakheet A, Hendrayani SF, Al-Yousef N, et al. p16(INK4a) positively regulates cyclin D1 and E2F1 through negative control of AUF1. PLoS One 2011;6:e21111.

49. Bakheet T, Hitti E, Khabar KSA. ARED-Plus: an updated and expanded database of AU-rich element-containing mRNAs and pre-mRNAs. Nucleic Acids Res 2018;46:D218–D20.

50. Castro A, Bernis C, Vigneron S, Labbe JC, Lorca T. The anaphase-promoting complex: a key factor in the regulation of cell cycle. Oncogene 2005;24:314–25.

51. Higa LA, Yang X, Zheng J, Banks D, Wu M, Ghosh P, et al. Involvement of CUL4 ubiquitin E3 ligases in regulating CDK inhibitors Dacapo/p27Kip1 and cyclin E degradation. Cell Cycle 2006;5:71–7.

52. Gui L, Homer H. Hec1-dependent cyclin B2 stabilization regulates the G2-M transition and early prometaphase in mouse oocytes. Dev Cell 2013;25: 43–54.

53. Alam MS. Proximity ligation assay (PLA). Curr Protoc Immunol 2018; 123:e58.

54. Baldin V, Lukas J, Marcote MJ, Pagano M, Draetta G. Cyclin D1 is a nuclear protein required for cell cycle progression in G_1. Genes Dev 1993;7:812–21.

55. Choi KS, Choi HJ, Lee JK, Im S, Zhang H, Jeong Y, et al. The endothelial E3 ligase HECW2 promotes endothelial cell junctions by increasing AMOTL1 protein stability via K63-linked ubiquitination. Cell Signal 2016;28:1642–51.

56. Lauwers E, Jacob C, Andre B. K63-linked ubiquitin chains as a specific signal for protein sorting into the multivesicular body pathway. J Cell Biol 2009;185: 493–502.

57. Erpapazoglou Z, Walker O, Haguenauer-Tsapis R. Versatile roles of k63-linked ubiquitin chains in trafficking. Cells 2014;3:1027–88.

58. Zhang J, Zhang C, Cui J, Ou J, Han J, Qin Y, et al. TRIM45 functions as a tumor suppressor in the brain via its E3 ligase activity by stabilizing p53 through K63-linked ubiquitination. Cell Death Dis 2017;8:e2831.

59. Weinberg RA. The retinoblastoma protein and cell cycle control. Cell 1995;81: 323–30.

60. Bracken AP, Ciro M, Cocito A, Helin K. E2F target genes: unraveling the biology. Trends Biochem Sci 2004;29:409–17.

61. Cano F, Miranda-Saavedra D, Lehner PJ. RNA-binding E3 ubiquitin ligases: novel players in nucleic acid regulation. Biochem Soc Trans 2010;38:1621–6.

62. Choudhury NR, Heikel G, Trubitsyna M, Kubik P, Nowak JS, Webb S, et al. RNA-binding activity of TRIM25 is mediated by its PRY/SPRY domain and is required for ubiquitination. BMC Biol 2017;15:105.

63. Lin S, Wang W, Wilson GM, Yang X, Brewer G, Holbrook NJ, et al. Down-regulation of cyclin D1 expression by prostaglandin A(2) is mediated by enhanced cyclin D1 mRNA turnover. Mol Cell Biol 2000;20:7903–13.

64. Singer JD, Gurian-West M, Clurman B, Roberts JM. Cullin-3 targets cyclin E for ubiquitination and controls S phase in mammalian cells. Genes Dev 1999;13: 2375–87.